# Micromagnetic Modeling of Magnetic Storage Devices

**A DISSERTATION**
**SUBMITTED TO THE FACULTY OF THE GRADUATE SCHOOL**
**OF THE UNIVERSITY OF MINNESOTA**
**BY**

**Wei-Heng Hsu**

**IN PARTIAL FULFILLMENT OF THE REQUIREMENTS**
**FOR THE DEGREE OF**
**DOCTOR OF PHILOSOPHY**

**Advisor: Randall H. Victora**

**March, 2021**

# Acknowledgements

First and foremost, I would like to express my sincere gratitude to my advisor, Professor Randall Victora, for his patience and support throughout my doctoral studies. His guidance not only showed me how to be a good researcher, but also inspired my life. The most important thing I learned from him is how to think. I am truly grateful to have Professor Victora as my advisor.

I would like to thank my committee members, Professor Bethanie Stadler, Professor Steven Koester, and Professor Paul Crowell, for providing valuable guidance and feedback on my research. I also appreciate learning from Professor Jian-Ping Wang and other MINT professors. I would also like to thank my manager Dr. Stephanie Hernández and the team members for their help during my internship at Seagate Technology.

I am grateful to Dr. Pin-Wei Huang. Without his advice, I would not have came to University of Minnesota and joined Prof. Victora's group. I would like to thank all the group members for their support and help, Aneesh Venugopal, Dr. Tao Qu, Kun Xue, Yijia Liu, Dr. Niranjan Natekar, Dr. Zengyuan Liu, Dr. Rizvi Ahmed, Dr. Ali Ghoreyshi, Dr. Yipeng Jiao, Dr. Ziran Wang, Dr. Warunee Tipcharoen, and Roy Bell. I also like to thank Joseph Um, Karthik Srinivasan, Reza Zamani, Dr. Kai Wu, Dr. Diqing Su, Renata Saha and other colleagues in MINT center and ECE department. Special thanks to Dr. Zengyuan Liu not only for mentoring me when I first joined the group, but also for the guidance during my internship. Many thanks to Aneesh Venugopal for all the conversations regarding research and life since we were in Michigan. Moreover, I truly appreciate all my friends who have helped me and been there with me during my difficult times.

Finally, and the most importantly, I would like to thank my dear parents and my sister. Nothing would have been possible without their love and support.

# Dedication

To my beloved family.

## Abstract

Hard disk drives (HDDs) are the dominant mass storage devices for personal and cloud storage due to their low cost and high capacity. Heat-assisted magnetic recording (HAMR) is considered to be next-generation recording technology for HDDs. While HAMR shows the potential for areal density to go beyond one terabit per square inch, this new recording mechanism requires further understanding and optimization before commercialization. First, I examine the relationship between media noise power and linear density in HAMR. I observe that there is a noise plateau at intermediate recording density and show that the plateau can be shifted to different recording density regions depending on the temperature profile. This effect is argued to be a consequence of the competition between transition noise and remanence noise in HAMR. To extend the recording density limit, heat-assisted shingled magnetic recording is studied. The transitions are no longer symmetric about the track center after shingled writing, especially when the transitions are highly curved as a result of the temperature profile generated by the near-field transducer. I propose a new reading scheme by rotating the read head to match the curved transitions. For a single rotated head, more than 10% improvement in user density over that of a single non-rotated head is achieved. I found that the optimal rotation angle generally follows the transition shape. With an array of two rotated heads, a track pitch of 15 nm, and a minimum bit length of 6.0 nm, the user areal density reaches 6.2 terabits per square inch, more than 30% above previous projections for recording on granular media.

Magnetoresistive random-access memory (MRAM) is another type of magnetic storage device that is mainly used as computer memory. As semiconductor-based memory begins to hit physical limits, spin-transfer torque (STT) MRAM and spin-orbit torque (SOT) MRAM appear to be strong candidates for future memory applications. I start first by studying SOT switching in magnetic insulators. Magnetic insulators (MIs), in particular rare-earth iron garnets, have low damping compared to metallic ferromagnetic materials due to lack of conduction electrons. Analogous to STT devices, their low-damping nature is presumed to be an advantage for SOT applications. I report that perpendicular magnetic anisotropy (PMA) material with low damping does not

favor reliable SOT switching, but increased damping, interfacial Dzyaloshinskii–Moriya interactions, or field-like torques may help SOT switching in some cases. Notches in a nanometer-scale element, which is a more realistic size for practical applications, can also improve switching stability. To fully utilize low damping MIs with SOT, an in-plane exchange-coupled composite free layer SOT-MRAM is proposed. The free layer consists a low-damping soft MI and a high anisotropy material. The adoption of high anisotropy materials, such as $L1_0$ alloy, not only facilitates the achievement of ultra-high-density memory but also allows for the reduction of heavy metal layer volume and thus a reduction in write energy not seen in previous CoFeB-based SOT-MRAM. A write energy of 18 attojoules per bit for 1 ns switching is achieved which is only 72 times more than the theoretical limit of $60k_BT$. It also represents a factor of more than five hundred times improvement relative to state-of-the-art dynamic RAM.

# Contents

# List of Tables

# List of Figures

# Chapter 1

# Introduction

Magnetism in solids originates from the spin of electrons. The unique nature of magnetic materials gives rise to many applications in our lives. Ancient magnetic compasses, modern-day motors, transformers, actuators, hard disk drives (HDDs), and even the magnetic strip on credit cards and transportation tickets all rely on magnetic materials. One important feature of magnetic materials is magnetic hysteresis — their magnetization is retained even without a magnetic field. This property allows magnetic materials to store data.

The history of magnetic storage can be traced back to the late-19th century. Oberlin Smith was the first person to propose that sound or information could be stored in magnetic materials; he published the idea in 1888 [16]. In 1898, Valdemar Poulsen independently developed the "telegraphone", the first true magnetic wire recorder. After the invention of magnetic tape drives for audio and video recording in the mid-20th century, the first commercial HDD, the IBM 350, was introduced along with the IBM 305 Random Access Method of Accounting and Control (RAMAC) system by the International Business Machines Corporation (IBM) in 1956. The HDD soon replaced magnetic tape drives as the dominant secondary storage in computer systems. As in Moore's law for semiconductor devices, the areal density in HDDs also shows exponential growth [17]. The areal density of HDDs in 2015 was around 1 terabit/in$^2$; this was eight orders of magnitude more than the IBM 350 drive which weighed over a ton and achieved only 2,000 bits/in$^2$.

Over the past six decades, the HDD has evolved into an essential component for

digital data storage. Magnetic data storage technology and semiconductor technology have shaped the modern information age. Although the HDD market share is decreasing due to advancements in solid-state drives (SSDs), HDDs remain solid candidates for data centers because they are less costly than SSDs, especially since the projected size of all global data storage may exceed 175 zettabytes by 2025 [18]. To extend areal density growth for HDDs, it is crucial to develop the next generation of magnetic recording technology. Heat-assisted magnetic recording (HAMR) has been introduced as the successor to contemporary perpendicular magnetic recording (PMR) [19], but the new physics, new materials, and new recording system for HAMR lead to new challenges.

Aside from data storage, magnetic materials can also serve as the primary storage in computers. Magnetic core memory was the dominant memory for 20 years since mid-1950s until the invention of metal-oxide-semiconductor (MOS) memory in the 1970s. In the 1980s, Honeywell introduced a new type of magnetic memory based on the magnetoresistance (MR) effect called magnetoresistive random-access memory (MRAM). An ideal MRAM has the speed of static RAM and the density of dynamic RAM. Also, its non-volatile nature and high endurance make MRAM very attractive as computer memory. The discovery of giant magnetoresistance (GMR) in magnetic multilayers in 1988 by Albert Fert [20] and Peter Grünberg [21] led to further signal strength enhancement of MRAM. It also enhanced the sensitivity of the MR sensor (which shares the same physics as the MRAM), leading to a huge increase in HDD areal density. The development of GMR started an era of spin electronics, or "spintronics", which added new functionalities to conventional electronics by utilizing the spin degree of freedom of electrons. Even with GMR, however, signal strength of MRAM is still low compared to that of MOS memory. Also, the large write current and magnetic field-driven switching in early MRAM limited its density.

In 1996, Luc Berger [22] and John Slonczewski [23] proposed that spin-polarized current can be used to manipulate magnetization through angular momentum transfer. This effect is called spin-transfer torque (STT) which is the most important phenomenon in modern magnetism and spintronics. STT, along with the development of tunnel magnetoresistance (TMR) in a magnetic tunnel junction (MTJ), has reintroduced MRAM

to the memory competition. However, even with decades of development, the performance of MRAM is still poorer than current memory technology. New materials or new physics such as spin-orbit torque (SOT) are needed for next-generation low-power high-density MRAM.

The rest of this introductory chapter presents a brief overview of HDDs and MRAM.

## 1.1 Hard Disk Drives

HDDs are electromechanical devices. The data are stored in the magnetic materials coated on the rotating platter. An inductive write head generates a magnetic field to write data while a MR read head senses the magnetic field of the recorded bits. The write head and read head are both fabricated on the tip of a slider controlled by an actuator (Fig. 1.1).

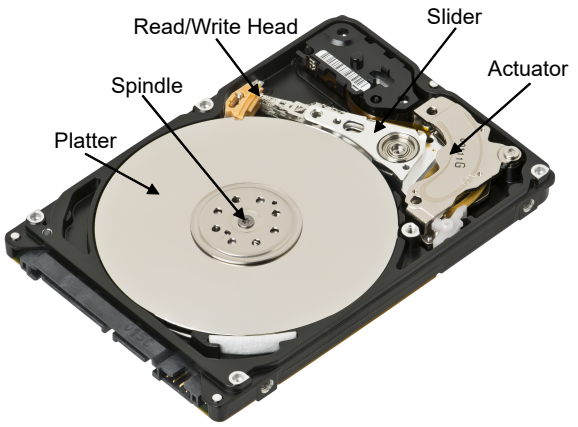


Figure 1.1: Internals of a modern hard disk drive. Adapted from Ref. [1] under license CC BY-SA 3.0.

In this section, the recording media is the main focus; the working principle of the MR sensor will be discussed in Sec. 1.2.1. Readers who are interested in recording physics and systems can learn more details in Ref. [24–26].

### 1.1.1 Superparamagnetic Limit and Magnetic Recording Trilemma

The recording medium used in HDDs is a granular structure. Because the magnetic properties and geometry of each grain differ, each bit is stored in several grains to reduce noise from grain variation. For high-density magnetic recording, the size of each bit must be reduced along with the magnetic grain. The anisotropy energy of a grain is the product of the grain's anisotropy constant ($K$) and volume ($V$); this defines the energy needed to reverse the magnetization of the grain. When grain size decreases to a volume where the anisotropy energy becomes too small, the magnetization will flip randomly due to thermal fluctuations. This effect is called superparamagnetism. To keep information stored for 10 years, $KV$ should be equal to at least $60k_BT$ at room temperature where $k_B$ is the Boltzman constant and $T$ is the temperature. This superparamagnetic limit has long been the driving force for the development of new technology for high-density magnetic recording.

One way to maintain enough thermal stability at reduced volume is to introduce materials with a higher $K$. A higher $K$ indicates a stronger anisotropy field (or coercivity). A stronger anisotropy field requires a stronger magnetic field to record the data. However, the magnetic field that a write head can generate is limited. It is evident that it is hard to satisfy the readability, stability, and writeability requirements all at the same time. This situation is referred to as the "magnetic recording trilemma".

### 1.1.2 From Longitudinal Magnetic Recording to Perpendicular Magnetic Recording

The first time the HDD industry encountered the superparamagnetic limit was during the transition between longitudinal magnetic recording (LMR) and PMR. Before 2005, recording in HDDs was based on LMR. In LMR, the magnetization of the recorded bits lies in the disk plane (Fig. 1.2(a)). In the transition regions of LMR, the magnetic charges between each bit create a strong demagnetizing field which destabilizes the bits, especially at high recording densities when bits are closer together. Also smaller bits require a thicker medium to maintain enough $KV$, but the unfavorable demagnetizing field increases with thickness. In PMR, the easy axis of magnetization is in an out-of-disk-plane direction (Fig. 1.2(b)). Magnetic charges with different polarities occur

at the transitions in PMR which reduces the unwanted demagnetizing field. Also, the introduction of a soft underlayer in PMR that serves as a magnetic mirror doubles the write field strength. This strong write field allows the usage of high $K$ material. With exchange coupled composite (ECC) media [27,28] and other new technologies from media level to system level, PMR successfully continues areal density growth.

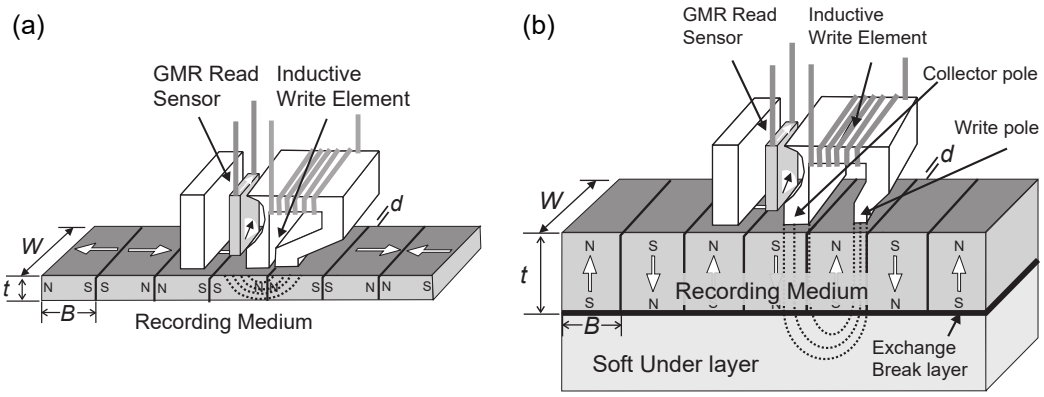


Figure 1.2: Schematic drawings of (a) longitudinal magnetic recording and (b) perpendicular magnetic recording. 

### 1.1.3 Heat-Assisted Magnetic Recording (HAMR)

However, the scaling of PMR leads to another superparamagnetic limit. Two new technologies, HAMR [3,19] and microwave-assisted magnetic recording [29], have been proposed to address the issue. Both technologies use external energy (heat for former and microwave for latter) to assist writing. HAMR is expected to be the leading technology for next-generation magnetic recording, especially with the commercial introduction of HAMR drives by Seagate Technology at the end of 2020.

The idea of HAMR is to use the dependence of coercivity on temperature; the coercivity drops when the temperature increases (Fig. 1.3(b)). This characteristic allows recording media with much higher $K$ to encounter the supermagnetic limit. A near field transducer is used to locally heat a high $K$ medium to a temperature close to its Curie temperature ($T_c$) (Fig. 1.3(a)), and the data is written at the same time with a lowered coercivity. Once the medium cools down to ambient temperature, the data can be

recorded stably in a smaller grain compared to that of PMR. However, this simple idea has several technical challenges that have to be overcome. One of the challenges is the new media design. The magnetic material should have high $K$ as well as good thermal properties. $L1_0$ FePt is the most promising material for the recording layer. An additional heat sink layer is needed for fast heat dissipation. The new recording physics in HAMR also introduces new noise mechanisms such as transition curvature due to the shape of the heat spot [30] and random absorption in the granular structure [31, 32]. HAMR with thermal ECC media shows the potential to achieve a user density of 4.7 $Tb/in^2$ [33].

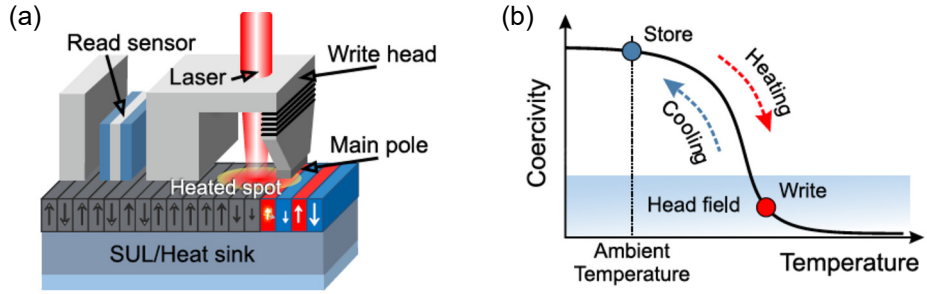


Figure 1.3: (a) Schematic drawing of HAMR. (b) Working principle of HAMR. Adapted from Ref. [3], with the permission of AIP Publishing.

## 1.2 Magnetoresistive Random-Access Memory (MRAM)

Modern MRAM consists of a trilayer structure where an insulator or a non-magnetic (NM) layer is sandwiched between two ferromagnetic (FM) layers. Magnetization in one of the FM layers is pinned and called the fixed, pinned, or reference layer, while magnetization in the other FM layer is free to change and is called the free layer (Fig. 1.4). The resistance state of the MRAM depends on the relative magnetization orientation between the free layer and the fixed layer. The resistance is high if magnetizations in the layers are aligned antiparallelly (AP state) and low if aligned parallelly (P state).

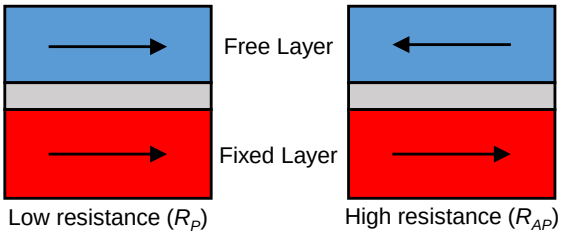


Figure 1.4: Schematic drawing of MRAM working principle.

### 1.2.1 Magnetoresistance

MR is the property of electrical resistance in a material (usually magnetic) that changes with an applied magnetic field and its magnetization orientation. The MR ratio is used to measure how effective the MR is; usually, MR ratio and MR are used interchangeably. The MR effect can be used as a magnetic sensor as in the read head of an HDD. It can also be used as the read mechanism in MRAM where the high and low resistance states represent logic "0" and "1".

#### Ordinary Magnetoresistance

Ordinary MR occurs in NM material. The applied field causes electrons to move in cyclotron orbits until they scatter. It reduces the mean free path and thus changes the resistivity. This effect is small unless the applied field is large.

#### Two-Channel Model

In a FM material, the $d$-electron energy band splits due to the exchange interaction between majority spins (or up-spins $\uparrow$) and minority spins (or down-spins $\downarrow$). At the Fermi level, electrons with different spins are at different states and thus have different transport properties. This spin-dependent transport [34] can be understood as a two-channel (or two-current) model where $\uparrow$-electrons and $\downarrow$-electrons experience different resistivity. This simple idea can be extended to most spin-dependent transport with modifications such as spin-mixing.

### Anisotropic Magnetoresistance (AMR)

William Thomson, better known as Lord Kelvin, discovered that the resistivity ($\rho$) in FM matals varies with angle between current flow direction and applied field or magnetization direction. The $\rho$ is higher if the current direction is parallel to the magnetization ($\rho_{\parallel}$) than it is perpendicular to the magnetization ($\rho_{\perp}$). This effect is referred to as anisotropic magnetoresistance (AMR). The origin of AMR is spin-orbit interaction (SOI). SOI results in $s$-$d$ scattering and mixes $\uparrow$-electrons and $\downarrow$-electrons. A rotation in magnetization changes the scattering rate and thus affect the $\rho$. The total $\rho$ is expressed as $\rho = \rho_{\perp} + (\rho_{\parallel} - \rho_{\perp}) \cos^2 \theta$ with $\theta$ as the angle between current direction and the magnetization. The maximum AMR ratio is defined as $(\rho_{\parallel} - \rho_{\perp})/\rho$ with a typical value of $\approx 2\%$. Read heads based on AMR replaced thin-film inductive heads due to better signal. In contrast, this 2% AMR is too low for MRAM to compete with semiconductor memory since a low MR ratio leads to weak signal levels and long access times.

### Giant Magnetoresistance (GMR)

The discovery of GMR is said to be the beginning of modern magnetism and spintronics. The GMR ratio is on the order of 10% and is more than 50% at low temperature which is "giant" compared to AMR. The GMR effect consists of two important physics: spin-dependent scattering and coupling between magnetic layers. Unlike AMR which is in a single material, GMR occurs in a magnetic multilayer consisting of alternating FM and NM conductive layers. This multilayer structure later became a trilayer structure (Fig. 1.5), called a spin valve, with an NM layer sandwiched between two FM layers. The two FM layers are coupled antiferromagnetically through Ruderman–Kittel–Kasuya–Yosida (RKKY) interaction without an applied field. In the two-channel model, the electrons with spin parallel to the magnetization have lower scattering (or $\rho$) than electrons with spin antiparallel to the magnetization. Both types of electrons experience strong scattering if two FM layers are antiferromagnetically coupled (AP state), thus total resistance for the whole structure is high and is referred to as $R_{AP}$ (Fig. 1.5(a)). In an applied field, the FM layers become ferromagnetically coupled (P state), and only one type of electron has strong scattering so total resistance for the whole structure is

low and is referred to as $R_P$ (Fig. 1.5(b)). GMR is usually defined as $(R_{AP} - R_P)/R_P$. GMR improves the read head sensitivity in an HDD, but its MR ratio is still too low for a useful MRAM.

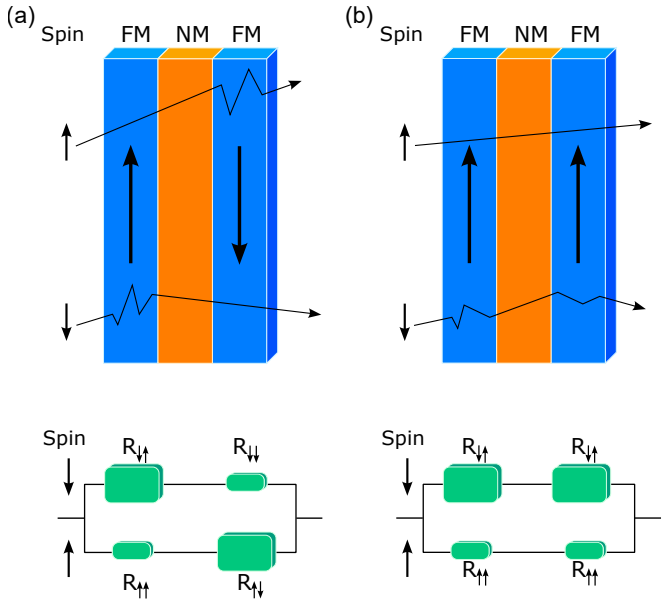


Figure 1.5: GMR effect in a trilayer structure. Arrows in the FM layers indicate the direction of magnetization. (a) Two FM layers are coupled antiferromagnetically. (b) Two FM layers are coupled ferromagnetically. Electrons with different spins experiences different resistance. Adapted from Ref. [4] under license CC BY-SA 3.0.

### Tunnel Magnetoresistance (TMR)

Tunnel magnetoresistance (TMR) occurs in a trilayer structure with an insulator as a tunnel barrier sandwiched between two FM layers. This structure is called a MTJ . Similar to GMR, high resistance occurs when the two FM layers couple antiferromagnetically, and vice versa. The TMR ratio is defined as $(R_{AP} - R_P)/R_P$. What is different from GMR is that the underlying mechanism is spin-dependent tunneling. TMR was discovered by Michel Julliére in 1975 [35], but it was not significant at only 14% at 4.2 K. A higher TMR of tens percent at room temperature was achieved with amorphous $Al_2O_3$ as a tunnel barrier [36, 37] but was still similar to GMR. In 2001, Butler [38] and Mathon [39] predicted that the TMR in a Fe/MgO/Fe structure can theoretically

exceed a thousand percent. The decay rates for energy states with different symmetry are very different in MgO. Also, the resonance states at the Fe/MgO interface only allow electrons in a particular state to tunnel. These two effects lead to a large TMR [38]. However, early attempts at MgO based TMR were only slightly better than $Al_2O_3$ based TMR [40]. The key to achieving a high TMR is a single-crystal or poly-crystal MgO film structure that avoids scattering from disorder. Yuasa [41] and Parkin [42] both reported a TMR of more than 200%; the former adopted molecular beam epitaxy (in Fe/MgO) while the latter used sputtering (in FeCo/MgO) to fabricate a high quality structure. It was later found that poly-crystalline MgO can be sputtered onto sputtered amorphous CoFeB. After annealing, CoFeB becomes a crystalline structure and is a good interface match to MgO [43]. A TMR of more than 600% at room temperature was achieved in Ref. [44]. An industry-friendly process, a high TMR, and the realization of perpendicular magnetic anisotropy (PMA) [12] make CoFeB/MgO/CoFeB an industry-standard MTJ structure widely used in HDD read heads and MRAMs. A full stack of modern CoFeB/MgO/CoFeB MTJ is shown in Fig. 1.6.

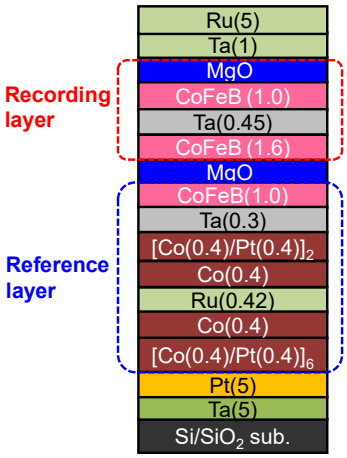


Figure 1.6: Full stack of modern MTJ. Adapted from Ref. [5]. © 2014 IEEE.

### 1.2.2 Field-Driven MRAM

Before the development of STT, an MRAM cell was written by the Oersted field generated by the current. There were two main issues in the early MRAM. Because the

magnetic field is along the entire current line, avoiding the effect on cells sharing the same current line in a memory array was the first challenge. This issue was called the half-selection issue and can be overcome with a toggle MRAM design [45]. Second, the typical current needed to generate the field necessary for switching was on the order of milliamperes. The narrow wire could not support such a large current and thus prevented MRAM scaling.

### 1.2.3 Spin-Transfer Torque MRAM (STT-MRAM)

In STT, a spin-polarized current or a spin current can exert a torque on a magnetic moment through angular momentum transfer (Fig. 1.7). STT can be used to switch magnetization or excite a spin waves. Early STT-MRAM was based on in-plane MTJ (i-MTJ) where the easy axis was in the film plane. Even though the write current was on the order of microamperes, much smaller than that of field-driven MRAM, it was still too large. Also, i-MTJ usually incorporated shape anisotropy which required a large lateral space, thus limiting the density. As in the transition from LMR to PMR in HDDs, the transition from i-MTJ to perpendicular MTJ (p-MTJ) is inevitable. The easy axis for p-MTJ is perpendicular to the film plane. The critical current density ($J_c$) to switch the free layer in an i-MTJ and a p-MTJ are given as [23, 46]

$$\text{i-MTJ:} \qquad J_{c,i} = \frac{\alpha}{\eta}\frac{2e}{\hbar}M_s t_F(H_K + 2\pi M_s), \tag{1.1}$$

$$\text{p-MTJ:} \qquad J_{c,p} = \frac{\alpha}{\eta}\frac{2e}{\hbar}M_s t_F(H_K), \tag{1.2}$$

where $\alpha$ is the Gilbert damping, $\eta$ is the STT efficiency, $e$ is the elementary charge, $\hbar$ is the reduced Planck constant, $M_s$ is the saturation magnetization, $t_F$ is the free layer thickness, and $H_k$ is the anisotropy field. Assuming all parameters are the same in both cases, $J_{c,i}$ is larger than $J_{c,p}$. In p-MTJ, STT and thermal fluctuations follow the same switching trajectory. However the demagnetizing field forces the switching trajectory for thermal fluctuations to stay in-plane in i-MTJ, so STT needs to overcome this additional demagnetization energy and thus there is a higher $J_c$ (Fig. 1.8). Besides, p-MTJ shows better scaling ability for high-density MRAM.

Nevertheless, the energy consumption of STT-MRAM so far is still higher than that of semiconductor memory, and it inescapably suffers from tunnel barrier degradation

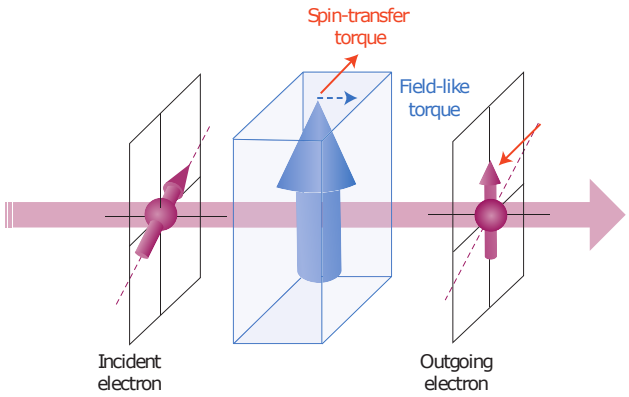


Figure 1.7: Illustration of spin-transfer torque. Reprinted from Ref. [6]. © 2012, Nature Publishing Group.

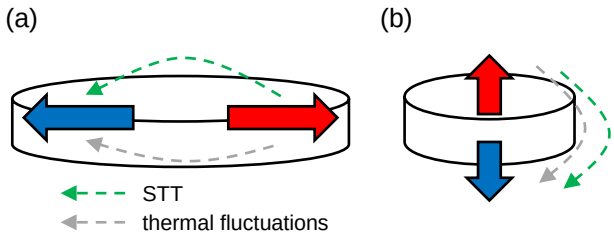


Figure 1.8: Comparison of switching between (a) i-MTJ and (b) p-MTJ.

under rapid operation since current flows directly through the MTJ. Also, the insulating nature of the tunnel barrier substantially increases the required write voltage.

### 1.2.4 Spin-Orbit Torque MRAM (SOT-MRAM)

Another way to generate spin-torque besides STT is through SOT. It utilizes the SOI at the interface of heavy metal (HM) and FM bilayers via mechanisms such as the Rashba effect [47] and spin Hall effect (SHE) [48]. Most studies take the SHE as the dominant physics of SOT, though the real contribution from both effects remains unclear. In this dissertation, only the SHE is considered as well. When a current is injected into the HM layer through SHE, a spin current is injected out-of-plane into the FM layer with in-plane spin polarization (Fig. 1.9).

The relation between the spin current ($I_s$) and the charge current ($I_c$) is expressed

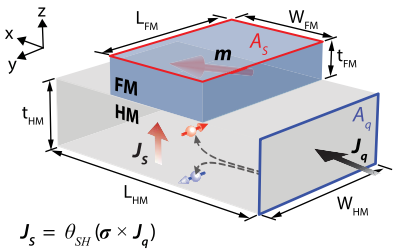


Figure 1.9: Spin Hall effect in HM/FM bilayer structure. Adapted from Ref. [7]. © 2016 IEEE.

as $I_s = \theta_{SH}(A_{FM}/A_{HM})I_c$, or $J_s = \theta_{SH}J_c$ for spin current density ($J_s$) and the charge current density ($J_c$). $\theta_{SH}$ is the spin-Hall angle that defines the ratio of $J_s$ to $J_c$. $A_{FM}$ and $A_{HM}$ are the areas of the FM and HM layers that carry the spin current and charge current, respectively. The $I_s/I_c$ ratio can be greater than 1 if $A_{FM}$ is larger than $A_{HM}$ which is much larger than the STT efficiency (the maximum is 100%). SOT is a more efficient way to generate spin current than STT since the electrons travel parallel to the interface, enabling each electron to undergo multiple spin-flip scatterings [49]. In SOT-MRAM, there is no barrier reliability issue since no charge current flows through the MTJ. The impedance is determined by the HM layer and is much lower than that of the MTJ. Therefore, SOT-MRAM is more energy-efficient than STT-MRAM [15].

Three types of SOT switching can be defined depending on the relative direction between the easy axis of the free layer and the current direction [8]; the switching mechanisms are different among these three types. Fig. 1.10(b) shows the SOT switching in i-MTJ where the easy axis is collinear with the spin polarization. The switching mechanism is the same as the STT switching in i-MTJ, and the critical current density is the same as Eq. (1.1) with $\eta$ replaced by $\theta_{SH}$. In this case, a smaller damping is preferred because the critical current is proportional to it. However, as long as the easy axis is not collinear with the spin polarization, a small applied field is needed to break the switching symmetry [49]. Here, only the SOT switching in p-MTJ will be discussed (Fig. 1.10(a)). The SOT switching in p-MTJ is a two-stage operation. First, SOT switches $\mathbf{m}$ to an intermediate state under the symmetry breaking field [50, 51], and then switching completes through relaxation when the current is removed. We learned that p-MTJ is, in general, better than i-MTJ, so achieving a field-free SOT

switching in p-MTJ remains a hot topic for both academia and industry. It is worth noted that the critical current density of SOT switching in p-MTJ does not depends on damping [50, 52]. Besides, low damping may lead to unsuccessful switching [52–54] which will be discussed in Ch. 5.

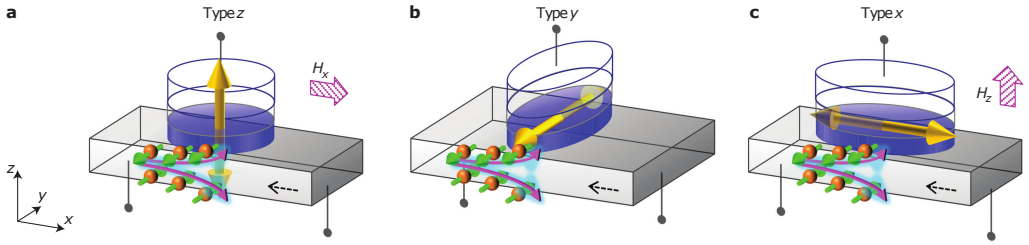


Figure 1.10: Different types of SOT switching. Adapted from Ref. [8]. © 2016, Nature Publishing Group.

## 1.3 Thesis Outline

The goal of this dissertation is to focus on addressing the challenges faced in both HDDs and SOT-MRAM, particularly from magnetization dynamics through micromagnetic simulation.

- The principles of micromagnetics and the simulation models for recording are described in **Chapter 2**.
- In **Chapter 3**, the relationship between noise power and the linear density in HAMR is studied. The competition between transition noise and remanence noise leads to a noise plateau at a certain linear density which can be controlled through the temperature gradient of the heat spot.
- A new read head design for high density heat-assisted shingled magnetic recording is studied in **Chapter 4**. By rotating the read head to match the transition curvature, we show that the user density can go beyond 6 Tb/in$^2$.
- In **Chapter 5**, we study SOT switching in a PMA low damping magnetic insulator. Techniques to avoid unsuccessful SOT switching due to the low damping are discussed.

- **Chapter 6** follows the conclusion in **Chapter 5** that in-plane SOT switching can benefit from low damping. A composite-free layer SOT-MRAM with write energy of tens of attojoules is proposed.

- Finally, **Chapter 7** summarizes the important discoveries in this dissertation and discusses the future direction for HAMR and SOT-MRAM.

# Chapter 2

# Modeling Methods

## 2.1 Micromagnetics

Micromagnetics is the study of magnetic behavior at sub-micrometer and nanometer scales. The theoretical basis of micromagnetics was established by William Fuller Brown Jr. in the 1960s [55]. Early research in micromagnetics was mostly analytical derivations of the equilibrium state of magnetization or simplified magnetization dynamics under strong assumptions. The first numerical study of two-dimensional domain wall structures was published by A. E. LaBonte in 1969 [56]. In 1987, R. H. Victora was the first to adopt a dynamical approach to the study of hysteretic phenomena in three-dimensional systems [57], although numerical simulations of realistic systems were still limited by the computers of that time. Today, with the help of modern computers, computational micromagnetics has become a useful tool for studying magnetization dynamics in systems like magnetic recording, magnetic sensors, and MRAM. Recent advances in graphics processing units for scientific computing have enabled the further acceleration of complicated micromagnetic problem solutions.

Micromagnetics is a semiclassical continuum theory. The quantum mechanics spins ($\mathbf{S}$) are replaced by a continuous vector field $\mathbf{M}(\mathbf{r}, t)$ which describes the magnetization in a material as a function of space ($\mathbf{r}$) and time ($t$). Due to the strong exchange interaction and the continuum approximation, the magnetization magnitude is assumed to be equal to the saturation magnetization $M_s$ where $\|\mathbf{M}(\mathbf{r}, t)\| = M_s$. The direction of the $\mathbf{M}$ can be defined as a unit vector $\mathbf{m} = m_x\,\hat{i} + m_y\,\hat{j} + m_z\,\hat{k}$ where $\mathbf{m} \equiv \mathbf{M}/M_s$

and $\|\mathbf{m}\| = 1$. The equilibrium of a magnetic system is obtained by minimizing its free energy with respect to the magnetization. The magnetization dynamics are described by the Landau–Lifshitz–Gilbert (LLG) equation which is the equation of motion of the magnetization.

In this section, the basic principles of micromagnetics will be provided. More details on micromagnetics and magnetization dynamics can be found in Ref. [58–60]. Unless indicated otherwise, the equations in this section are written in CGS units.

### 2.1.1 Micromagnetics Energies

The free energy ($E$) of a magnetic system determines the static and the dynamic behavior of the magnetization. Typical contributions to free energy are discussed below.

#### Zeeman Energy ($E_{zee}$)

Zeeman energy is the potential energy of a magnetic moment in an external magnetic field ($\mathbf{H}_{app}$). It is given by:

$$E_{zee} = -\int_V M_s\, \mathbf{m} \cdot \mathbf{H}_{app}\, dV \tag{2.1}$$

#### Anisotropy Energy ($E_{ani}$)

The magnetic material is said to have magnetic anisotropy if the magnetization tends to align in certain directions. The anisotropy energy is defined as the energy cost for the magnetic moment to move away from easy directions. The sources of magnetic anisotropy can be either intrinsic (e.g., magnetocrystalline anisotropy) or extrinsic (e.g., magnetoelastic anisotropy and interfacial magnetic anisotropy). There is also shape anisotropy which originates from a demagnetizing field or the magnetic dipole-dipole interaction; this will be discussed with demagnetization energy. In this dissertation, only anisotropy with a uniaxial anisotropy form is considered.

**Magnetocrystalline Anisotropy** The crystal structure determines the preferential directions of magnetization as a result of SOI. There are mainly two types of magnetocrystalline anisotropy: uniaxial and cubic.

- Uniaxial anisotropy occurs in a hexagonal or tetragonal crystal. For a system with an easy axis along $z$-axis, $E_{ani}$ is written as

$$E_{ani} = \int_V (K_{u0} + K_{u1} \sin^2\theta + K_{u2} \sin^4\theta + \cdots)\, dV, \tag{2.2}$$

  where $K_u$ are uniaxial anisotropy constants in units of energy per volume. $\theta$ is the angle between $z$-axis and $\mathbf{m}$. Since the contributions from higher order terms are typically weak, $E_{ani}$ is often represented as

$$E_{ani} = \int_V (K_u \sin^2\theta)\, dV, \tag{2.3}$$

  where the constant parts are neglected. For a positive $K_u$, the magnetization tends to align along the $\pm z$-axis (easy axis), while for a negative $K_u$, the magnetization tends to lie in the $x-y$ plane (easy plane). It is also possible to have an easy cone if higher ordered terms are considered. A more general form of uniaxial anisotropy is expressed as

$$E_{ani} = \int_V K_u[1 - (\hat{u} \cdot \mathbf{m})^2]\, dV, \tag{2.4}$$

  where $\hat{u}$ is the unit vector along the easy axis.

- Cubic anisotropy occurs in a cubic crystal. The $E_{ani}$ is expressed as

$$E_{ani} = \int_V [K_{c0} + K_{c1}(m_x^2 m_y^2 + m_y^2 m_z^2 + m_z^2 m_x^2) + K_{c2} m_x^2 m_y^2 m_z^2 + \cdots]\, dV, \tag{2.5}$$

  where $K_c$ are cubic anisotropy constants in units of energy per volume. The preferred direction of magnetization is along $\pm x$-axis, $\pm y$-axis, and $\pm z$-axis if $K_{c1} > 0$ and higher order terms are discarded.

**Interfacial Magnetic Anisotropy** In magnetic thin film multilayer structures, inversion symmetry is broken at the interfaces. This broken inversion symmetry gives rise to a uniaxial perpendicular anisotropy at the interfaces. The interfacial magnetic anisotropy in different material systems has different origins. For the CoFeB-MgO MTJ, which is widely used in MRAM devices, the interfacial PMA is partially attributed to the hybridization of $3d$ orbitals in Co and Fe and $2p$ orbitals in O at the interface [61].

**Exchange Energy ($E_{ex}$)**

Exchange interaction is a quantum mechanical effect. The exchange interaction between two neighboring spins can be described by the Heisenberg model with the Hamiltonian ($\mathcal{H}$) written as:

$$\mathcal{H} = -J\mathbf{S}_i \cdot \mathbf{S}_j, \tag{2.6}$$

where the $\mathbf{S}_i$ and $\mathbf{S}_j$ are spin angular momentum operators at site $i$, and $j$, and $J$ is the exchange integral. The neighboring two spins are ferromagnetically coupled if $J > 0$ while they are antiferromagnetically coupled if $J < 0$.

For a semiclassical analogy, the exchange energy at site $i$ is expressed as

$$\begin{aligned} E_{ex,i} &= -J \sum_{i \neq j} \mathbf{S}_i \cdot \mathbf{S}_j \\ &= -J \sum_{i \neq j} 1 - \frac{1}{2}(\mathbf{S}_i - \mathbf{S}_j)^2, \end{aligned} \tag{2.7}$$

assuming an isotropic exchange interaction. In the continuum approximation, $\mathbf{S}_i$ and $\mathbf{S}_j$ are replaced by $\mathbf{S}(\mathbf{r})$ and $\mathbf{S}(\mathbf{r} + \Delta\mathbf{r})$ where $\Delta\mathbf{r}$ is the distance vector between two neighboring spins. Eq. (2.7) becomes

$$\begin{aligned} E_{ex} &= -J \sum_{n.n} [1 - \frac{1}{2}(\mathbf{S}(\mathbf{r}) - \mathbf{S}(\mathbf{r} + \Delta\mathbf{r}))^2] \\ &= -J \sum_{n.n} [1 - \frac{1}{2}(\mathbf{S}(\mathbf{r}) - \mathbf{S}(\mathbf{r}) - \Delta\mathbf{r} \cdot \nabla\mathbf{S}(\mathbf{r}) - ...)^2] \\ &\approx -J \sum_{n.n} [1 - \frac{1}{2}(\Delta\mathbf{r} \cdot \nabla\mathbf{S}(\mathbf{r}))^2]. \end{aligned} \tag{2.8}$$

For a simple cubic lattice system with lattice constant $a$, $\mathbf{r}$ equals $(\pm a, 0, 0)$, $(0, \pm a, 0)$, or $(0, 0, \pm a)$. $\mathbf{S}$ is replaced by $S\mathbf{m}$ where $S$ is the spin magnitude. By neglecting the

constant term and considering the nearest neighbors only, Eq. (2.8) becomes

$$\begin{aligned} E_{ex} &= \frac{1}{2} JS^2 \sum_{n.n} [(\Delta \mathbf{r} \cdot \nabla \mathbf{m}(\mathbf{r}))^2] \\ &= \frac{1}{2} JS^2 \sum_{n.n} [(\Delta \mathbf{r} \cdot \nabla m_x))^2 + (\Delta \mathbf{r} \cdot \nabla m_y))^2 + (\Delta \mathbf{r} \cdot \nabla m_z))^2] \\ &= JS^2 a^2 [(\nabla m_x))^2 + (\nabla m_y))^2 + (\nabla m_z))^2]. \end{aligned} \tag{2.9}$$

With the volume $V = a^3$ of the unit cell in a simple cubic lattice, the energy density can be written as

$$\frac{E_{ex}}{V} = A_{ex}[(\nabla m_x)^2 + (\nabla m_y)^2 + (\nabla m_z)^2], \tag{2.10}$$

where $A_{ex} = JS^2/a$ is the exchange stiffness constant in units of energy per length. Despite the fact that Eq. (2.10) is derived from an isotropic simple cubic lattice, it can be applied to other systems with minor modification. Finally, the general form of exchange energy is expressed as

$$\begin{aligned} E_{ex} &= \int_V A_{ex}[(\nabla m_x)^2 + (\nabla m_y)^2 + (\nabla m_z)^2]\, dV \\ &= \int_V A_{ex}(\nabla \mathbf{m})^2\, dV. \end{aligned} \tag{2.11}$$

**Demagnetization Energy ($E_{dem}$)**

The demagnetizating field ($\mathbf{H}_{dem}$) (inside the magnet) or the stray field (outside the magnet) originates from long-range magnetic dipole-dipole interactions. The $\mathbf{H}_{dem}$ can be calculated from Maxwell's equations with no electric currents (magnetostatics):

$$\nabla \cdot \mathbf{B} = 0, \tag{2.12}$$

$$\nabla \times \mathbf{H}_{dem} = 0, \tag{2.13}$$

where the magnetic flux density $\mathbf{B}$ equals

$$\mathbf{B} = \mathbf{H}_{dem} + 4\pi \mathbf{M}. \tag{2.14}$$

Because $\mathbf{H}_{dem}$ is conservative ($\nabla \times \mathbf{H}_{dem} = 0$), there exists a scalar potential $U$ such that $\mathbf{H}_{dem} = -\nabla U$. Eq. (2.12) becomes a set of Poisson's equations:

$$\begin{cases} \Delta U = 4\pi \nabla \cdot \mathbf{M} & \text{inside the magnet} \\ \Delta U = 0 & \text{outside the magnet} \end{cases}, \tag{2.15}$$

and the boundary condition at the surface satisfies

$$\begin{cases} \mathbf{n} \cdot (\mathbf{H}_{dem,out} - \mathbf{H}_{dem,in}) = 4\pi \mathbf{n} \cdot \mathbf{M} \\ \mathbf{n} \times (\mathbf{H}_{dem,out} - \mathbf{H}_{dem,in}) = \mathbf{0} \end{cases}, \tag{2.16}$$

where $\mathbf{H}_{dem,out}$ is $\mathbf{H}_{dem}$ outside the magnet, $\mathbf{H}_{dem,in}$ is $\mathbf{H}_{dem}$ inside the magnet, and $\mathbf{n}$ is the surface normal. The solution of $U$ at $\mathbf{r}$ is

$$U(\mathbf{r}) = -\int_{volume} \frac{\nabla' \cdot \mathbf{M}(\mathbf{r}')}{|\mathbf{r} - \mathbf{r}'|}\, dV' + \int_{surface} \frac{\mathbf{n} \cdot \mathbf{M}(\mathbf{r}')}{|\mathbf{r} - \mathbf{r}'|}\, d\mathbf{S}', \tag{2.17}$$

where $\mathbf{r}'$ is the variable to be integrated. Although there are no real magnetic charges, the $-\nabla' \cdot \mathbf{M}(\mathbf{r}')$ term is usually called the magnetic volume charges, and $\mathbf{n} \cdot \mathbf{M}(\mathbf{r}')$ is called the magnetic surface charges. The $\mathbf{H}_{dem}(\mathbf{r})$, which equals $-\nabla U$, is

$$\mathbf{H}_{dem}(\mathbf{r}) = -\int_{volume} \frac{\nabla' \cdot \mathbf{M}(\mathbf{r}')(\mathbf{r} - \mathbf{r}')}{|\mathbf{r} - \mathbf{r}'|^3}\, dV' + \int_{surface} \frac{\mathbf{n} \cdot \mathbf{M}(\mathbf{r}')(\mathbf{r} - \mathbf{r}')}{|\mathbf{r} - \mathbf{r}'|^3}\, d\mathbf{S}'. \tag{2.18}$$

The $\mathbf{H}_{dem}$ in the solid leads to shape anisotropy and the formation of magnetic domains.

By using the divergence theorem and the fact that $\nabla \cdot (\psi \mathbf{A}) = \psi \nabla \cdot \mathbf{A} + (\nabla \psi) \cdot \mathbf{A}$, Eq. (2.17) can be rewritten as

$$\begin{aligned} U(\mathbf{r}) &= \int_{volume} [-\frac{\nabla' \cdot \mathbf{M}(\mathbf{r}')}{|\mathbf{r} - \mathbf{r}'|} + \nabla' \cdot (\frac{\mathbf{M}(\mathbf{r}')}{|\mathbf{r} - \mathbf{r}'|})]\, dV' \\ &= \int_{volume} \nabla' (\frac{1}{|\mathbf{r} - \mathbf{r}'|}) \cdot \mathbf{M}(\mathbf{r}')\, dV'. \end{aligned} \tag{2.19}$$

Eq. (2.18) becomes

$$\begin{aligned}\mathbf{H}_{dem}(\mathbf{r}) &= -\nabla U \\ &= -\int_{volume} \nabla\nabla'(\frac{1}{|\mathbf{r}-\mathbf{r}'|}) \cdot \mathbf{M}(\mathbf{r}')\, dV', \\ &= -\int_{volume} \mathcal{N}(\mathbf{r}-\mathbf{r}') \cdot \mathbf{M}(\mathbf{r}')\, dV',\end{aligned} \tag{2.20}$$

where

$$\mathcal{N} = \nabla\nabla'(\frac{1}{|\mathbf{r}-\mathbf{r}'|}) \tag{2.21}$$

is the demagnetizing tensor. $\mathcal{N}$ has the form

$$\mathcal{N} = \begin{bmatrix} N_{xx} & N_{xy} & N_{xz} \\ N_{yx} & N_{yy} & N_{yz} \\ N_{zx} & N_{zy} & N_{zz} \end{bmatrix}. \tag{2.22}$$

For a single domain ellipsoid, the tensor $\mathcal{N}$ becomes a $3 \times 3$ diagonal matrix with $N_{xx} + N_{yy} + N_{zz} = 4\pi$. The $\mathbf{H}_{dem} = -M_s(N_{xx}m_x\,\hat{i} + N_{yy}m_y\,\hat{j} + N_{zz}m_z\,\hat{k})$. For a perfect thin film $N_{zz} = 4\pi$, and $\mathbf{H}_{dem} = -4\pi M_s m_z\,\hat{k}$ with an effective shape anisotropy constant of $2\pi M_s^2$.

Finally, the corresponding demagnetization energy is written as

$$E_{dem} = -\frac{1}{2}\int_V M_s\,\mathbf{m} \cdot \mathbf{H}_{dem}\, dV, \tag{2.23}$$

where the factor $1/2$ is introduced to avoid double-counting.

### Antisymmetric Exchange Energy ($E_{dmi}$)

Antisymmetric exchange, also known as the Dzyaloshinskii–Moriya interaction (DMI) [62, 63], favors a chiral arrangement between neighboring magnetic moments that is unlike the Heisenberg exchange. DMI is the source for chiral spin textures such as magnetic skyrmions and chiral domain walls. The Hamiltonian ($\mathcal{H}$) of DMI is written as

$$\mathcal{H} = -\mathbf{D}_{i,j} \cdot (\mathbf{S}_i \times \mathbf{S}_j), \tag{2.24}$$

where $\mathbf{D}_{i,j}$ is the DMI vector, and its direction depends on symmetry of the crystal structure [63]. In a bulk material, such as the B20 compound, the lack of inversion symmetry in the crystal structure gives rise to DMI. This kind of DMI is called bulk DMI (Fig. 2.1(a)). DMI can also occur at the interface between different materials. For a magnetic material-heavy metal bilayer structure, the neighboring spins in the magnetic layer couple with each other through an atom in the heavy metal that has a large spin-orbit coupling (SOC) (Fig. 2.1(b)). This three-site coupling gives rise to interfacial DMI [64].

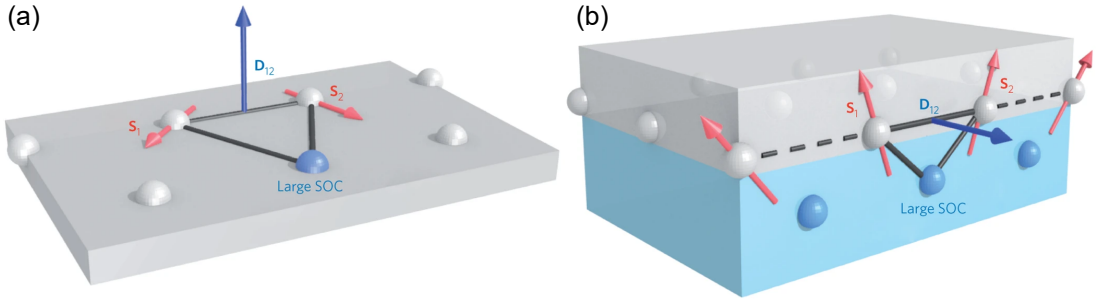


Figure 2.1: (a) Bulk and (b) interfacial DMI. In both cases, two neighboring spins (gray) $\mathbf{S}_1$ and $\mathbf{S}_2$ couple to each other through an atom with a strong SOC (blue). Adapted from Ref. [9]. © 2013, Nature Publishing Group.

Unlike bulk DMI, where the chiral spin texture only exists at low temperatures, the interfacial DMI can stabilize the texture at room temperature. Also, the strength of the interfacial DMI can be easily modified by changing the material combinations and varying the thickness of the magnetic layer. The $\mathbf{D}_{i,j}$ for interfacial DMI has the form

$$\mathbf{D}_{i,j} = d(\hat{r} \times \hat{u}_n), \tag{2.25}$$

where $d$ is a constant, $\hat{r}$ is a unit vector pointing from $\mathbf{S}_i$ to $\mathbf{S}_j$, and $\hat{u}_n$ is the interface normal.

Similar to the Heisenberg exchange (Sec. 2.1.1), Eq. (2.24) can be translated into a

continuum model with respect to $\mathbf{m}$

$$\begin{aligned} E_{dmi} &= \frac{1}{2}\sum_i S^2 d(\hat{r}\times\hat{u}_n)\cdot[\mathbf{m}(\mathbf{r})\times\mathbf{m}(\mathbf{r}+\Delta\mathbf{r})] \\ &\approx \frac{1}{2}\sum_i S^2 d(\hat{r}\times\hat{u}_n)\cdot[\mathbf{m}(\mathbf{r})\times(\mathbf{m}(\mathbf{r})+\Delta\mathbf{r}\cdot\nabla\mathbf{m}(\mathbf{r})] \\ &= \frac{1}{2}\sum_i S^2 d\{(\hat{r}\cdot\mathbf{m})[\hat{u}_n\cdot(\mathbf{m}+\Delta\mathbf{r}\cdot\nabla\mathbf{m})]-[\hat{r}\cdot(\mathbf{m}+\Delta\mathbf{r}\cdot\nabla\mathbf{m})](\hat{u}_n\cdot\mathbf{m})\} \\ &= \frac{1}{2}\sum_i S^2 d\{(\hat{r}\cdot\mathbf{m})[\hat{u}_n\cdot(\Delta\mathbf{r}\cdot\nabla\mathbf{m})]-[\hat{r}\cdot(\Delta\mathbf{r}\cdot\nabla\mathbf{m})](\hat{u}_n\cdot\mathbf{m})\}. \end{aligned} \tag{2.26}$$

For a simple cubic lattice with lattice constant $a$, the energy density of DMI can be written as

$$\frac{E_{dmi}}{V} = D[\mathbf{m}\cdot\nabla(\hat{u}_n\cdot\mathbf{m})-(\nabla\cdot\mathbf{m})(\hat{u}_n\cdot\mathbf{m})], \tag{2.27}$$

where $D$ is the micromagnetic DMI constant in units of energy per area and $D$ is a function of $d$, $S$, and $a$. The more general form of DMI in a continuum approximation for different symmetry classes can be defined by Lifshitz invariants [65, 66].

Considering a magnetic thin film with interface normal along the $z$-axis, and $\partial\mathbf{m}/\partial z = 0$, Eq. (2.27) can be further simplified as

$$\begin{aligned} \frac{E_{dmi}}{V} &= D[(m_x\frac{\partial m_z}{\partial x}-m_z\frac{\partial m_x}{\partial x})+(m_y\frac{\partial m_z}{\partial y}-m_z\frac{\partial m_y}{\partial y})] \\ &= D[(\mathbf{m}\times\partial_y\mathbf{m})_x-(\mathbf{m}\times\partial_x\mathbf{m})_y]. \end{aligned} \tag{2.28}$$

Eq. (2.28) is the typical equation used to describe the interfacial DMI with $z$-axis as the interface normal. The corresponding energy is given as

$$E_{dmi} = \int_V D[(\mathbf{m}\times\partial_y\mathbf{m})_x-(\mathbf{m}\times\partial_x\mathbf{m})_y]\,dV. \tag{2.29}$$

In the rest of the dissertation, only this form of DMI is considered.

### Other Energy Contributions

Other interactions can contribute to $E$ such as the interlayer-exchange energy originating from the RKKY interaction and magnetostrictive energy which couples magnetization

with mechanical force.

### 2.1.2 Static Micromagnetics

The purpose of static micromagnetics is to find the configuration of $\mathbf{m}$ at equilibrium by minimizing the magnetic free energy $E$. The minima of the $E$ can be found from the calculus of variations. The solution satisfies the condition that

$$\mathbf{m} \times \frac{\delta E}{\delta \mathbf{m}} = \mathbf{0}, \tag{2.30}$$

which is known as Brown's equation [55].

#### Effective Field

Here the effective field ($\mathbf{H}_{eff}$) is introduced as the functional derivative of the free energy density with respect to $\mathbf{M}$

$$\mathbf{H}_{eff} = -\frac{1}{M_s V}\frac{\delta E}{\delta \mathbf{m}}. \tag{2.31}$$

Each interaction that contributes to the free energy behaves as a magnetic field experienced by the local magnetic moment. $\mathbf{H}_{eff}$ is the sum of applied field ($\mathbf{H}_{app}$), anisotropy field ($\mathbf{H}_{ani}$), exchange field ($\mathbf{H}_{ex}$), demagnetizing field ($\mathbf{H}_{dem}$), DMI field ($\mathbf{H}_{dmi}$), etc. The expressions for commonly used fields are shown below:

- Uniaxial anisotropy field

$$\mathbf{H}_{ani} = -\frac{1}{M_s V}\frac{\delta E_{ani}}{\delta \mathbf{m}} = \frac{2K_u}{M_s}[(\hat{u}\cdot\mathbf{m})\hat{u}], \tag{2.32}$$

- Exchange field

$$\mathbf{H}_{ex} = -\frac{1}{M_s V}\frac{\delta E_{ex}}{\delta \mathbf{m}} = \frac{2}{M_s}\nabla\cdot(A_{ex}\nabla\mathbf{m}) = \frac{2A_{ex}}{M_s}\nabla^2\mathbf{m}, \tag{2.33}$$

- Interfacial DMI field

$$\mathbf{H}_{dmi} = -\frac{1}{M_s V}\frac{\delta E_{dmi}}{\delta \mathbf{m}} = \frac{2D}{M_s}[-\frac{\partial m_z}{\partial x}\hat{i} - \frac{\partial m_z}{\partial y}\hat{j} + (\frac{\partial m_x}{\partial x} + \frac{\partial m_y}{\partial y})\hat{k}]. \tag{2.34}$$

Eq. (2.30) becomes

$$\mathbf{m} \times \mathbf{H}_{eff} = \mathbf{0}, \tag{2.35}$$

indicating that at equilibrium, the torque exerted on the local magnetic moment by the effective field is zero.

### Boundary Conditions

The boundary conditions can be obtained from the variations of free energy as well. For the energies term discussed above, only the exchange interaction and the DMI contribute to boundary conditions.

The boundary condition from the exchange interaction is given as

$$\mathbf{m} \times 2A_{ex}\frac{\partial \mathbf{m}}{\partial \mathbf{n}} = \mathbf{0} \qquad \text{or} \qquad \frac{\partial \mathbf{m}}{\partial \mathbf{n}} = 0, \tag{2.36}$$

where $\mathbf{n}$ is the surface normal. This is the boundary condition that satisfies most of the systems without DMI.

The boundary condition from the interfacial DMI is given as

$$\mathbf{m} \times [-D(\hat{u}_n \times \mathbf{n}) \times \mathbf{m}] = \mathbf{0}. \tag{2.37}$$

The joint boundary condition in the presence of exchange interaction and DMI is the summation of Eq. (2.36) and Eq. (2.37),

$$\mathbf{m} \times [2A_{ex}\frac{\partial \mathbf{m}}{\partial \mathbf{n}} - D(\hat{u}_n \times \mathbf{n}) \times \mathbf{m}] = \mathbf{0}, \tag{2.38}$$

which indicates

$$2A_{ex}\frac{\partial \mathbf{m}}{\partial \mathbf{n}} - D(\hat{u}_n \times \mathbf{n}) \times \mathbf{m} = \mathbf{0}. \tag{2.39}$$

The final expression of the boundary conditions is

$$\frac{\partial \mathbf{m}}{\partial \mathbf{n}} = \frac{D}{2A_{ex}}(\hat{u}_n \times \mathbf{n}) \times \mathbf{m}. \tag{2.40}$$

The magnetic system must satisfy the boundary conditions. Other boundary conditions, such as surface anisotropy, may be applied depending on the system. A periodic

boundary condition is often used if no surface exists in the system.

### 2.1.3 Dynamic Micromagnetics

If the magnetic system is not at an equilibrium state, the magnetization will evolve in time in response to $\mathbf{H}_{eff}$.

#### Landau–Lifshitz Equation

In 1935, Landau and Lifshitz first proposed an equation to describe magnetization dynamics [67]:

$$\frac{\partial \mathbf{m}}{\partial t} = -\gamma \mathbf{m} \times \mathbf{H}_{eff}, \tag{2.41}$$

where $\gamma$ is the gyromagnetic ratio. For electron spin, $\gamma = 1.76 \times 10^7$ rad·Oe$^{-1}$·s$^{-1}$. It represents the precession motion of $\mathbf{m}$ about $\mathbf{H}_{eff}$, and the energy in the system is conserved. However, magnetic energy loss is inevitable in a real system. Landau and Lifshitz introduced a dimensionless phenomenological damping parameter $\lambda$ to include the dissipative process, and Eq. (2.41) becomes

$$\frac{\partial \mathbf{m}}{\partial t} = -\gamma \mathbf{m} \times \mathbf{H}_{eff} - \lambda \mathbf{m} \times (\mathbf{m} \times \mathbf{H}_{eff}), \tag{2.42}$$

which is the final form of the Landau–Lifshitz (LL) Equation. With the damping term, the direction of $\mathbf{m}$ will eventually align with $\mathbf{H}_{eff}$. At equilibrium, $\partial \mathbf{m}/\partial t = 0$, suggesting the satisfaction of Eq. (2.35) that $\mathbf{m} \times \mathbf{H}_{eff} = \mathbf{0}$.

#### Landau–Lifshitz–Gilbert Equation

In 1955, Gilbert derived an equation for magnetization dynamics [68]

$$\frac{\partial \mathbf{m}}{\partial t} = -\gamma \mathbf{m} \times \mathbf{H}_{eff} + \alpha \mathbf{m} \times \frac{d\mathbf{m}}{dt}, \tag{2.43}$$

where $\alpha$ is the Gilbert damping constant. It has a form similar to Eq. (2.42) but has a different expression for the damping term. By applying the cross product to Eq. (2.43) with $\mathbf{m}$ and the fact that $\mathbf{m} \cdot d\mathbf{m}/dt = 0$, it can be shown that Eq. (2.43) can be rewritten

as

$$\frac{\partial \mathbf{m}}{\partial t} = -\frac{\gamma}{1+\alpha^2}\mathbf{m} \times \mathbf{H}_{eff} - \frac{\gamma\alpha}{1+\alpha^2}\mathbf{m} \times (\mathbf{m} \times \mathbf{H}_{eff}), \tag{2.44}$$

which has the same mathematical form as the LL equation (Eq. (2.42)). Eq. (2.43) is referred to as the Landau–Lifshitz–Gilbert (LLG) Equation and Eq. (2.44) is the LLG equation in LL form. However, the LL equation and the LLG equation may not be physically equivalent.

It can be seen that when damping is small ($\lambda$, $\alpha \to 0$), The two equations are identical. However, in the limit of infinite damping ($\lambda$, $\alpha \to \infty$), $\partial\mathbf{m}/\partial t$ approaches $\infty$ in the LL equation while $\partial\mathbf{m}/\partial t$ goes to 0 in the LLG equation. The arguments suggest that the LL equation may not be physically reasonable for large damping [69]. As a result, the LLG equation is used to describe magnetization dynamics.

Since $\mathbf{m}$ is the unit vector, it can be described in spherical coordinates:

$$\begin{aligned} m_x &= \sin\theta\cos\phi, \\ m_y &= \sin\theta\sin\phi, \\ m_z &= \cos\theta, \end{aligned} \tag{2.45}$$

where $\theta$ is the polar angle and $\phi$ is the azimuthal angle. With the $\mathbf{H}_{eff} = H_{eff,x}\,\hat{i} + H_{eff,y}\,\hat{j} + H_{eff,z}\,\hat{k}$ derived in Sec. 2.1.2, Eq. (2.44) becomes

$$\begin{aligned} \frac{d\theta}{dt} &= \frac{\gamma}{1+\alpha^2}[-\sin(\phi)H_{eff,x} + \cos(\phi)H_{eff,y}] \\ &\quad + \frac{\gamma\alpha}{1+\alpha^2}[\cos(\theta)\cos(\phi)H_{eff,x} + \cos(\theta)\sin(\phi)H_{eff,y} - \sin(\theta)H_{eff,z}], \end{aligned} \tag{2.46}$$

$$\begin{aligned} \sin(\theta)\frac{d\phi}{dt} &= \frac{\gamma}{1+\alpha^2}[-\cos(\theta)\cos(\phi)H_{eff,x} - \cos(\theta)\sin(\phi)H_{eff,y} + H_{eff,z}] \\ &\quad + \frac{\gamma\alpha}{1+\alpha^2}[-\sin(\phi)H_{eff,x} + \cos(\phi)H_{eff,y}]. \end{aligned} \tag{2.47}$$

Eq. (2.46) and Eq. (2.47) will be used in the numerical evaluation of the LLG equation.

### Finite Temperature

The thermal fluctuations due to the finite temperature can be modeled as a random thermal field $\mathbf{H}_{th}$ [70] at a given moment $t$:

$$\mathbf{H}_{th}(t) = \eta(t)\sqrt{\frac{2\alpha k_B T}{\gamma M_s \Delta V \Delta t}}, \tag{2.48}$$

where $k_B$ is the Boltzmann constant, $T$ is the temperature in Kelvin, $\Delta V$ is the volume of the unit cell, and $\Delta t$ is the time step. $\Delta V$ and $\Delta t$ are related to numerical discretization and integration. $\eta(t)$ is a random vector that follows a normal distribution in three dimensions with a mean of zero.

The total effective field becomes

$$\mathbf{H}_{eff} = -\frac{1}{M_s V}\frac{\delta E}{\delta \mathbf{m}} + \mathbf{H}_{th} \tag{2.49}$$

### Spin-Transfer Torque and Spin-Orbit Torque

To describe the STT and the SOT for a magnetic thin film, an additional torque $\mathbf{T}$ is added to the LLG equation:

$$\frac{\partial \mathbf{m}}{\partial t} = -\gamma \mathbf{m} \times \mathbf{H}_{eff} + \alpha \mathbf{m} \times \frac{d\mathbf{m}}{dt} + \mathbf{T}. \tag{2.50}$$

$\mathbf{T}$ has the form

$$\mathbf{T} = -\eta_{DL}\frac{\gamma \hbar J}{2|e|M_s t}\mathbf{m} \times (\mathbf{m} \times \mathbf{p}) - \eta_{FL}\frac{\gamma \hbar J}{2|e|M_s t}\mathbf{m} \times \mathbf{p}. \tag{2.51}$$

The first term is usually referred to as damping-like torque (DLT) and the second term is known as field-like torque (FLT) since they have a form similar to Eq. (2.44). $\eta_{DL}$ and $\eta_{FL}$ are DLT efficiency and FLT efficiency, respectively. $\hbar$ is the reduced Planck constant, $J$ is the applied current density, $e$ is the elementary charge, $t$ is the film thickness, and $\mathbf{p}$ is the unit vector along the spin polarization direction of the current. $\eta_{DL}$ and $\eta_{FL}$ are related to spin polarization for STT and related to spin Hall angle for SOT.

Despite the fact that spin torques are not fields, equivalent forms for effective fields

that are useful for numerical evaluation can still be derived from Eq. (2.51):

$$\mathbf{H}_{DL} = \eta_{DL}\frac{\hbar J}{2|e|M_s t}\mathbf{m}\times\mathbf{p}, \tag{2.52}$$

$$\mathbf{H}_{FL} = \eta_{FL}\frac{\hbar J}{2|e|M_s t}\mathbf{p}. \tag{2.53}$$

Eq. (2.50) becomes

$$\frac{\partial \mathbf{m}}{\partial t} = -\gamma\mathbf{m}\times(\mathbf{H}_{eff}+\mathbf{H}_{DL}+\mathbf{H}_{FL}) + \alpha\mathbf{m}\times\frac{d\mathbf{m}}{dt}. \tag{2.54}$$

### 2.1.4 Numerical Evaluations

The LLG equation can be solved numerically through the finite-difference method (FDM) or finite-element method. In this dissertation, FDM is considered. $\mathbf{r}$ is approximated as $\mathbf{r} \approx i\Delta x\,\hat{i} + j\Delta y\,\hat{j} + k\Delta z\,\hat{k}$, where $i$, $j$, and $k$ are position indices for the cell. $\Delta x$, $\Delta y$, and $\Delta z$ denote the discretization size along the $x$-,$y$-, and $z$-directions.

#### Exchange Length

In order to resolve the magnetic domain structure, the cell size in FDM must be smaller than the exchange length $l_{ex}$:

$$l_{ex} = \sqrt{\frac{A_{ex}}{K_{eff}}}, \tag{2.55}$$

where $K_{eff}$ is the effective anisotropy constant which comprises the crystalline anisotropy as well as the shape anisotropy. For a thin film with uniaxial anisotropy, $K_{eff} = K_u - 2\pi M_s^2$. Below the exchange length, exchange interaction dominates the system and thus the cell magnetization is saturated.

### Exchange Field and DMI Field

The first and second order derivatives of $\mathbf{m}$ at site $(i, j, k)$ along the $x$-direction are approximated as

$$\frac{\partial \mathbf{m}(i,j,k)}{\partial x} \approx \frac{\mathbf{m}(i+1,j,k) - \mathbf{m}(i-1,j,k)}{2\Delta x}, \tag{2.56}$$

$$\frac{\partial^2 \mathbf{m}(i,j,k)}{\partial x^2} \approx \frac{\mathbf{m}(i+1,j,k) - 2\mathbf{m}(i,j,k) + \mathbf{m}(i-1,j,k)}{\Delta x^2}. \tag{2.57}$$

Similar approximations can be applied along the $y$- and $z$-directions. As a result, the exchange field becomes (Eq. (2.33))

$$\begin{aligned}\mathbf{H}_{ex}(i,j,k) = \frac{2A_{ex}}{M_s}[&\frac{\mathbf{m}(i+1,j,k) - 2\mathbf{m}(i,j,k) + \mathbf{m}(i-1,j,k)}{\Delta x^2} \\ &+ \frac{\mathbf{m}(i,j+1,k) - 2\mathbf{m}(i,j,k) + \mathbf{m}(i,j-1,k)}{\Delta y^2} \\ &+ \frac{\mathbf{m}(i,j,k+1) - 2\mathbf{m}(i,j,k) + \mathbf{m}(i,j,k-1)}{\Delta z^2}].\end{aligned} \tag{2.58}$$

For the interfacial DMI field (Eq. (2.34)),

$$\begin{aligned}\mathbf{H}_{dmi}(i,j,k) = \frac{2D}{M_s}\{&-(\frac{m_z(i+1,j,k) - m_z(i-1,j,k)}{2\Delta x})\,\hat{i} \\ &-(\frac{m_z(i,j+1,k) - m_z(i,j-1,k)}{2\Delta y})\,\hat{j} \\ +[(\frac{m_x(i+1,j,k) - m_x(i-1,j,k)}{2\Delta x}) &+ (\frac{m_y(i,j+1,k) - m_y(i,j-1,k)}{2\Delta y}]\,\hat{k}\}.\end{aligned} \tag{2.59}$$

At the boundary ($\partial\Omega$), the missing neighboring cell in the $u$- ($u = \pm x$, $\pm y$ or $\pm z$) directions is padded with an imaginary cell $\mathbf{m} + (\partial_u \mathbf{m}|_{\partial\Omega} \cdot \Delta u)\mathbf{n}$ where $\mathbf{n}$ is the surface normal.

### Demagnetizating Field

The discrete form of Eq. (2.20) is

$$\mathbf{H}_{dem}(i,j,k) = -\sum_{i,j,k \neq i',j',k'} \mathbf{N}_{i-i',j-j',k-k'} \mathbf{M}(i',j',k'), \tag{2.60}$$

which is the discrete convolution between the discrete demagnetizing tensor $\mathbf{N}$ and $\mathbf{M}$. The expression $\mathbf{N}$ for cubic cells is derived in Ref. [71].

$$\mathbf{N}_{xx}(i,j,k,\Delta x,\Delta y,\Delta z) = -\frac{1}{\Delta x\Delta y\Delta z}\sum_{\mathbf{p},\mathbf{q}\in 0,1}\{(-1)^{\sum p_x+p_y+p_z+q_x+q_y+q_z} f[(i+p_x-q_x)\Delta x,(j+p_y-q_y)\Delta y,(k+p_z-q_z)\Delta z]\}. \quad (2.61)$$

$$\mathbf{N}_{xy}(i,j,k,\Delta x,\Delta y,\Delta z) = -\frac{1}{\Delta x\Delta y\Delta z}\sum_{\mathbf{p},\mathbf{q}\in 0,1}\{(-1)^{\sum p_x+p_y+p_z+q_x+q_y+q_z} g[(i+p_x-q_x)\Delta x,(j+p_y-q_y)\Delta y,(k+p_z-q_z)\Delta z]\}. \quad (2.62)$$

The auxiliary functions $f$ and $g$ are

$$\begin{aligned} f(x,y,z) &= \frac{|y|}{2}(z^2-x^2)\sinh^{-1}(\frac{|y|}{\sqrt{x^2+z^2}}) \\ &+ \frac{|z|}{2}(y^2-x^2)\sinh^{-1}(\frac{|z|}{\sqrt{x^2+y^2}}) \\ &- |xyz|\tan^{-1}(\frac{|yz|}{x\sqrt{x^2+y^2+z^2}}) \\ &+ \frac{1}{6}(2x^2-y^2-z^2)\sqrt{x^2+y^2+z^2}, \end{aligned} \quad (2.63)$$

$$\begin{aligned} g(x,y,z) &= (xyz)\sinh^{-1}(\frac{z}{\sqrt{x^2+y^2}}) \\ &+ \frac{y}{6}(3z^2-y^2)\sinh^{-1}(\frac{x}{\sqrt{y^2+z^2}}) \\ &+ \frac{x}{6}(3z^2-x^2)\sinh^{-1}(\frac{y}{\sqrt{x^2+z^2}}) \\ &- \frac{z^3}{6}\tan^{-1}(\frac{xy}{z\sqrt{x^2+y^2+z^2}}) - \frac{zy^2}{2}\tan^{-1}(\frac{xz}{y\sqrt{x^2+y^2+z^2}}) \\ &- \frac{zx^2}{2}\tan^{-1}(\frac{yz}{x\sqrt{x^2+y^2+z^2}}) - \frac{xy\sqrt{x^2+y^2+z^2}}{3}. \end{aligned} \quad (2.64)$$

The rest of the elements are obtained from circular permutation of the coordinates. For the diagonal elements:

$$\begin{aligned}\mathbf{N}_{yy}(i,j,k,\Delta x,\Delta y,\Delta z) &= \mathbf{N}_{xx}(j,k,i,\Delta y,\Delta z,\Delta x),\\ \mathbf{N}_{zz}(i,j,k,\Delta x,\Delta y,\Delta z) &= \mathbf{N}_{xx}(k,i,j,\Delta z,\Delta x,\Delta y).\end{aligned} \tag{2.65}$$

For the off-diagonal elements:

$$\begin{aligned}\mathbf{N}_{xz}(i,j,k,\Delta x,\Delta y,\Delta z) &= \mathbf{N}_{xy}(i,k,j,\Delta x,\Delta z,\Delta y),\\ \mathbf{N}_{yz}(i,j,k,\Delta x,\Delta y,\Delta z) &= \mathbf{N}_{xy}(j,k,i,\Delta y,\Delta z,\Delta x).\end{aligned} \tag{2.66}$$

Also, $\mathbf{N}$ is symmetric, so $\mathbf{N}_{ij} = \mathbf{N}_{ji}$.

Per the convolution theorem, the discrete convolution between $\mathbf{N}$ and $\mathbf{M}$ becomes a multiplication of their discrete Fourier transforms (DFTs) in Eq. (2.60). $\mathbf{H}_{dem}$ is obtained from the inverse DFT of the product. For a non-periodic system, Eq. (2.60) is not a cyclic convolution and thus zero-padding is needed for the DFT to give correct results [59]. The size of cells including zero-padding should be at least twice the original size. Using the fast Fourier transform (FFT) technique, the complexity to compute $\mathbf{H}_{dem}$ is reduced to $\mathcal{O}(N \log N)$, where $N$ is the number of cells [72, 73].

## 2.2 Recording Modeling

### 2.2.1 Renormalization in Micromagnetics for Heat-Assisted Magnetic Recording

Different from most micromagnetic simulations where the temperature is either at 0 K or much lower than $T_c$, simulations for HAMR are performed near $T_c$. To resolve magnetization dynamics within a grain at such high temperatures, simulation at an atomistic scale is needed. However, system-level atomistic simulation for HAMR is not feasible due to limited computational resources. To address this issue, Victora and Huang developed a modified version of LLG based on renormalization group theory [10] — multiple atomistic spins can be coarse-grained into a single renormalized block spin, followed by the fact that the correlation length of spin fluctuations becomes infinite when

temperature is close to $T_c$ (Fig. 2.2). The renormalized block spin has its own renormalized magnetic parameters: $M_{s,block}$, $K_{u,block}$, $A_{ex,block}$, and $\alpha_{block}$. The $\alpha_{block}$ can be calculated following the approach in Ref. [74]. To ensure the system does not change after renormalization, the rest of renormalized magnetic parameters should satisfy the condition that the macroscopic magnetic properties from renormalized system should be maximally equivalent to those from atomistic system at thermal equilibrium. The macroscopic magnetic properties such as the spontaneous magnetization, the anisotropy field and their standard variations in time are usually chosen since they affect the magnetization process most. It is worth noted that all renormalized magnetic parameters are temperature and renormalized scale dependent, unlike the constant values for atomistic scale parameters. This renormalized LLG technique can also be applied to different systems [75–77] as long as the operating temperature are close to $T_c$.

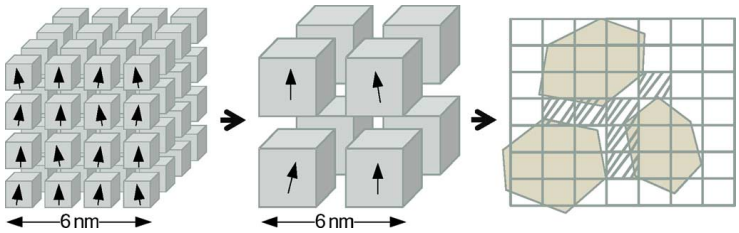


Figure 2.2: The atomistic spins are coarse-grained into larger renormalized block spins. The Voronoi grains are discretized with these renormalized block spins for micromagnetic simulation. Reprinted with permission from Ref. [10], © 2013 IEEE.

### 2.2.2 Recording Process

The granular structure of recording media is modeled as Voronoi cells (Fig. 2.3). The details for the generation of Voronoi grains with grain boundaries can be found in Ref. [78]. The Voronoi grains are then discretized into 3-D renormalized cells for micromagnetic simulations (Fig. 2.2). During the recording process, the write head with heat spot moves along the down-track direction with a velocity $v$. The corresponding temperature distribution ($T$) of the media is usually modeled as a 2-D Gaussian distribution in the $x$-$y$ plane, assuming the $T$ is uniform along $z$-direction, with known peak temperature $T_{peak}$ and full width at half maximum (FWHM). The $T$ at location $x$ (down-track)

and $y$ (cross-track) at time $t$ is expressed as

$$T(x,y,t) = T_{rt} + (T_{peak} - T_{rt})exp(\frac{-(x - x_0 - vt)^2 - (y - y_0)^2}{2\sigma^2}), \tag{2.67}$$

where $T_{rt}$ is room temperature which is 300 K, $\sigma = \text{FWHM}/(2\sqrt{2\ln 2})$, $x_0$ and $y_0$ are the initial position of the heat spot, and $t$ is the simulation time. At a given location and time, the $T$ dependent renormalized magnetic parameters are known. The corresponding $\mathbf{H}_{eff}$ can then be calculated for the LLG evolution. The same procedure is repeated until the end of the simulations.

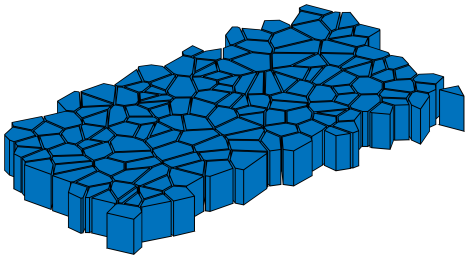

Figure 2.3: Voronoi grains with grain boundary.

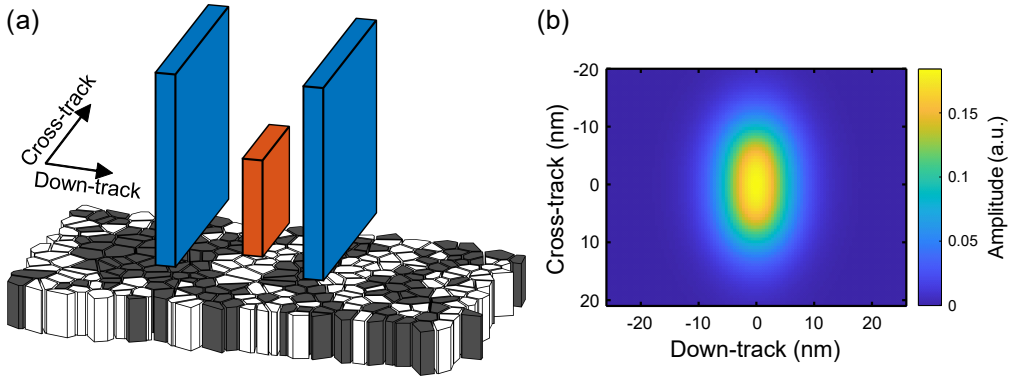


Figure 2.4: (a) Schematic of the MR read head (red), shields (blue) and a Voronoi medium with recorded bits. (b) Reader potential.

### 2.2.3 Readback Process

The reader consists of two shields along the down-track direction, and a magnetoresistive element in between. The head-media distance is the fly height. The distance between shields is called the shield-to-shield spacing (SSS). The reader width is defined along the cross-track direction. Per the reciprocity principle [24], the readback signal $V(x)$ is the cross-correlation between the reader potential and the surface charge on the media. The read head potential ($\Phi_{MR}$) can be obtained by numerically solving the 3-D Laplace's equation with boundary conditions of unit potential in the MR head and zero potential in the shields and at the bottom of the media [79,80]. The surface charge is proportional to the magnetization. $V(x)$ can be written as

$$V(x) \propto \int_{-\delta/2}^{\delta/2} \int_{-\infty}^{\infty} \Phi_{MR}(x + x', y') M_z(x', y')\, dx' dy', \tag{2.68}$$

where $\delta$ is the track width. The signal-to-noise ratio (SNR) and bit error rate (BER) can be calculated from the readback signal [78].

# Chapter 3

# Media Noise Plateau in Heat-Assisted Magnetic Recording

This chapter is based on the publication:
W.-H. Hsu and R. Victora, "Micromagnetic study of media noise plateau in heat-assisted magnetic recording," *IEEE Transactions on Magnetics*, vol. 55, no. 2, pp. 1–4, 2018.

## 3.1 Introduction

HAMR can potentially provide a high areal density of as much as 4.7 terabits/in$^2$ [33] so it serves as a likely replacement for the current PMR. However, this high-temperature process introduces additional noise; understanding and mitigating the noise are important for successful high-density HAMR recording [82–84]. In PMR, media noise power (NP) integrated over all frequencies grows linearly at a low linear density and grows superlinearly at a high linear density. In between, there is a plateau region (or relatively flat region) at an intermediate density. This noise plateau has been observed and studied in PMR, and has been explained by a tradeoff between transition noise and AC-erasure noise [85], by magnetostatic interactions [80], and by cluster cutting [86]. In this chapter, by adopting micromagnetic simulation, we observe a similar noise plateau behavior

in HAMR, and this plateau region can be manipulated by changing the temperature profile of the heat spot.

## 3.2 Methods

The renormalized stochastic LLG equation was adopted (Sec. 2.2.1). The dimension of the $L1_0$ FePt media sample was 384 nm × 48 nm × 9 nm. Voronoi grains with 6.5 ± 1.1 nm grain pitch (1 nm grain boundary) were considered. At 0 K, the $M_s$ = 1100 (emu/cm$^3$), the anisotropy constant $K_u = 7 \times 10^7$ (erg/cm$^3$), the exchange stiffness $A_{ex} = 1.1 \times 10^{-6}$ (erg/cm), the damping constant $\alpha = 0.02$ [87], and $T_c$ is about 700 K for $L1_0$ FePt. The whole medium was discretized into 1.5 nm cubic renormalized cells for micromagnetic simulation. We did not consider the effect of variation in $T_c$ ($\sigma_{T_c}$) and $H_k$ ($\sigma_{H_k}$), and there is no intergranular exchange in this chapter.

The temperature profile of the heat spot was set to be a perfect 2-D Gaussian distribution with a varied FWHM and peak temperature ($T_{peak}$) (Eq. (2.67)). The head velocity $v$ is 15 m/s throughout this chapter. The applied field ($H_{appl}$) was 10 kOe with a canting angle of 22.5°. The playback signal was obtained by the reciprocity principle with a 20 nm read head and a fly height of 5 nm unless stated otherwise (Sec. 2.2.3). The written signal was a single tone. The noise-free signal ($S_{avg}$) was obtained by averaging all playback signals from eight different ac-erased media. The NP was calculated by averaging the variance of all signals $S_i(x)$ over the signal length ($L$)

$$\mathrm{NP} = \frac{1}{L}\int_0^L \overline{\{S_i(x) - S_{avg}\}^2}dx. \tag{3.1}$$

We calculated and compared the integrated NP for various $T_{peak}$ and the FWHM of the heat spot.

## 3.3 Results and Discussion

### 3.3.1 Origin of the Noise Plateau in HAMR

In magnetic recording, jitter and nonlinear transition shift (NLTS) degrade the performance. It has been previously argued that the jitter from adjacent transitions is

positively correlated due to strong magnetostatic interaction between adjacent bits in PMR and that this results in the reduction of noise, i.e. a noise plateau is formed at intermediate density [80]. Transition jitter is defined as the standard deviation of each zero-crossing point of the playback signal, i.e. $[(1/N)\sum_{i=1}^{N}(d_i - d_m)^2]^{(1/2)}$ where $d_m$ is the averaged transition location and $N$ is the total number of transitions. In HAMR, NLTS has been observed with a sign opposite to PMR but with the same sign as the longitudinal case [88]. Our simulations show that the effect of NLTS is usually weak in HAMR. According to Ref. [24] and Ref. [89], the bit shift caused by a small change in the demagnetizing field ($\Delta H_d$) is inversely proportional to the effective field gradient $dH_{eff}/dx$, $\Delta x \propto |\Delta H_d|/(dH_{eff}/dx)$, where $dH_{eff}/dx$ is approximately equal to the applied head field gradient $dH_{app}/dx$ in PMR while it is approximately equal to the anisotropy field gradient $dH_k/dx$ in HAMR. The typical value of $|dH_{app}/dx|$ is on the

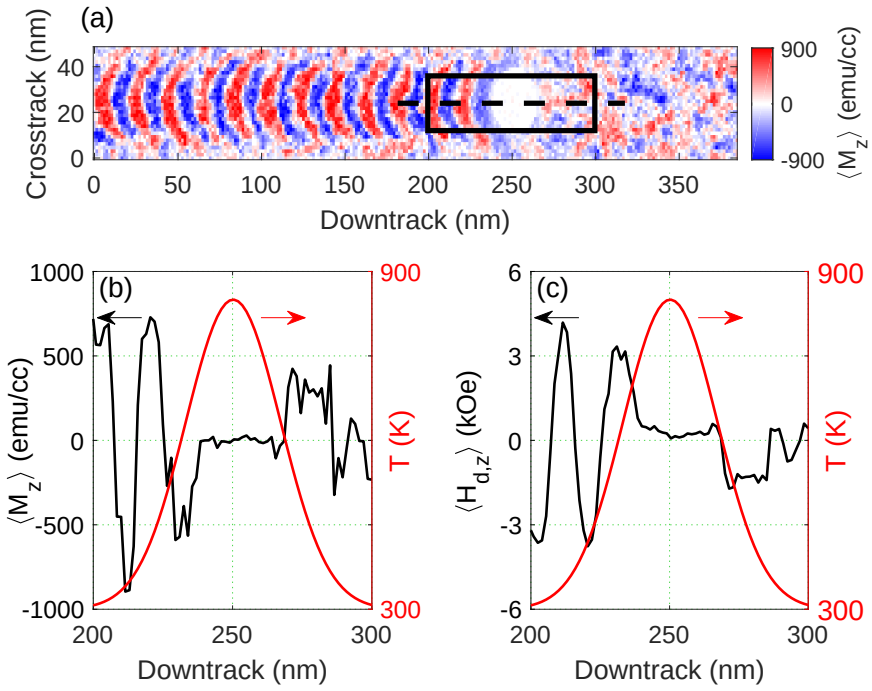


Figure 3.1: (a) The average recording pattern at the time when the direction of $H_{appl}$ is switched. The magnetization and the demagnetizing fields of the centerline along the downtrack direction in the black box are shown in (b) and (c). The red curve is the temperature profile. Both $\langle M_z \rangle$ and $\langle H_{d,z} \rangle$ vanish when the temperature is close to $T_c$

order of hundreds of Oe/nm in PMR, and $|dH_k/dx|$ is on the order of thousands of Oe/nm in HAMR. It is clear that $dH_{eff}/dx$ is about an order of magnitude larger in HAMR than it is in PMR. Therefore, the NLTS caused by $\Delta H_d$ is an order of magnitude larger in PMR than it is in HAMR. Also, the $z$-component of $|\Delta H_d|$ is about 2.5 kOe during the writing process at a linear density of 2600 kilo flux changes per inch (kfci) (Fig. 3.1), and it keeps decreasing as the density increases. Thus, $\Delta x$ due to $|\Delta H_d|$ is even smaller at high density. Therefore, we believe that the arguments in Ref. [80] are not very important for HAMR.

The breakpoint from the low-density linear region to the moderate plateau region was explained by a cluster size effect in PMR [86]. In our simulation, there is no intergranular exchange which means no cluster exists. Instead, we think the possible explanation of the plateau in HAMR is the competition between transition noise and remanence noise.

### 3.3.2 Competition between Transition Noise and Remanence Noise

Two sources contribute to the total noise in HAMR. One is the transition noise (also known as jitter), and the other is the remanence noise (also known as DC noise). The transition noise is mainly caused by $\sigma_{T_c}$, the thermal gradient of the heat spot, and the grain size distribution, while the remanence noise is mainly caused by thermal fluctuations during the cooling process. In this chapter, the only factors that can contribute to the noise are temperature profile of the heat spot, grain size distribution, and thermal fluctuations.

The cooling rate in HAMR can be written as

$$\frac{dT}{dt} = \frac{\partial T}{\partial x}\frac{dx}{dt} = \frac{\partial T}{\partial x}v, \tag{3.2}$$

where $v = dx/dt$ is the head velocity. As mentioned in Ref. [10], we want a small $dT/dt$ to eliminate the effect of thermal fluctuations, while a large $\partial T/\partial x$ is favored to get rid of the effects of grain variation. This means that the transition noise and the remanence noise are competing with each other. For a relatively low-density recording, the spacing between transitions is large, i.e. the DC-saturated region is relatively large. The number of transitions in a unit length is less than that of high recording density; the remanence

noise contributes more to the total noise in this case. In contrast, transition noise dominates in a high-density recording; the plateau is a consequence of this competition. As a result, a small $\partial T/\partial x$ leads to a plateau appearing at lower density, while a large $\partial T/\partial x$ leads to a plateau appearing at higher density.

Ref. [90] and Ref. [91] provide a more systematic study of the transition and remanence noises and show the separation of these two noises in a relatively large bit length. Nevertheless, it is hard to discern these two noises in playback signals, especially when the bit length is close to the grain size, the region we are interested in. Though this competition hypothesis is crude, it still provides insight for predicting noise behavior. Our simulation results support this idea and will be detailed below.

### 3.3.3 Noise Plateau vs FWHM

The actual write temperature ($T_w$) of FePt media depends on the cooling rate and magnetic properties of each grain [92]. Here, we take 675 K as $T_w$ for simplicity. Under a fixed $T_{peak}$ of 850 K, the temperature gradients ($\partial T/\partial x$) along the centerline at $T_w$ are approximately 25.8, 19.3, and 15.5 K/nm for FWHMs of 30, 40, and 50 nm, respectively. The greater the FWHM of a heat spot (smaller $\partial T/\partial x$), the less remanence noise is formed, but jitter is enhanced. Therefore, the plateau region should form in a relatively low recording density region for a large heat spot. We expect this plateau region to shift to the right as the FWHM decreases. These behaviors are confirmed in our simulation results (Fig. 3.2). Raw data with error bars are shown in black. The solid line represents the results from applying a Savitzky–Golay filter [93] (third-order polynomial and window size of 500 kfci) to the interpolated data.

### 3.3.4 Noise Plateau vs $T_{peak}$

Similarly, we maintained the FWHM of the heat spot at 40 nm while changing $T_{peak}$. $\partial T/\partial x$ along the centerline at $T_w$ is approximately 13.3, 19.3, and 23.2 K/nm for $T_{peak}$ of 750, 850, and 950 K, respectively. The noise plateau (Fig. 3.3) occurs in the low density region for the case with a $T_{peak}$ of 750 K and in the high density region for the case with a $T_{peak}$ of 950 K as expected. The linear density at plateau region as a function of $\partial T/\partial x$ is shown in Fig. 3.4, and it further illustrates our competition hypothesis: a

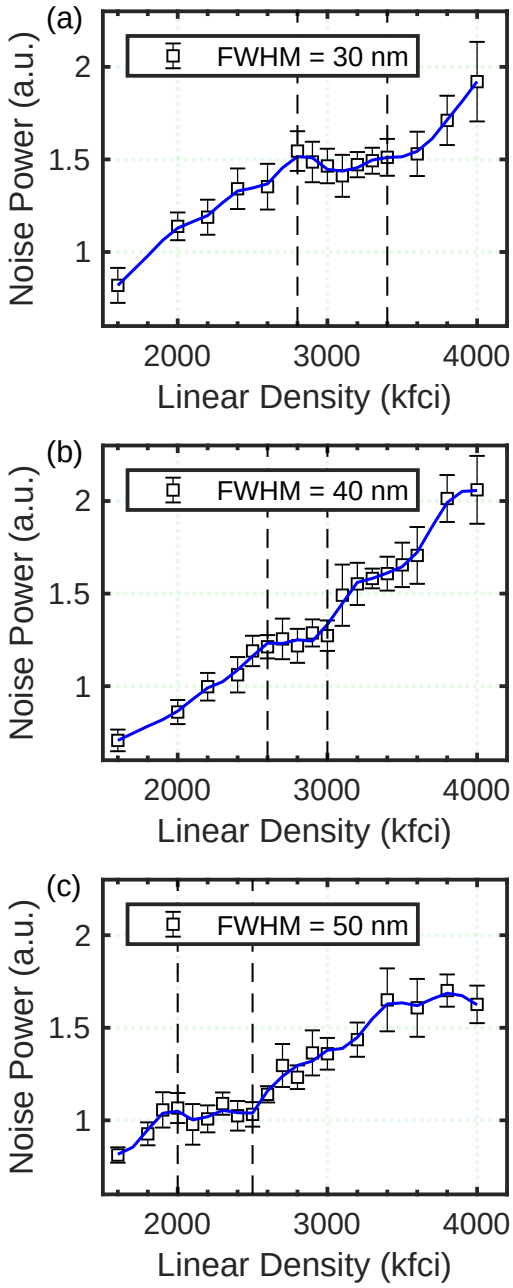


Figure 3.2: Integrated NP versus recording density for FWHM of (a) 30, (b) 40, and (c) 50 nm. $T_{peak}$ is 850 K for all cases. The dashed lines are given as guides to the eye. The blue solid lines represent the filtered results.

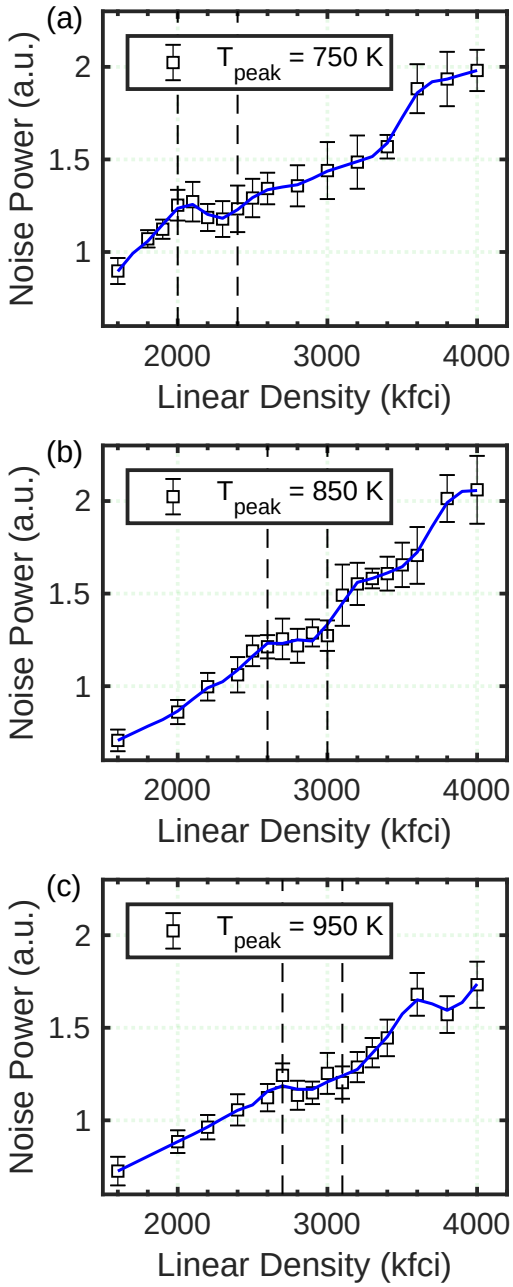


Figure 3.3: Integrated NP versus recording density for $T_{peak}$ of (a) 750, (b) 850, and (c) 950 K. The FWHMs are 40 nm. The blue solid lines represent the filtered results, and the dashed lines are given as guides to the eye.

large $\partial T/\partial x$ favors noise reduction at high density while a small $\partial T/\partial x$ favors noise reduction at low density.

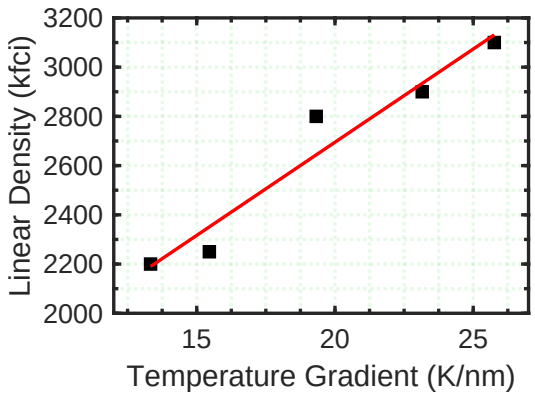


Figure 3.4: Linear density at plateau region center (estimated from Fig. 3.2 and Fig. 3.3) versus the temperature gradient.

### 3.3.5 Noise Plateau vs Read Head Width

Fig. 3.5 shows the NP for different read head widths (RWs). There are clear noise plateaus for RWs under 25 nm. The absence of a plateau for the 30 nm RW is because the recording pattern of HAMR has a transition curvature, and a wider read head is able to capture the curvature effect. Also, the side track noise on an ac-erased medium is detected by the wider head, thus the noise is increased and the plateau is obscured. The suggested RW should be about half of the FWHM [94] while the useful track width should be 70% of the FWHM [33].

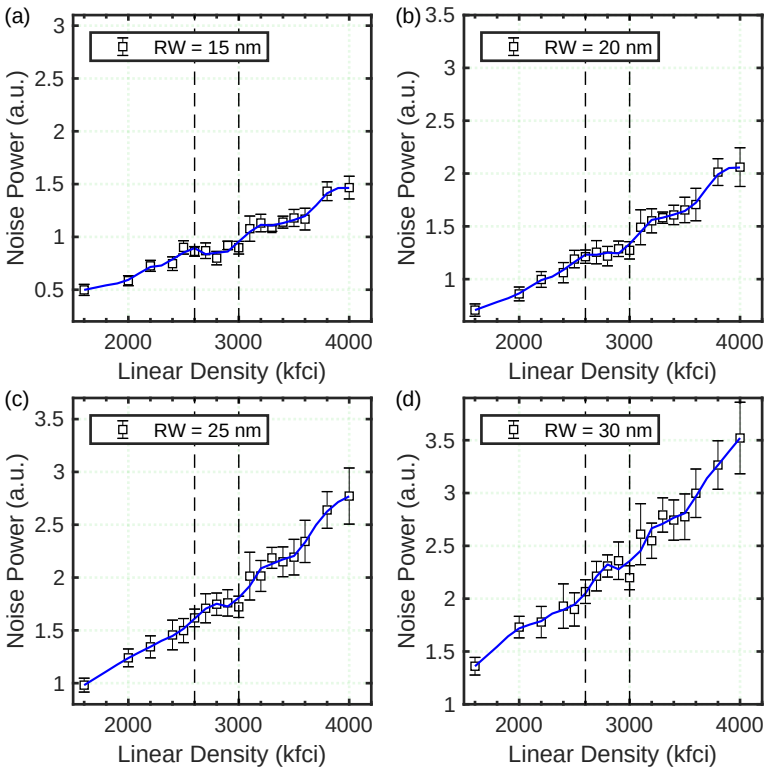


Figure 3.5: Integrated NP versus recording density for different RWs: (a) 15, (b) 20, (c) 25, and (d) 30 nm. The FWHM is 40 nm and the $T_{peak}$ is 850 K. The dashed lines are given as guides to the eye. The blue solid lines represent the filtered results.

## 3.4 Conclusion

In this chapter we showed that by adjusting the temperature profile, we can tune the NP behavior for different linear densities. For a single-tone signal, temperature profiles with higher gradients favor a noise plateau at high linear density while lower temperature gradients favor a noise plateau at low linear density. We found that a noise plateau is unaffected by the RW unless the head is wide enough to sample the sidetrack noise and the transition curvature.

# Chapter 4

# Rotated Read Head Design for High Density Heat-Assisted Shingled Magnetic Recording

Part of this chapter is based on the publication:
W.-H. Hsu and R. H. Victora, "Rotated read head design for high-density heat-assisted shingled magnetic recording," *Applied Physics Letters*, vol. 118, no. 7, p. 072406, 2021.

## 4.1 Introduction

In conventional HAMR, tracks are written in random order. At high recording density with closely spaced tracks, adjacent track erasure (ATE) occurs and a given track can experience two-sided erasure from writing to the neighboring tracks [96, 97]. Maximum user density (UD) is achieved by optimizing the track pitch (TP) so the ATE does not distort the data on the previously written track [33]. In heat-assisted shingled magnetic recording (HSMR), tracks are written adjacently in sequence; each newly written track overlaps the fixed side of the previously written track. In HSMR, only one-sided erasure occurs. Ideally, HSMR yields a higher UD than conventional HAMR with the same TP. However, two factors limit further improvement in HSMR's user density. First, only the track edge remains after ATE; the edge's recording quality is worse than that of the

track center. Also, the highly curved transitions in HSMR are asymmetric relative to the track center and are inevitable as long as the temperature profile generated by the near-field transducer remains elliptical in the media plane [32,98]. These asymmetrically curved transitions lead to signal loss in readback and limit the recording density.

In this chapter, we report on a study of HSMR through micromagnetic simulations. We found that by rotating the read head to compensate for asymmetrically curved transitions, we improved the UD more than 10% over that achievable with a non-rotated head. The relationship between the optimal rotation angle and the TP is explored. Finally, we show that the UD could go beyond 6.2 Tb/in$^2$ by combining the rotated read head with multiple sensor magnetic recording (MSMR).

## 4.2 Recording System Model

Magnetization dynamics were modeled with the Landau–Lifshitz–Gilbert (LLG) equation using 1.5 nm cubic renormalized cells (Sec. 2.2.1). The recording medium in this work was an ac-erased exchange-coupled composite (ECC) structure with a superparamagnetic write layer [33, 92]. The ECC media consisted of a 4.5 nm thick superparamagnetic write layer and a 9 nm thick storage layer. The recording grains were modeled as Voronoi cells with an average grain pitch of 4.8 nm, a standard deviation of 18%, and a 1 nm non-magnetic grain boundary. The storage layer was $L1_0$ FePt. A 2% Curie temperature variation among the grains was included. The Curie temperatures of the write layer and the storage layer were 900 K and 700 K, respectively. The magnetic properties of the renormalized cell were temperature dependent, and their values at 300 K can be found in Table 4.1.

| Parameters | Write Layer | Storage Layer |
|---|---|---|
| $M_s$ (emu/cm$^3$) | 550 | 942 |
| $K_u$ (erg/cm$^3$) | $0.7 \times 10^7$ | $4.4 \times 10^7$ |
| $A_{ex}$ (erg/cm) | $1.4 \times 10^{-6}$ | $1.1 \times 10^{-6}$ |
| $\alpha$ | 0.02 | 0.02 |

Table 4.1: Magnetic properties at 300 K for recording simulations.

The temperature profile was approximated as a 2-D Gaussian function in space with

a peak temperature of 850 K and a FWHM of 30 nm (Eq. (2.67)). The head velocity was 20 m/s and the applied writing field was 8 kOe with a canting angle of 22.5°. To simulate HSMR, three adjacent tracks were written on the media sequentially. The data sequence of the middle track was a fixed 31-bits pseudorandom binary sequence (PRBS) generated by the polynomial $x^5 + x^3 + 1$ while the sequence on the remaining two tracks were arbitrary 31-bit PRBSs. The minimum bit length was 6 nm. Sixty-four recording simulations were performed on different media realizations.

The noise-free magnetoresistive (MR) read head for readback had a shield-to-shield spacing (SSS) of 11 nm, a square-shaped 4 nm thick MR element, and a 6 nm magnetic fly height. The readback signals were obtained through cross-correlation of the read head sensitivity and the magnetization as prescribed by the reciprocity principle (Sec. 2.2.3).

The SNR, the BER, and the UD were calculated from the readback signals [33, 99]. For the BER calculation, 16 readback signals (496 bits) were used to train the equalizer function, and 48 readback signals (1488 bits) were used in a Viterbi detector to calculate the BER. The Shannon channel capacity $C$ was defined as $C = 1 + \mathrm{BER} \cdot \log_2(\mathrm{BER}) + (1 - \mathrm{BER}) \cdot \log_2(1 - \mathrm{BER})$, and the UD was calculated as $C/(\mathrm{BL} \cdot \mathrm{TP})$.

## 4.3 Results and Discussion

### 4.3.1 Comparision between HSMR and HAMR

Fig. 4.1(a) shows the average recording pattern of HSMR over 64 simulations and the relative configuration of the read head. Only the second track is visible after averaging. The read head was offset along the cross-track direction by $\Delta$ nm to the track center and was rotated counterclockwise by the angle $\theta$. Figs. 4.1(b)-(e) show the relations between track pitch and track width, SNR, BER, and UD; Fig. 4.1(f) displays SNR as a function of track width for varied reader widths (RW) from 12 nm to 18 nm. The figures include results for both HAMR and HMSR. Here we consider typical readback: the head was offset to the location that gave the maximum SNR without rotation ($\theta = 0°$). From the integral of the absolute value of the average magnetization along the down-track direction after writing, the track width (TW) can be defined as the full width at 50% of the maximum magnetization value. For a complete track, the TW was 24.3 nm for the heat profile and media design used here. The TW is narrower than

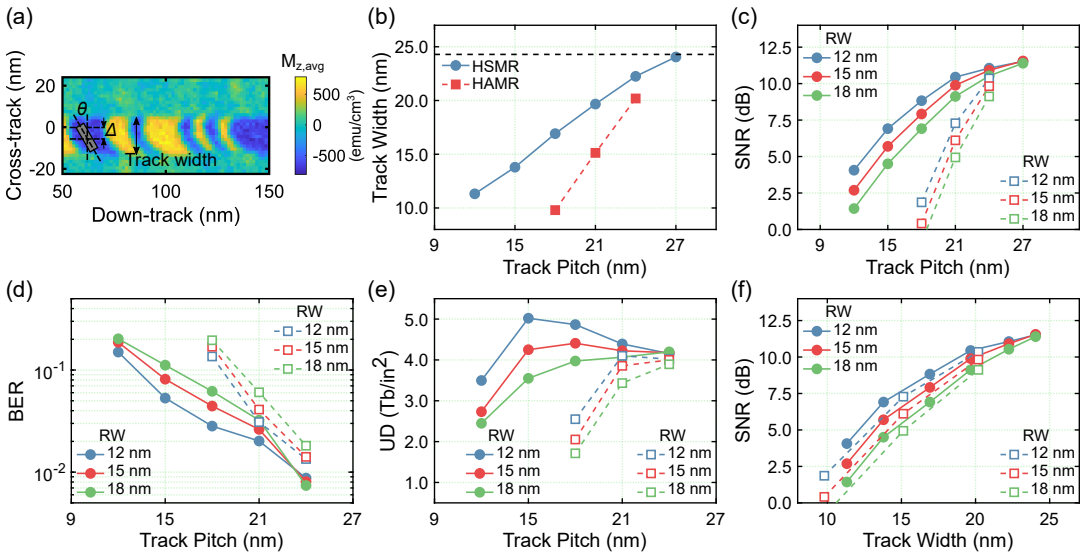


Figure 4.1: (a) Sample of the average recording pattern of HSMR over 64 simulations. The top track and the bottom track are imperceptible due to averaging. (b) Track width, (c) SNR, (d) BER, (e) UD as a function of track pitch, and (f) SNR as a function of track width for HSMR (solid curve) and HAMR (dashed curve) with various reader widths at $\theta = 0°$. The black dashed line in (b) indicates the track width without ATE.

the TP indicating the occurrence of the ATE. The HAMR TW decays faster than the HSMR TW due to the former's two-sided erasure. The resulting wider track width in HSMR yields better SNR, BER, and UD compared to HAMR.

The FWHMs of reader sensitivity in the cross-track direction for 12 nm, 15 nm, and 18 nm heads are 16.1 nm, 19.0 nm, and 21.9 nm, respectively. As track width decreases, the wider heads start to pick up undesired signals outside the track and show worse recording metrics than the narrowest head. It can be seen in Fig. 4.1(e) that the 18 nm head has no gain in UD for HSMR since the decrease of channel capacity $C$ offsets the gain from increasing TP. It shows that the UD can achieve 5 Tb/in$^2$ with a TP of 15 nm and a 12 nm head in HSMR. Beyond that point, ATE dominates, and UD drops.

One would expect HAMR to perform better than HSMR for a given track width since HSMR uses a curved track edge. Surprisingly, the SNRs in HSMR are comparable to the SNRs in HAMR (Fig. 4.1(f)), and they become slightly better when the TP is smaller. That may be because HAMR experiences two times erasure from adjacent track writes (ATWs) and the recorded quality of the center track is degraded. Moreover,

there will be more than one ATW in a real HAMR drive, whereas there is only one ATW in a real HSMR drive. The same argument can be applied to heat-assisted interlaced magnetic recording (HIMR) [100]; the underneath track may experience many ATWs resulting in bad recording quality.

### 4.3.2 Rotated Read Head

To achieve a higher UD, the asymmetrically curved transitions in HSMR need to be addressed. One approach is to rotate the read head to match the transition curvature. Fig. 4.2 shows the SNR, BER, and UD versus the rotation angle $\theta$ for a 12 nm head and an 18 nm head. At small $\theta$, all recording metrics are considerably improved, indicating that the rotated head starts to match the curve transition. If we further rotate the head, the SNR shows a monotonic increase while BER reaches its minimum and UD is at its maximum at a certain $\theta$, which is defined as the optimal $\theta$ ($\theta_{opt}$). The $\theta_{opt}$ are estimated from the quadratic polynomial fits of the UD curves. It can be seen that a large SNR does not necessarily imply a low BER or high UD. The larger effective SSS from the rotation improves the SNR because more low-frequency signals or long-bit signals can pass and strengthen the signal, but a larger SSS also leads to a resolution loss in high-frequency signals or short-bit signals, and thus BER grows and UD drops when $\theta$ exceeds $\theta_{opt}$. For a 12 nm head, $\theta_{opt}$ is larger when the TP becomes narrower which indicates the transitions are more asymmetric (Fig. 4.2(c)). For an 18 nm head, $\theta_{opt}$ values are smaller than those of a 12 nm head, and the difference in $\theta_{opt}$ between different TPs is smaller (Fig. 4.2(f)). This is because the 18 nm head tends to average out the transition and thus is less sensitive to the transition shape.

To understand how $\theta_{opt}$ changes with TP and RW, we focus on a single transition. The Fig. 4.3(a) inset shows the average of transitions from a single tone signal. The transition is fitted with quadratic polynomial as a function of cross-track position (red line). Depending on the position of the read head, the corresponding transition angle with respect to the track center can be extracted by taking the arctangent of the tangent to the transition. We compare the extracted angle with the $\theta_{opt}$ obtained from Fig. 4.2 and show them according to the read head position with respect to different TP in Fig. 4.3(a). The read head is closer to the track center with a wider TP, and vice versa. It is clear that the rotation of the head generally follows the shape of the transition. The

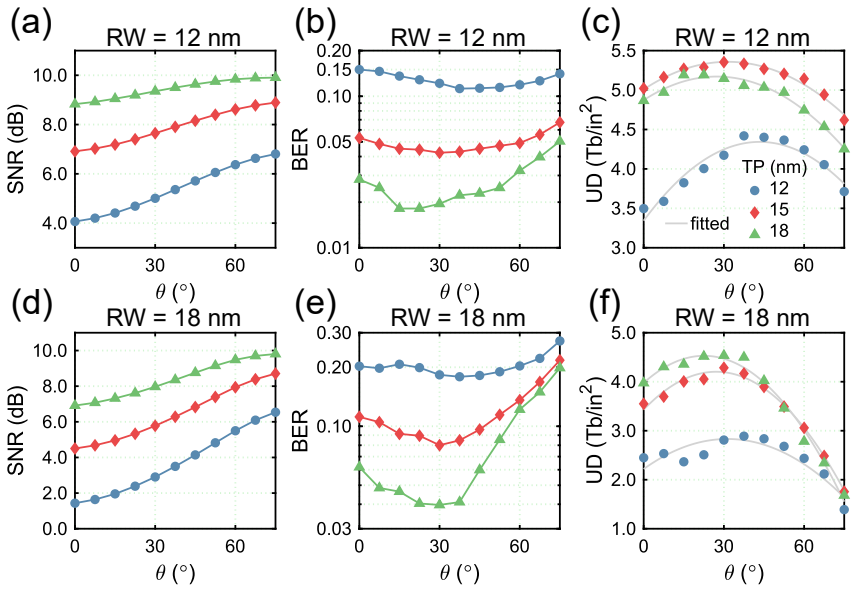


Figure 4.2: SNR, BER, and UD in HSMR as a function of $\theta$ at varied TPs with (a)-(c) a 12 nm head and (d)-(f) an 18 nm head where the read head is offset to the track center. The gray solid lines in (c) and (f) are quadratic polynomial fits.

difference between different read head width may originate from the finite width of the reader sensitivity along down-track and cross-track direction. A wide read head tends to rotate less, while a narrow head rotates more to capture the asymmetry. Fig. 4.3(b) shows the UDs of rotated and non-rotated heads. By simply rotating the head, the UD demonstrates a 5.9% enhancement; it reaches a 5.4 Tb/in$^2$ maximum from 5.1 Tb/in$^2$ at a 15 nm TP and a 30° $\theta_{opt}$ with a 12 nm head. For a 15 nm head, a 14% improvement can be seen (from 4.4 Tb/in$^2$ to 5.0 Tb/in$^2$). The increase is more pronounced when the head is wide (18 nm) and the TP is narrow (12 nm) where a more than 20% enhancement is achieved. Again, the maximum UD for an 18 nm head does not occur at a 15 nm TP due to the excess noise outside the track. The previously published work [101], which adopted a 90° rotated head design, utilized a side shield in the cross-track direction and aggressive oversampling to achieve its gain, while in this work, the improvement comes from matching the physical shape of the transition. This rotated head design is not compatible with HIMR since the transitions are symmetric as found in conventional HAMR, suggesting that HSMR has potential for higher UD over HIMR with proper

optimization. It should be noted that the rotated read head is used to address the asymmetrically curved transitions. For a PRBS with longer bit length, the number of transitions per unit length are fewer, so $\theta_{opt}$ may not follow the angle derived from transition shape.

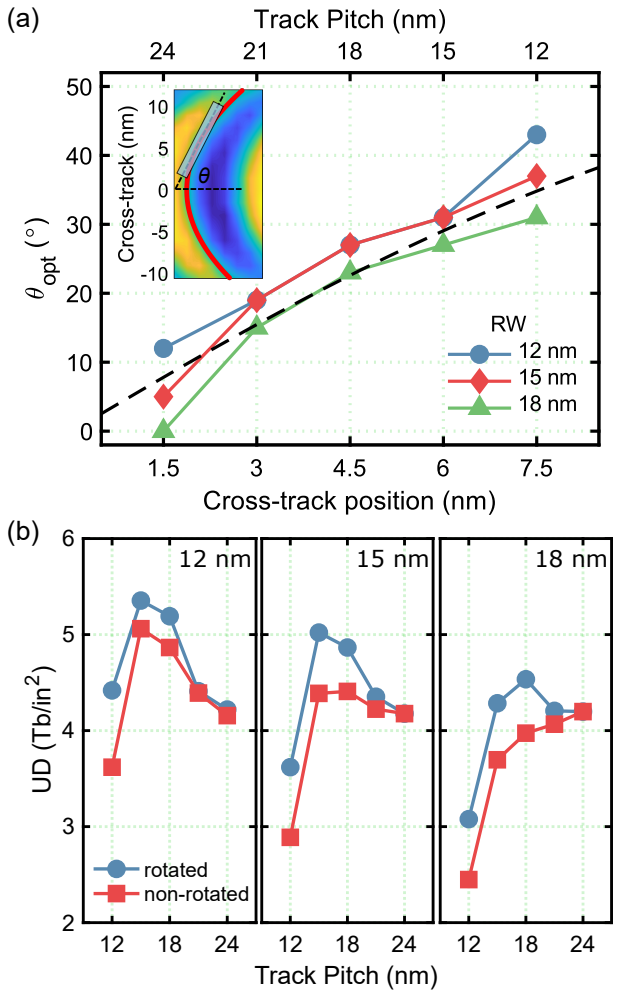


Figure 4.3: (a) $\theta_{opt}$ versus head position in the cross-track direction with varied RWs. The top axis is the corresponding track pitch. The dashed line is the $\theta$ derived from the shape of the transition. The inset shows the transition and the fitted line. (b) Comparison of UD between rotated head and non-rotated head for varied RWs.

### 4.3.3 Effect of Intergranular Eexchange

We note that in our configuration, unlike the previous work with its longer bit length [102], intergranular exchange coupling ($A_{ex,inter}$) does not improve the recording. By introducing up to 10% of intra-grain exchange ($A_{ex,intra}$) in the write layer, the maximum UD drops from 5.4 to 4.6 Tb/in$^2$ (Fig. 4.4). One reason for this is that the media used here is thick enough (13.5 nm) to reduce DC noise; another reason is that the minimum bit length used here is 6 nm which is very close to the grain pitch while $A_{ex,inter}$ favors a longer bit.

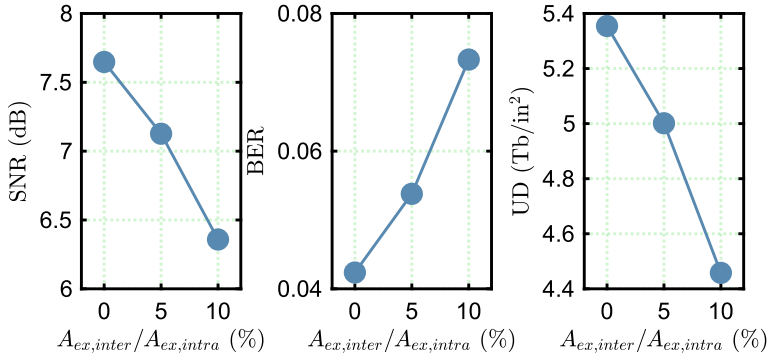


Figure 4.4: SNR, BER, and UD as a function of $A_{ex,inter}/A_{ex,intra}$ at TP = 15 nm and $\theta_{opt} = 30°$ for a 12 nm head.

### 4.3.4 Effect of Head Noise

We have considered only the media noise in this discussion so far. In fact, the head noise, which consists of the magnetization noise [103] and the Johnson noise [104], plays an important role in the real readback process. This is especially true of the magnetization noise which dominates when the volume of the MR element is small. We will consider head noise power-to-signal power ratio ($\text{NSR}_{\text{head}}$) from 2% to 6%, where the corresponding head SNR is from 17.0 dB to 12.2 dB, and that the head noise is included in the readback process as a Gaussian white noise. The SNR, BER, and the UD versus the $\text{NSR}_{\text{head}}$ for a 12 nm head at the optimal points are shown in (Fig. 4.5). The UD for the rotated head drops from 5.4 to 3.3 Tb/in$^2$, a 39% reduction when 6% head noise is included.

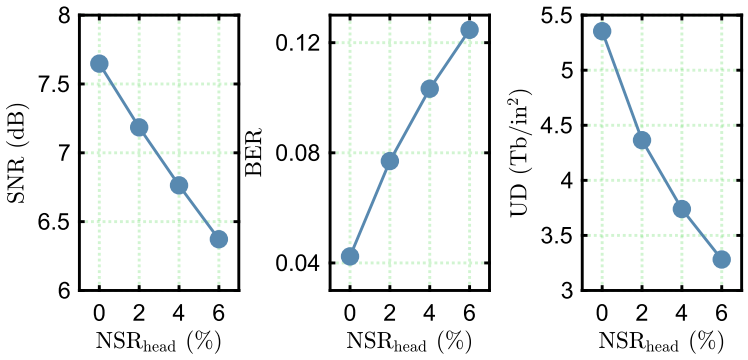


Figure 4.5: SNR, BER, and UD as a function of $\text{NSR}_{\text{head}}$ at TP = 15 nm for a 12 nm head.

### 4.3.5 MSMR

To further extend the feasibility of the rotated head, we combine it with MSMR which is proven to have UD gains [105]. We consider a two-reader MSMR, where the final signal ($S_{tot}$) is a linear combination of the signal from head 1 ($S_1$) and the signal from head 2 ($S_2$), $S_{tot} = 3 \times S_1 - 2 \times S_2$. From the fabrication point of view, the rotation angle for both heads is set to be the same. Fig. 4.6(a) and (b) show the UD as a function of the head 1 offset ($\Delta_1$) and the head 2 offset ($\Delta_2$) for 12 nm heads and 15 nm heads where the track center is at -6 nm and TP is 15 nm. We can see that the maximum UD is 5.9 Tb/in$^2$ for the 12 nm head and is 5.4 Tb/in$^2$ for the 15 nm head. Both occur at 37.5° $\theta$, a -9 nm $\Delta_1$, and a -7.5 nm $\Delta_2$. The $\theta_{opt}$ is different than the single head $\theta_{opt}$, which is 30°. The dual read heads show a 15.7% and 22.7% improvement over a single non-rotated 12 nm head and 15 nm head, respectively. Finally, if we allow both heads to rotate independently, 6.2 Tb/in$^2$ of UD is achieved for 12 nm heads when head 1 is rotated 7.5°, $\Delta_1$ is -1.5 nm, head 2 is rotated 37.5°, and $\Delta_2$ is 1.5 nm (Fig. 4.6(c)). Including additional heads and utilizing advanced signal processing techniques will likely push the UD well beyond 6.2 Tb/in$^2$. It is more than 30% greater than a previous projection for UD [33] and more than 50% greater than our prediction for non-shingled recording displayed in Fig. 4.1(e). It should be noted that the subtractive combination used here only works when the head noise is negligible, otherwise an additive combination is preferred.

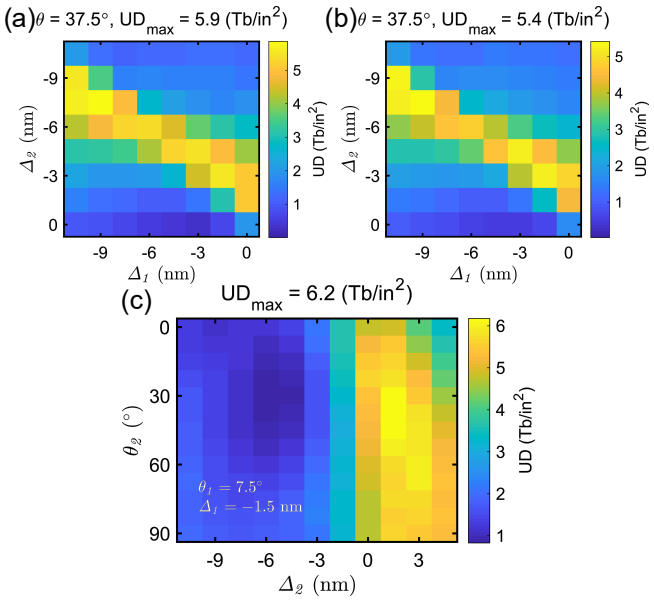


Figure 4.6: UD as function of the head 1 offset ($\Delta_1$) and the head 2 offset ($\Delta_2$) for (a) 12 nm heads and (b) 15 nm heads at $\theta = 37.5°$ and TP = 15 nm. (c) UD as function of the head 2 $\theta$ ($\theta_2$) and the head 2 offset ($\Delta_2$) for 12 nm heads where $\theta_1 = 7.5°$ and $\Delta_1$ = -1.5 nm.

## 4.4 Conclusion

In this chapter, we demonstrated that UD can be increased by more than 10% by simply rotating the read head. The gain in UD originates from the improved ability of the head to match the asymmetrically curved transitions through its optimal angle which roughly follows the shape of the transitions. By combining the rotated read head with MSMR and advanced signal processing techniques, the UD can potentially be extended beyond 6.2 Tb/in$^2$. The reduced ATW, and the compatibility with the rotated head make HSMR suitable for very high-density applications.

# Chapter 5

# Spin-Orbit Torque Switching in Low-Damping Magnetic Insulators

This chapter is based on the publication:
W.-H. Hsu and R. Victora, "Spin–orbit torque switching in low-damping magnetic insulators: A micrmomagnetic study," *IEEE Magnetics Letters*, vol. 11, pp. 1–5, 2020.

## 5.1 Introduction

MIs have unique magnetic properties, especially those in the family of rare-earth iron garnets (REIGs). For example, magnetic damping ($\alpha$) can be as low as $10^{-5}$ in yttrium iron garnet (YIG) ($Y_3Fe_5O_{12}$) [107] which implies a long spin-wave propagation length and a slow energy dissipation rate. The magnetic properties can be easily tuned by varying the composition of rare-earth elements. The realization of PMA in iron garnets makes them attractive for spintronic applications [108, 109].

Nevertheless, STT cannot be used to switch or excite a MI due to its insulating nature [110]. In contrast, in a HM/MI bilayer, electron current flowing in the HM can generate an out-of-plane spin current with in-plane spin polarization that provides SOT to switch the adjacent MI [49, 110]. Thus, SOT is an ideal way to manipulate the

magnetic moment of the MI in a HM/MI bilayer. SOT can excite spin waves in Pt/YIG [111] or induce switching in Pt/$BaFe_{12}O_{19}$ [112], Pt/$Tm_3Fe_5O_{12}$ (Pt/TmIG) [110], or Pt/$Y_3Fe_5O_{12}$ [113]. A fast SOT-driven domain wall motion in Pt/TmIG has also been reported [114–116]. Other than SOT-driven magnetization dynamics, a HM/MI bilayer itself also provides interesting physics. Chiral magnetic textures such as Néel domain walls and skyrmions have been observed in Pt/TmIG, suggesting that the system can have a sizable interfacial DMI [115, 117, 118]. Also, varied damping and DMI strengths with different combinations of HM and MI can yield unique magnetization dynamics [119]. Thus the HM/MI bilayer structure, especially HM/REIG along with SOT, shows great potential for spintronic applications.

In this chapter, we study SOT switching dynamics in a low-damping PMA MI through micromagnetic simulations. We show that low damping is not helpful for SOT switching; it introduces switching instability. The effect of interfacial DMI strength and FLT on switching is also discussed. It is shown that in a film with dimensions close to the monodomain limit, the switching instability caused by low damping can be reduced by introducing notches.

## 5.2 Methods

Following Sec. 2.1.1, the energy density for PMA materials can be expressed as a summation of uniaxial anisotropy energy, exchange energy, demagnetization energy, Zeeman energy, and interfacial DMI energy:

$$\frac{E}{V} = K_u[1-(\mathbf{m}\cdot\hat{u}_z)^2] + A_{ex}(\nabla\mathbf{m})^2 - \frac{1}{2}M_s\mathbf{m}\cdot\mathbf{H}_{dem} - M_s\mathbf{m}\cdot\mathbf{H}_{app} + D[(m_x\frac{\partial m_z}{\partial x} - m_z\frac{\partial m_x}{\partial x}) + (m_y\frac{\partial m_z}{\partial y} - m_z\frac{\partial m_y}{\partial y})], \quad (5.1)$$

where $K_u$ is the uniaxial anisotropy constant with the easy axis along the $\pm z$-direction, $\hat{u}_{i=x,y,z}$ is the unit vector, $A_{ex}$ is the exchange constant, $M_s$ is the saturation magnetization, $\mathbf{H}_{dem}$ is the demagnetizing field, $\mathbf{H}_{app}$ is the applied field, $D$ is the DMI parameter, and $\mathbf{m}$ is the normalized magnetization vector ($\mathbf{M}/M_s$). The effective field is the functional derivative of the free energy density with respect to $\mathbf{M}$ (Sec. 2.1.2). The boundary condition should be considered as well (Sec. 2.1.2).

The LLG equation with a SOT term (Eq. (2.50)) is rewritten as

$$\frac{\partial \mathbf{m}}{\partial t} = -\gamma \mathbf{m} \times \mathbf{H}_{eff} + \alpha \mathbf{m} \times \frac{d\mathbf{m}}{dt} - \gamma H_{SOT}[\mathbf{m} \times (\mathbf{m} \times \sigma) + r\mathbf{m} \times \sigma], \tag{5.2}$$

The $H_{SOT} = \theta_{SH} J_c / 2|e| M_s d$ is the magnitude of the effective field from SOT. $J_c$ is the applied current density and $d$ is the film thickness. The spin polarization ($\sigma$) is determined via the cross product of the unit vector of current and the interface normal $\sigma = -sgn(\theta_{SH}) \hat{J}_c \times \hat{u}_z$. The ratio of FLT ($= \mathbf{m} \times \sigma$) to DLT ($= \mathbf{m} \times (\mathbf{m} \times \sigma)$) is defined as $r$. The LLG equation was solved using a specially written graphics processing unit micromagnetic simulator in double precision. The fourth-order Runge–Kutta method with a fixed time step of 20 fs was adopted for numerical integration. The cell size is 10 nm × 10 nm × 9.6 nm for micrometer-sized samples and 5 nm × 5 nm × 9.6 nm for nanometer-sized samples.

Fig. 5.1 shows the HM/MI bilayer structure. The material properties of the MI were chosen to be similar to an experimental Pt/TmIG sample [114], which has $M_s = 100$ emu/cm$^3$, $K_u = 9.8 \times 10^4$ erg/cm$^3$, $A_{ex} = 3.6 \times 10^{-7}$ erg/cm, and an effective anisotropy field $H_{k,eff} \approx 2K_u/M_s - 4\pi M_s = 700$ Oe. The MI film thickness is 9.6 nm, and the $\theta_{SH}$ of the HM/MI stack is 0.03 [114]. One reason that MIs are attractive is their low $\alpha$, so $\alpha$ was chosen to be 0.001 which is smaller than most metallic systems. Interestingly, some recent studies of Pt/TmIG find a larger $\alpha$ on the order of 0.01 which is much greater than the $\alpha$ of YIG [109, 120, 121]. The $D$ value remains as an independent variable, since the origin of DMI in HM/MI is still unclear and reported values differ greatly [115, 118, 122].

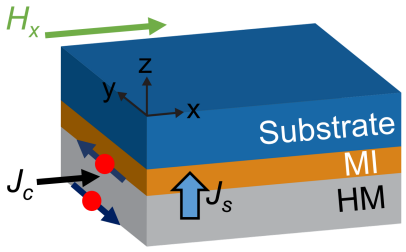


Figure 5.1: Schematic of the substrate/MI/HM structure. The electron current ($J_c$) and external field ($H_x$) are applied along $\hat{u}_x$. The spin current ($J_s$) is in the $z$-direction with a spin polarization along $\hat{u}_y$.

In this chapter, the most common SOT configuration has been adopted; the electron current is injected along the $x$-direction which gives $\sigma$ along $\hat{u}_y$, and an external field of 177 Oe is applied along $\hat{u}_x$ ($H_x$) [8]. The current pulse duration is 20 ns, followed by another 20 ns relaxation.

## 5.3 Results and Discussion

### 5.3.1 Switching in Micrometer-Sized Film

To date, most of the experimental demonstrations of SOT switching in MIs have used micrometer-sized samples. To have a comprehensive understanding of experimental results, we first study the switching in a MI film having the dimensions 1 µm × 1 µm × 9.6 nm assuming $D$ is 0.0 erg/cm$^2$ and the FLT is negligible. The average magnetization is initially along $-\hat{u}_z$ ($m_z \approx -1$). Fig. 5.2(a) shows the time evolution of $m_z$ as a function of $J_c$ with $\alpha = 0.001$. In this micrometer-sized film, switching occurs because of domain nucleation and domain wall propagation [123]. For a certain $J_c$ smaller than

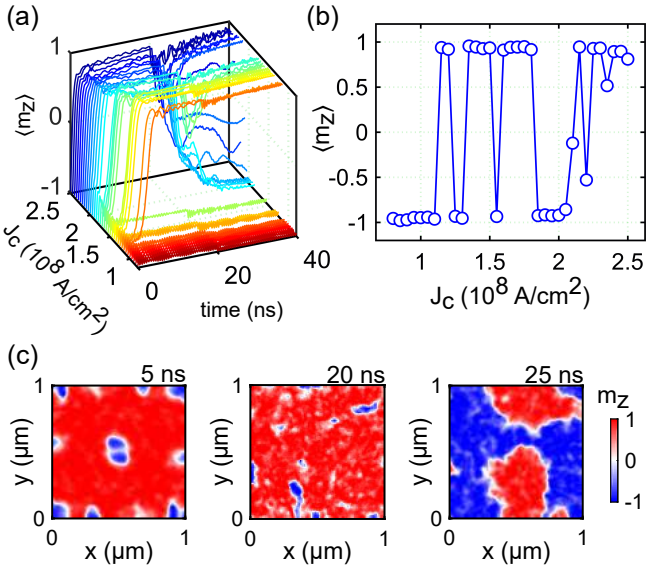


Figure 5.2: (a) $m_z$ as a function of time and applied current with a duration of 20 ns for 1 µm square. The applied in-plane field is 177 Oe with $D = 0.0$ erg/cm$^2$ and $\alpha = 0.001$. (b) $m_z$ at 40 ns (20 ns pulse + 20 ns relaxation) corresponding to (a). (c) Spatial $m_z$ profiles during switching at different times with $J_c = 1.85 \times 10^8$ A/cm$^2$.

$1.6 \times 10^8$ A/cm$^2$, an absence of domain nucleation leads to unsuccessful switching. At a high current density, many unsuccessful switches can be observed at 40 ns (Fig. 5.2(b)) even if successful domain nucleation followed by switching occurred in the first 20 ns (Fig. 5.2(a)). Since there are no temperature fluctuations considered, the randomness presented in the switching is not random; it is deterministic if $J_c$ is known. Fig. 5.2(c) shows an example of how $m_z$ evolves during switching at $J_c = 1.85 \times 10^8$ A/cm$^2$. A complex multidomain configuration at 20 ns is a consequence of the balance between micromagnetic energies and SOT [124], and this state indicates that the system is energetic. The energy provided by SOT cannot dissipate properly due to low $\alpha$, and eventually, a back switching occurs.

Unsuccessful switching can be viewed as a consequence of the precessional motion induced by $H_x$ in the macrospin approximation. SOT switching is a two-stage switching process; first, the SOT switches **m** to an intermediate state [50, 51], then switching completes through relaxation when the current is removed. If **m** is not placed in an energetically stable state by the SOT, the precession of **m** might lead to unsuccessful switching which is similar to field-induced precessional switching [60]. For a system with large $\alpha$, the precessional motion dies out faster, i.e. it has an increased energy dissipation rate, and its switching is more reliable compared to a system with a small $\alpha$. Nevertheless, $\alpha$ is fixed once the material and geometry are chosen. The other way to suppress precessional motion is to remove the in-plane field along with the current, and successful switching can be achieved. Using an even stronger in-plane field ($> 15\%$

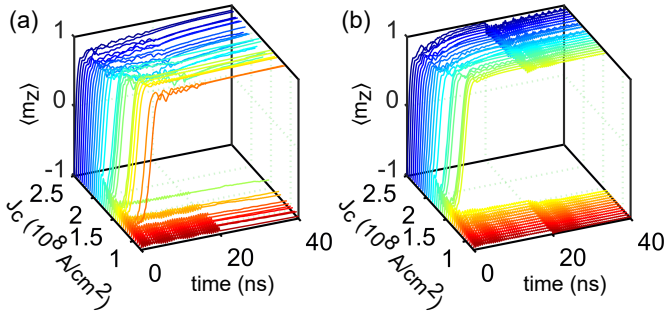


Figure 5.3: $m_z$ as a function of time and applied current with a duration of 20 ns for 1 µm square. The applied in-plane field is 177 Oe with $D = 0.0$ erg/cm$^2$. (a) $\alpha = 0.001$ and the applied field is removed at 20 ns. (b) $\alpha = 0.01$ and the applied field is always present.

of $H_k$) can also yield reliable switching [125].

For full micromagnetic system, the ideas from the macrospin approximation still apply: the low $\alpha$ cannot dissipate energy provided by the SOT in a reasonable period, and the presence of an in-plane field leads to uncertainty in switching. Here, two solutions are considered: removing the applied field along with the applied current while keeping $\alpha = 0.001$ (Fig. 5.3(a)) and keeping the applied field while increasing $\alpha$ to 0.01 (Fig. 5.3(b)). In Fig. 5.3(a), back switching is eliminated because the precessional motion along the applied field is prohibited after both current and field are removed at 20 ns. For Fig. 5.3(b), which has $\alpha$ of 0.01, back switching is eliminated because the extra energy provided by SOT can be dissipated properly with larger damping.

Apparently, unlike STT switching, low $\alpha$ is not an advantage in SOT switching. STT directly acts against the damping torque at the start of the switching, whereas SOT behaves like a moving magnetic field along $\mathbf{m} \times \sigma$, which neither opposes nor assists the damping torque [126]. The critical current of SOT switching is independent of $\alpha$ if no FLT exists [50, 52]. Low-damping induced unsuccessful SOT switching has been briefly reported in the literature [52–54] but is sometimes overlooked because almost all metallic systems have high damping.

### 5.3.2 Effect of DMI

Another solution to improve switching depends on control of the DMI. Fig. 5.4(b) shows $m_z$ at 40 ns with various DMI strengths. The sign of $D$ determines the domain wall chirality and the nucleation site; here only positive D is considered [127]. For small $D$ values ($D = 0.002$ erg/cm$^2$ in Ref. [115]), the switching is not reliable. As $D$ increases, nonswitching is still present, but back switching is eliminated. For large $D$ values, ($D \approx 0.05$ erg/cm$^2$ in Ref. [118]), Néel domain walls are favored. Once Néel domain walls are formed, switching can be achieved through domain wall propagation without back switching (Fig. 5.4(a)) [128].

### 5.3.3 Effect of FLT

Ref. [129] showed that the SOT in a HM/MI bilayer can have a non-negligible FLT component, and this can play an important role in SOT switching [130]. Switching

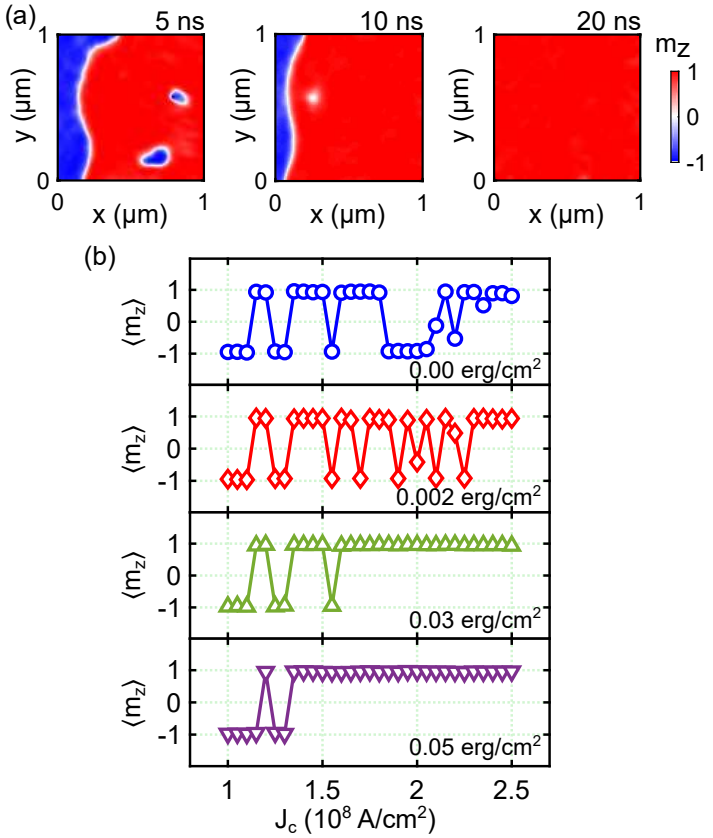


Figure 5.4: (a) $m_z$ profile during switching at different times with $J_c = 1.85 \times 10^8$ A/cm$^2$ and $D = 0.05$ erg/cm$^2$. (b) $m_z$ measured at 40 ns (20 ns pulse + 20 ns relaxation) with various $D$ values.

under FLT is shown in Fig. 5.5 with $r = \pm 0.2$ for $D = 0.00$ erg/cm$^2$ and $D = 0.05$ erg/cm$^2$. It can be seen that positive $r$ (FLT/DLT $> 0$) improves switching whereas negative $r$ does not. For a negative $r$, FLT and DLT drive $\mathbf{m}$ in opposite directions, which may lead to complicated magnetization states and eventually to unsuccessful switching. A recent study also suggests that negative $r$ might lead to unsuccessful switching due to the domain wall reflecting when the wall hits the edge [131].

### 5.3.4 Switching in Nanometer-Sized Film

So far, the simulation results have mainly focused on micrometer-sized samples as typical for studies of the physics and material properties. For practical applications, a lateral

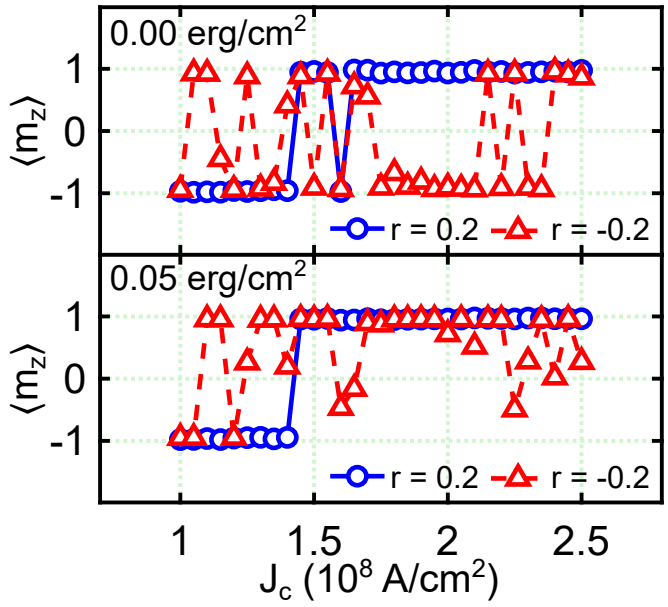


Figure 5.5: $m_z$ measured at 40 ns (20 ns pulse + 20 ns relaxation) for $r = \pm 0.2$ with $D = 0.00$ erg/cm$^2$ and $D = 0.05$ erg/cm$^2$.

size on the order of 100 nm is preferred. Here, a film with dimensions 100 nm $\times$ 100 nm $\times$ 9.6 nm is considered. Unsuccessful switching at this length scale is mainly due to the oscillatory motion of domains (Fig. 5.6(a)). Inspired by domain wall devices that utilize notches to pin the domain wall, four artificial square notches with a dimension of 20 nm $\times$ 20 nm were introduced (Fig. 5.6(b)). In general, these notches lower the domain wall length, i.e. wall energy. Switching is improved by preventing the energetic domain from oscillating through the whole film. However, unlike the micrometer-sized sample, DMI does not increase reliable switching in nanometer-sized samples, whether they are notched or not (Fig. 5.6(c)). A possible explanation is that DMI promotes a nonuniform state and lowers the domain wall energy making it is easier to form domains and impede switching compared to the micrometer-sized sample which is dominated by demagnetizing energy. It should be noted that patterning at the 20 nm length scale has not yet been demonstrated in garnets.

To fully utilize a low-damping MI in a SOT system, an in-plane configuration with its easy axis parallel to $\sigma$ is preferred. In this case, the switching dynamics will be similar

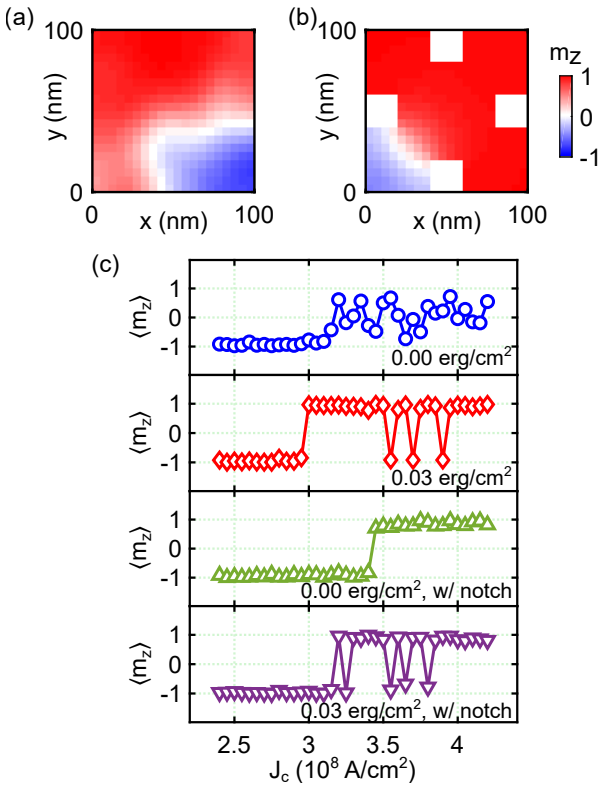


Figure 5.6: $m_z$ profile during switching at 20 ns with $J_c = 3.7 \times 10^8$ A/cm$^2$. (a) Without notch. (b) With 20 nm $\times$ 20 nm notches on each side. $D = 0.0$ erg/cm$^2$ for both cases. (c) $m_z$ measured at 40 ns (20 ns pulse + 20 ns relaxation) with $D = 0.00$ erg/cm$^2$, $D = 0.03$ erg/cm$^2$, $D = 0.00$ erg/cm$^2$ with notch, and $D = 0.03$ erg/cm$^2$ with notch.

to in-plane STT. By coupling the MI with a material of high anisotropy, e.g., $L1_0$ FePt, low switching energy can be achieved while maintaining enough thermal stability for technologically important nanometer-sized devices which will be discussed in the next chapter (Ch. 6).

## 5.4 Conclusion

In summary, we investigated SOT switching in low-damping PMA MIs through micromagnetic simulations. The low-damping nature of the material may impede reliable switching. We showed that there are several ways to improve switching, such as:

(i) Remove the applied in-plane field along with the applied current;

(ii) Introduce DMI or positive FLT (relative to DLT);

(iii) Introduce a notch design to pin the magnetic domain in a nanometer-sized device, minimizing DMI so as not to impede successful switching in these devices.

Although only low-damping MIs are studied in this chapter, its central argument also holds for metallic systems with similar properties.

# Chapter 6

# Ultra-low Write Energy Composite Free Layer SOT MRAM

This chapter is based on the publication:
W.-H. Hsu, R. Bell, and R. H. Victora, "Ultra-low write energy composite free layer spin–orbit torque MRAM," *IEEE Transactions on Magnetics*, vol. 54, no. 11, pp. 1–5, 2018.

## 6.1 Introduction

From the previous chapter, we know that SOT switching in low-damping PMA material may be unsuccessful due to a low energy dissipation rate. An i-MTJ with spin polarization collinear with its easy axis can supposedly fully utilize the low damping and SOT (Sec. 1.2.4) since the critical current for this case is proportional to $\alpha$ (Eq. (1.1)). A MI such as YIG achieves very low Gilbert damping ($\alpha_{YIG} \sim 10^{-4}$) [107, 133, 134], and the SOT mechanism enables selection of YIG as the free layer in SOT systems. However, YIG is not suitable for memory applications due to its low thermal stability.

Generally, a thermal stability $\Delta$ ($\Delta = K_u V/k_B T$) of 60 achieves data retention on the order of 10 years at room temperature. $K_u$ is the magnetocrystalline anisotropy, $V$

is the volume of nanomagnet, $k_B$ is the Boltzmann's constant, and $T$ is the temperature. FM materials with high $K_u$ are preferred for high-density memory applications owing to their nanoscale device size. Specifically, $L1_0$ ordered phase crystals such as FePt or FePd are suitable due to their high $K_u$ ($\sim 10^7$ erg/cm$^3$) [135] and moderate damping [87]. The other benefit of choosing a high $K_u$ material is that not only the requisite device diameter but also the cross-sectional area of the HM layer can be reduced which reduces write current and write energy. However, the critical current is large in $L1_0$ ordered phase crystal-based devices because it is proportional to their anisotropy field (Eq. (1.1)).

The benefits from both low-damping MIs and high $K_u$ FM materials can be achieved at the same time through an exchange-coupled composite structure [27]. Fig. 6.1(a) shows our proposed in-plane SOT-MRAM structure which is similar to the three-terminal SOT structure in [15]. The length and the width of HM with a thickness ($t_{HM}$) are set to be equal to the diameter ($D$) of a circular MTJ. The single-free layer in a normal MTJ is replaced by an efficient exchange-coupled composite free layer with an $L1_0$ FePt or $L1_0$ FePd hard layer (HL) and a YIG soft layer (SL) . The top electrode is for readout. Though the PMA of a FePt-based MTJ [136] has been shown to have a TMR of 100%, a comparably high TMR for in-plane magnetic anisotropy of $L1_0$ FePt has not yet been measured [137].

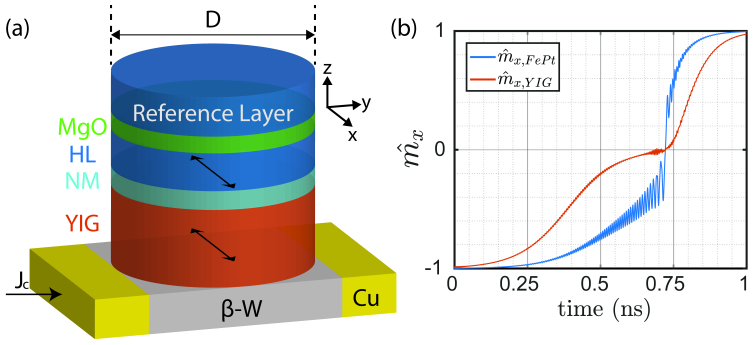


Figure 6.1: (a) Schematic of the proposed in-plane SOT-MRAM. Only the MTJ part is shown. (b) Magnetization reversal of the composite structure. For this case, $t_{FePt} = 1$ nm, $t_{YIG} = 8$ nm, $J_{ex} = 5$ erg/cm$^2$, and $J_c = 6 \times 10^7$ A/cm$^2$.

In our structure, the easily switched SL assists the switching of HL via FM coupling modulated by a NM layer such as Pd. The injected spin current density ($J_s$) due to the

SHE can be expressed as $J_s = \theta_{SH}[1-\text{sech}(t_{HM}/\lambda_{sf})]J_c$ [138], where $\theta_{SH}$ is the spin Hall angle, $\lambda_{sf}$ is the spin-flip scattering length in the HM, $t_{HM}$ is the HM thickness, and $J_c$ is the applied charge current density. The spin polarization of the spin current is along $\hat{\sigma} = \pm\hat{J}_c(\hat{y}) \times \hat{z} = \pm\hat{x}$. This spin current generates a torque to reverse the magnetization of the easily switched SL. Once the HL passes the equator $m_x = 0$ through exchange coupling, the assistance from the anisotropy field makes it switch faster than the SL (Fig. 6.1(b)). Note that the easy axis of the proposed cell is in-plane and along $\pm\hat{x}$; alternatively, an external field could be used to break the symmetry in a design with PMA.

## 6.2 Methods

### 6.2.1 Heavy Metal Selection

The write energy ($E_w$) of the cell can be written as

$$E_w = t_{pulse} R_{HM} I_c^2 = t_{pulse} \frac{\rho_{HM}}{t_{HM}} (t_{HM} D J_c)^2, \tag{6.1}$$

where $t_{pulse}$, $R_{HM}$, $\rho_{HM}$, and $I_c$ are the current pulse duration, HM electrical resistance, HM resistivity, and charge current, respectively. The generalized optimal HM thickness ($t_{HM,opt}$) is obtained via the first and second derivative tests of Eq. (6.1): $t_{HM,opt} = 2.45\lambda_{sf}$. The YIG contribution to $\Delta$ is negligible because the anisotropy energy of YIG is relatively small ($\sim 10^5$ erg/cm$^3$) [139] compared with $K_{u,HL}$ ($\sim 10^7$ erg/cm$^3$), thus we ignore the contribution of the YIG anisotropy field for further calculations. For a desired $\Delta$ of 60, we write

$$60 k_B T \approx K_{u,HL} V_{HL} = K_{u,HL} \pi D^2 t_{HL}/4, \tag{6.2}$$

where $t_{HL}$ is the thickness of HL. Replacing $t_{HM}$ with $t_{HM,opt}$ and $J_c$ with $J_s$, Eq. (6.1) becomes

$$E_w = \frac{856.24 t_{pulse} k_B T}{\pi K_{u,HL} t_{HL}} \frac{\rho_{HM} \lambda_{sf}}{\theta_{SH}^2} J_s^2. \tag{6.3}$$

From Eq. (6.3), we propose a figure of merit (FOM) for HM layer selection:

$$\text{FOM} = \frac{\rho_{HM}\lambda_{sf}}{\theta_{SH}^2}. \tag{6.4}$$

The best HMs have the smallest FOM. A large $\theta_{SH}$ results in smaller charge current density needed, a small $\rho$ reduces bias voltage, and a small $\lambda_{sf}$ reduces optimal thickness, so the proposed FOM will guide HM selection.

### 6.2.2 Micromagnetic Simulations

The SOT-MRAM was solved numerically via a fourth-order Runge–Kutta method of the set of coupled LLG equations with the SOT term in a macrospin approximation:

$$\frac{d\mathbf{m}_i}{dt} = -\gamma \mathbf{m}_i \times \mathbf{H}_{eff,i} + \alpha_i \mathbf{m}_i \times \frac{d\mathbf{m}_i}{dt} + \tau_{SOT,i}, \tag{6.5}$$

where $\mathbf{m}$ is the unit magnetization vector, $\mathbf{H}_{eff,i}$ is the total effective field, $\alpha$ is the Gilbert damping constant, and $i$ stands for HL or YIG. The numerical integration time step was 5 fs. $\tau_{SOT,i}$ is the torque generated by the SHE and only exists in the YIG layer. $\mathbf{H}_{eff,i}$ consists of anisotropy field $\mathbf{H}_{k,i} = (2K_{u,i}/M_{s,i})m_{x,i}\hat{x}$, demagnetizing field $\mathbf{H}_{d,i} = -\mathcal{N}_{d,i}M_{s,i}\mathbf{m}_i$, and exchange field $\mathbf{H}_{ex,i} = J_{ex,i}/(M_{s,i}t_i)\mathbf{m}_j$, where $J_{ex}$ is the coupling strength constant, $M_s$ is the saturation magnetization, and $t$ is the thickness of the layer. The demagnetizing tensor ($\mathcal{N}_d$) was approximated as an ellipsoid [140]. The effective field imposed on the YIG is approximately equal to the exchange field imposed on it by HL since its anisotropy and $M_s$ are relatively small. The magnetostatic interaction between the two layers was neglected for simplicity. $\tau_{SOT}$ is formulated as

$$\tau_{SOT} = \frac{\gamma\hbar}{2|e|}\frac{J_s}{M_{s,YIG}t_{YIG}}[\mathbf{m}_{YIG} \times (\sigma \times \mathbf{m}_{YIG}) + r(\sigma \times \mathbf{m}_{YIG})], \tag{6.6}$$

where $r$ is the ratio of the FLT to the DLT. We examined $r$ from 0 to 2, and our final results show that this FLT is acting as a small bias field on the YIG and does not affect our central results.

The initial angle [141] for the FL was taken as $\theta_0 = \sqrt{1/\Delta} \approx 0.13\ rad$. Similarly, the critical angle for magnetization switching is $\theta_c = \pi - \theta_0$ and is defined as the angular distance the magnetization must travel to constitute a thermally stable reversal. The

HL must reach $\theta_c$ within 1 ns for ultra-fast information storage, thus $t_{pulse}$ was set to 1 ns in this chapter. The spin Hall angle was 0.3 which is achievable with $\beta$-W thin films [142] that have $\rho_{HM} = 200$ μΩ-cm and $\lambda_{sf} = 1.4$ nm. Therefore, the FOM of $\beta$-W is 31.1 kΩ-nm$^2$. From the relationship between $\mathbf{H}_{eff}$ and $\tau_{SOT}$, we can see that an increase in $t_{HL}$ yields a roughly proportional increase in $J_c$. The optimization of the SOT cell is completely a function of the HL, NM (determines $J_{ex}$), and YIG thicknesses. These relationships are illustrated in the next section. The material parameters used for numerical simulations are listed in Table 6.1.

| Parameters | $L1_0$ FePt | $L1_0$ FePd | YIG |
|---|---|---|---|
| $M_s$ (emu/cm$^3$) | 1000 | 1000 | 130 |
| $K_u$ (erg/cm$^3$) | $4.6 \times 10^7$ | $1.3 \times 10^7$ | — |
| $A_{ex}$ (erg/cm) | $1.0 \times 10^{-6}$ | $1.0 \times 10^{-6}$ | $3.7 \times 10^{-7}$ |
| $\alpha$ | 0.02 | 0.009 | $1.0 \times 10^{-4}$ |

Table 6.1: Typical material properties at room temperature.

## 6.3 Results and Discussion

### 6.3.1 Device Optimization

We varied the HL thickness from 0.25 to 2.0 nm while maintaining the volume $V_{HL} = 60k_BT/K_{u,HL}$ at room temperature (300 K) for $\Delta = 60$. Fig. 6.2 shows the contour plot of normalized magnetization of 1 nm thick HL along $\hat{x}$ under varied applied current densities as a function of $J_{ex}$ and $t_{YIG}$. Figs. 6.2(a)-(c) are for FePt and Figs. 6.2(d)-(f) are for FePd. HL switching is a combination of precessional switching and damping switching because the HL exchange field keeps changing direction. Since FePt $\alpha$ is about twice that of FePd, the switching mechanism is more like damping switching for FePt (i.e., $\mathbf{m}_{FePt}$ follows $\mathbf{H}_{ex,FePt}$ more closely). Usually a small $\alpha$ indicates slower switching speed in response to the field; that is why the contour plot of $m_x$ for FePd broadens.

An optimal design should approximately follow fixed ratios of $(M_{s,YIG}t_{YIG})/(M_{s,HL}t_{HL})$ and $J_{ex}/(2K_{u,HL}t_{HL})$. The first term is the ratio of the magnetic moment between two

layers, and the second term represents the ratio of $|\mathbf{H}_{ex}|$ and $|\mathbf{H}_k|$ in the HL. The minimum $E_w$ can then be calculated from Eq. (6.3) and is proportional to $t_{HL}$ ($\propto D^{-2}$ under a fixed $V_{HL}$). This relationship was verified in our numerical simulations and is shown in Fig. 6.3 as a function of device diameter. Although a $E_w$ as low as 18 aJ ($\approx 4300 k_B T$) can be achieved for a 1 ns current pulse, a more realistic geometry such as a 15.6 nm disk of FePd (1 nm)/YIG (2.14 nm) composite structure requires 60 aJ. $E_w$ of single layer FePt and FePd cells were also calculated and included in Fig. 6.3 for comparison with FLT neglected. Composite structures show a 6.5 to 20 times improvement in write energy depending on their materials which suggests that a composite free layer structure is a better choice for low-energy memory.

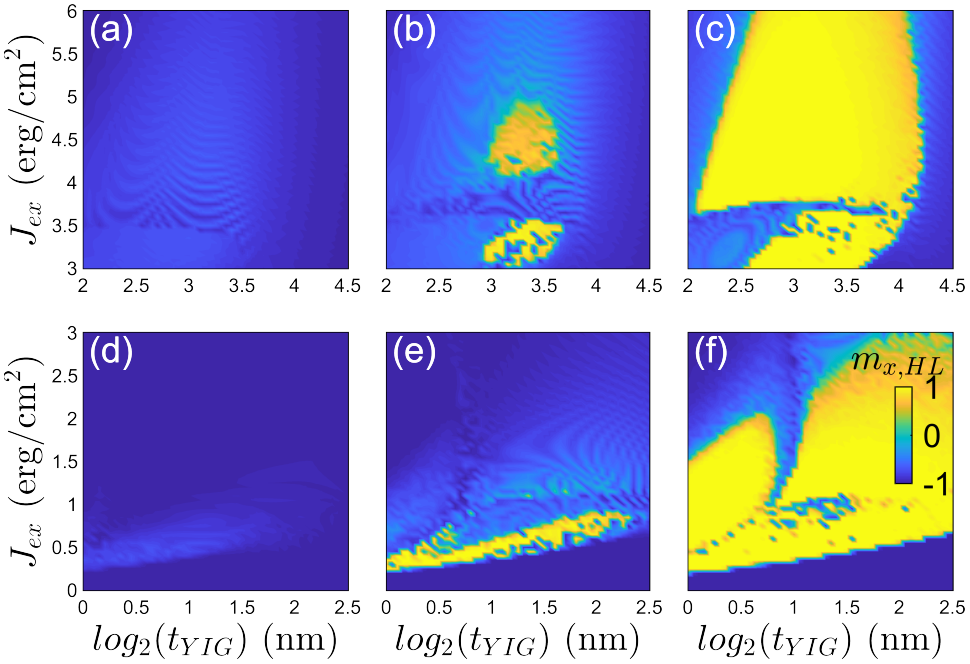


Figure 6.2: Normalized HL magnetization along $\hat{x}$ after a 1 ns current pulse. $J_c$ is (a) $4 \times 10^7$ A/cm$^2$, (b) $5 \times 10^7$ A/cm$^2$, and (c) $6 \times 10^7$ A/cm$^2$ for 1 nm FePt ($D = 8.3$ nm), and (d) $1 \times 10^7$ A/cm$^2$, (e) $2 \times 10^7$ A/cm$^2$, and (f) $3 \times 10^7$ A/cm$^2$ for 1 nm FePd ($D = 15.6$ nm). The initial state was $m_x \approx -1$.

### 6.3.2 Comparison with State-of-the-art RAM

STT-MRAM [11,12] can achieve a sub-picojoule $Ew$ per bit; for an electric field induced device [13,14], $E_w$ is about tens of femtojoules per bit. Ref. [15] proposed a SOT-MRAM that can achieve 100 aJ. However, these devices all have large diameters (>40 nm) or insufficient $\Delta$ (<60). Low anisotropy CoFeB as the free layer necessitates large diameters which is not favorable to high-density applications. Also, bulk PMA here is more reliable than the interfacial PMA in CoFeB. Therefore, the employment of high $K_u$ materials is advantageous in SOT-MRAM. A state-of-the-art DDR4 DRAM has a standard cell area of $6F^2$, where F denotes the process, currently 10 nm. This DRAM operates at around 1 V with a minimum acceptable cell capacitance of 10 fF [143]. Therefore, the write energy of a DRAM cell is about $10^4$ aJ, approximately 360 times the $E_w$ of a FePd/YIG composite structure having the same diameter. We only compare the energy consumption of a single cell in this chapter; nevertheless, the power consumption from peripheral circuitry and the refresh energy for DRAM (the dominant energy term as

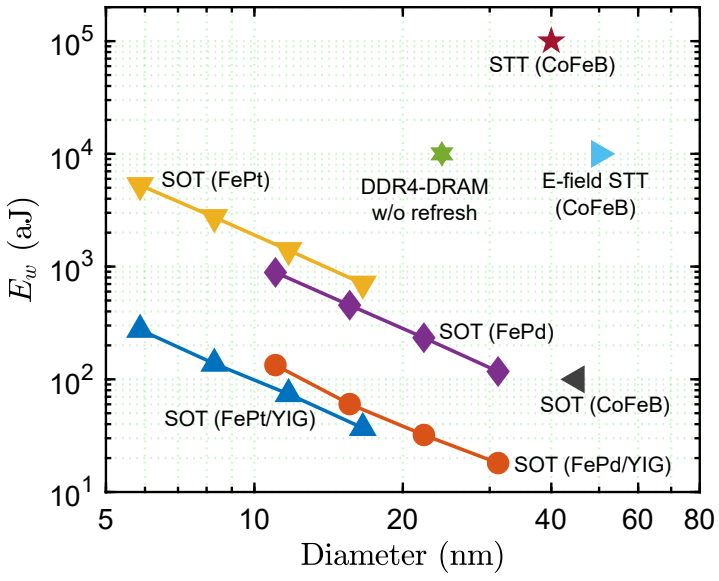


Figure 6.3: Write energy of the proposed SOT MRAM versus device size. Results from DRAM and other CoFeB based MRAMs are also included: STT-MRAM [11,12], E-field STT-MRAM [13,14], and SOT-MRAM [15].

DRAM capacity increases and leakage currents consequently increase [144]) needs to be considered when benchmarking our proposed device with existing technology. Although dimensions are provided for FePt, FePd, and YIG devices, the central argument still holds for other materials with similar properties, e.g. Heusler alloy $Co_2FeAl$ also has a low $\alpha$ and a low $H_k$ but relatively high $M_s$ [145, 146].

### 6.3.3 Bit Error Rate

The results shown earlier do not consider the effect of thermal fluctuations. At a finite temperature, thermal fluctuations tend to randomize the magnetic moment and lead to non-deterministic switching in MRAM devices. Also, for large-angle switching, magnon-magnon scattering dominates [147], so full micromagnetic simulations are needed. We calculated and compared the BER of a FePd (1 nm)/YIG (2.14 nm) cell from macrospin ($J_{ex}$ = 0.5 erg/cm$^2$) results and micromagnetic results. For micromagnetic simulations (Sec. 2.1), the system was discretized into 6 × 6 × 3 cells with a grid size of 2.6 nm × 2.6 nm × 1 nm, which is within the exchange length. We ignored the NM layer for simplicity in our micromagnetic simulation. The interlayer exchange in the

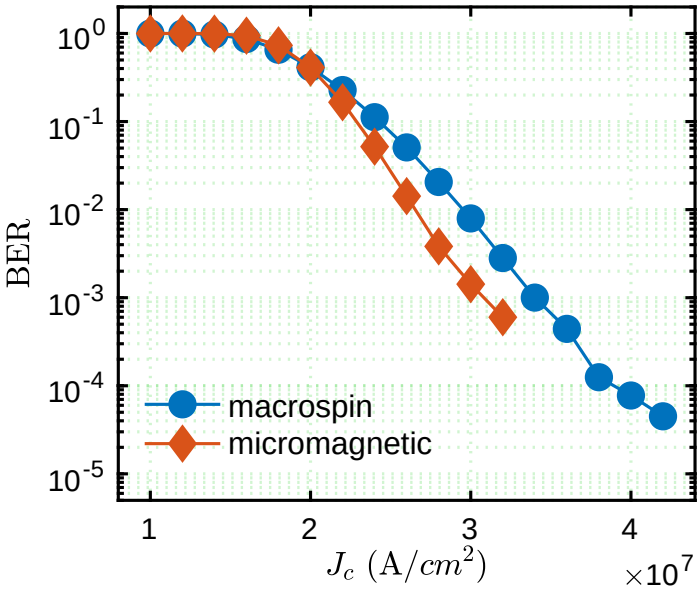


Figure 6.4: BER versus $J_c$ for optimized FePd (1 nm)/YIG (2.14 nm) composite MRAM.

micromagnetic simulations was taken to be $2.3 \times 10^{-8}$ erg/cm which is the optimal value for this geometry. We also assumed that the SOT only affects the bottom layer since there is no net electron flow into the YIG layer. Thermal fluctuations can be modeled as an effective field in the LLG equation (Sec. 2.1.3). Switching is considered to be complete when the average of $m_x$ is larger than 0.9 ($\langle m_x \rangle > 0.9$) at 300 K. The results are shown in Fig. 6.4. The micromagnetic simulations show switching at a slightly lower current than the macrospin simulations as expected owing to the possibility of incoherent switching or domain wall motion. The tail of the two curves loses accuracy due to an insufficient number of trials to evaluate low error rates. Micromagnetic simulations are computationally expensive; techniques like rare event enhancement [148] might help simulate a BER of $10^{-9}$ which is acceptable in commercial applications [141].

## 6.4 Conclusion

In this chapter, we showed, by utilizing the exchange coupling between a thermally stable HL of $L1_0$ FePt or $L1_0$ FePd and an ultra-low-damping MI such as YIG, that a write energy of 18 aJ ($\approx 4300 k_B T$) can be achieved. A prescription for HM layer thickness that depends on the spin diffusion length is proposed. Furthermore, a FOM for HM layer selection is suggested to minimize write energy. The proposed SOT-MRAM achieves a 500 times improvement in write energy over a state-of-the-art DDR4 DRAM cell. If refresh energy is considered, this improvement can be much greater.

# Chapter 7

# Summary

This dissertation reports the results of micromagnetic simulations for emerging magnetic storage devices, particularly HAMR and SOT-MRAM, driven by the demand for low-cost data storage and high performance computer memory. The first part of this dissertation responds to the low-cost demands on new storage technologies. One way to increase storage density is to reduce the media noise. I showed that media noise behavior in HAMR depends heavily on the temperature profile. A heat spot with a large thermal gradient is favored for recording at high density because of its lower transition noise. It was found that there exists a region where the total noise does not grow with recording density due to the competition between remanence noise and transition noise. This noise plateau region shows a linear relationship with the thermal gradient. Another way to increase recording density is through engineering and optimization of the recording system. In HSMR, more than a 10% improvement in UD can be achieved by rotating the read head to match the curved transitions on the track edge. The rotation angle is found by matching the shape of the transitions. HSMR combined with two-dimensional magnetic recording is expected to push UD beyond 6.2 terabits per square inch.

In the second part of the dissertation, I focused on SOT switching for low-damping MIs and related devices. I found that low damping impeded successful SOT switching in PMA MIs due to their slow energy dissipation rate. This argument applies to other PMA materials with low damping as well. Aside from increasing the damping, removing the applied field along with the applied current, or introducing interfacial DMI, a positive FLT or notches (in a nanometer-sized device) can help achieve successful switching.

To follow up on the fact that SOT switching is more efficient for in-plane MIs, an in-plane exchange-coupled composite free layer SOT-MRAM is proposed. The free layer consists of a high $K_u$ $L1_0$ alloy that is ferromagnetically coupled to a low damping MI. A criterion for HM selection is provided to minimize the write energy. By leveraging exchange coupling, a write energy of 18 attojoules per bit is achieved in a 31 nm diameter MRAM. This write energy is only 72 times more than the theoretical limit of $60k_BT$.

In summary, I hope the results presented in this dissertation provide insight for the decision of future magnetic storage devices.

# Bibliography


[1] Wikipedia, "Hard disk drive — Wikipedia, the free encyclopedia," 2021. [Online].

[2] A. Moser, K. Takano, D. T. Margulies, M. Albrecht, Y. Sonobe, Y. Ikeda, S. Sun, and E. E. Fullerton, "Magnetic recording: advancing into the future," *Journal of Physics D: Applied Physics*, vol. 35, no. 19, p. R157, 2002.

[3] D. Weller, G. Parker, O. Mosendz, A. Lyberatos, D. Mitin, N. Y. Safonova, and M. Albrecht, "FePt heat assisted magnetic recording media," *Journal of Vacuum Science & Technology B, Nanotechnology and Microelectronics: Materials, Processing, Measurement, and Phenomena*, vol. 34, no. 6, p. 060801, 2016.

[4] Wikipedia, "Giant magnetoresistance — Wikipedia, the free encyclopedia," 2021. [Online].

[5] S. Ikeda, H. Sato, H. Honjo, E. Enobio, S. Ishikawa, M. Yamanouchi, S. Fukami, S. Kanai, F. Matsukura, T. Endoh, *et al.*, "Perpendicular-anisotropy CoFeB-MgO based magnetic tunnel junctions scaling down to 1X nm," in *2014 IEEE International Electron Devices Meeting*, pp. 33–2, IEEE, 2014.

[6] A. Brataas, A. D. Kent, and H. Ohno, "Current-induced torques in magnetic materials," *Nature Materials*, vol. 11, no. 5, pp. 372–381, 2012.

[7] X. Fong, Y. Kim, K. Yogendra, D. Fan, A. Sengupta, A. Raghunathan, and K. Roy, "Spin-transfer torque devices for logic and memory: Prospects and perspectives," *IEEE Transactions on Computer-Aided Design of Integrated Circuits and Systems*, vol. 35, no. 1, pp. 1–22, 2015.

[8] S. Fukami, T. Anekawa, C. Zhang, and H. Ohno, "A spin–orbit torque switching scheme with collinear magnetic easy axis and current configuration," *Nature Nanotechnology*, vol. 11, no. 7, pp. 621–625, 2016.

[9] A. Fert, V. Cros, and J. Sampaio, "Skyrmions on the track," *Nature Nanotechnology*, vol. 8, no. 3, pp. 152–156, 2013.

[10] R. H. Victora and P.-W. Huang, "Simulation of heat-assisted magnetic recording using renormalized media cells," *IEEE Transactions on Magnetics*, vol. 49, no. 2, pp. 751–757, 2013.

[11] H. Zhao, A. Lyle, Y. Zhang, P. Amiri, G. Rowlands, Z. Zeng, J. Katine, H. Jiang, K. Galatsis, K. Wang, *et al.*, "Low writing energy and sub nanosecond spin torque transfer switching of in-plane magnetic tunnel junction for spin torque transfer random access memory," *Journal of Applied Physics*, vol. 109, no. 7, p. 07C720, 2011.

[12] S. Ikeda, K. Miura, H. Yamamoto, K. Mizunuma, H. Gan, M. Endo, S. Kanai, J. Hayakawa, F. Matsukura, and H. Ohno, "A perpendicular-anisotropy CoFeB–MgO magnetic tunnel junction," *Nature Materials*, vol. 9, no. 9, pp. 721–724, 2010.

[13] S. Kanai, Y. Nakatani, M. Yamanouchi, S. Ikeda, F. Matsukura, and H. Ohno, "In-plane magnetic field dependence of electric field-induced magnetization switching," *Applied Physics Letters*, vol. 103, no. 7, p. 072408, 2013.

[14] C. Grezes, F. Ebrahimi, J. Alzate, X. Cai, J. Katine, J. Langer, B. Ocker, P. Khalili Amiri, and K. Wang, "Ultra-low switching energy and scaling in electric-field-controlled nanoscale magnetic tunnel junctions with high resistance-area product," *Applied Physics Letters*, vol. 108, no. 1, p. 012403, 2016.

[15] S. Manipatruni, D. E. Nikonov, and I. A. Young, "Energy-delay performance of giant spin Hall effect switching for dense magnetic memory," *Applied Physics Express*, vol. 7, no. 10, p. 103001, 2014.

[16] O. Smith, *Some possible forms of phonograph.* Electrical World, 1888.

[17] C. Walter, "Kryder's law," *SciAm*, vol. 293, no. 2, pp. 32–33, 2005.

[18] D. R.-J. G.-J. Rydning, "The digitization of the world from edge to core," *Framingham: International Data Corporation*, 2018.

[19] M. H. Kryder, E. C. Gage, T. W. McDaniel, W. A. Challener, R. E. Rottmayer, G. Ju, Y.-T. Hsia, and M. F. Erden, "Heat assisted magnetic recording," *Proceedings of the IEEE*, vol. 96, no. 11, pp. 1810–1835, 2008.

[20] M. N. Baibich, J. M. Broto, A. Fert, F. N. Van Dau, F. Petroff, P. Etienne, G. Creuzet, A. Friederich, and J. Chazelas, "Giant magnetoresistance of (001) Fe/(001) Cr magnetic superlattices," *Physical Review Letters*, vol. 61, no. 21, p. 2472, 1988.

[21] G. Binasch, P. Grünberg, F. Saurenbach, and W. Zinn, "Enhanced magnetoresistance in layered magnetic structures with antiferromagnetic interlayer exchange," *Physical Review B*, vol. 39, no. 7, p. 4828, 1989.

[22] L. Berger, "Emission of spin waves by a magnetic multilayer traversed by a current," *Physical Review B*, vol. 54, no. 13, p. 9353, 1996.

[23] J. C. Slonczewski *et al.*, "Current-driven excitation of magnetic multilayers," *Journal of Magnetism and Magnetic Materials*, vol. 159, no. 1, p. L1, 1996.

[24] H. N. Bertram, *Theory of magnetic recording*. Cambridge University Press, 1994.

[25] M. L. Plumer, J. Van Ek, and D. Weller, *The physics of ultra-high-density magnetic recording*, vol. 41. Springer Science & Business Media, 2012.

[26] B. Vasic and E. M. Kurtas, *Coding and signal processing for magnetic recording systems*. CRC press, 2004.

[27] R. H. Victora and X. Shen, "Composite media for perpendicular magnetic recording," *IEEE Transactions on Magnetics*, vol. 41, no. 2, pp. 537–542, 2005.

[28] R. H. Victora and X. Shen, "Exchange coupled composite media for perpendicular magnetic recording," *IEEE Transactions on Magnetics*, vol. 41, no. 10, pp. 2828–2833, 2005.

[29] J.-G. Zhu, X. Zhu, and Y. Tang, "Microwave assisted magnetic recording," *IEEE Transactions on Magnetics*, vol. 44, no. 1, pp. 125–131, 2007.

[30] J.-G. J. Zhu and H. Li, "Correcting transition curvature in heat-assisted magnetic recording," *IEEE Transactions on Magnetics*, vol. 53, no. 2, pp. 1–7, 2016.

[31] A. Ghoreyshi and R. H. Victora, "Localization noise in deep subwavelength plasmonic devices," *Physical Review B*, vol. 97, no. 20, p. 205430, 2018.

[32] R. H. Victora and A. Ghoreyshi, "Optical analysis of HAMR media," *IEEE Transactions on Magnetics*, vol. 55, no. 3, pp. 1–8, 2018.

[33] Z. Liu, Y. Jiao, and R. Victora, "Composite media for high density heat assisted magnetic recording," *Applied Physics Letters*, vol. 108, no. 23, p. 232402, 2016.

[34] N. F. Mott, "The electrical conductivity of transition metals," *Proceedings of the Royal Society of London. Series A-Mathematical and Physical Sciences*, vol. 153, no. 880, pp. 699–717, 1936.

[35] M. Julliere, "Tunneling between ferromagnetic films," *Physics Letters A*, vol. 54, no. 3, pp. 225–226, 1975.

[36] T. Miyazaki and N. Tezuka, "Giant magnetic tunneling effect in $Fe/Al_2O_3/Fe$ junction," *Journal of Magnetism and Magnetic Materials*, vol. 139, no. 3, pp. L231–L234, 1995.

[37] J. S. Moodera, L. R. Kinder, T. M. Wong, and R. Meservey, "Large magnetoresistance at room temperature in ferromagnetic thin film tunnel junctions," *Physical Review Letters*, vol. 74, no. 16, p. 3273, 1995.

[38] W. Butler, X.-G. Zhang, T. Schulthess, and J. MacLaren, "Spin-dependent tunneling conductance of Fe|MgO|Fe sandwiches," *Physical Review B*, vol. 63, no. 5, p. 054416, 2001.

[39] J. Mathon and A. Umerski, "Theory of tunneling magnetoresistance of an epitaxial Fe/MgO/Fe (001) junction," *Physical Review B*, vol. 63, no. 22, p. 220403, 2001.

[40] M. Bowen, V. Cros, F. Petroff, A. Fert, C. Martınez Boubeta, J. L. Costa-Krämer, J. V. Anguita, A. Cebollada, F. Briones, J. De Teresa, *et al.*, "Large magnetoresistance in Fe/MgO/FeCo (001) epitaxial tunnel junctions on GaAs (001)," *Applied Physics Letters*, vol. 79, no. 11, pp. 1655–1657, 2001.

[41] S. Yuasa, T. Nagahama, A. Fukushima, Y. Suzuki, and K. Ando, "Giant room-temperature magnetoresistance in single-crystal Fe/MgO/Fe magnetic tunnel junctions," *Nature Materials*, vol. 3, no. 12, pp. 868–871, 2004.

[42] S. S. Parkin, C. Kaiser, A. Panchula, P. M. Rice, B. Hughes, M. Samant, and S.-H. Yang, "Giant tunnelling magnetoresistance at room temperature with MgO (100) tunnel barriers," *Nature Materials*, vol. 3, no. 12, pp. 862–867, 2004.

[43] D. D. Djayaprawira, K. Tsunekawa, M. Nagai, H. Maehara, S. Yamagata, N. Watanabe, S. Yuasa, Y. Suzuki, and K. Ando, "230% room-temperature magnetoresistance in CoFeB/MgO/CoFeB magnetic tunnel junctions," *Applied Physics Letters*, vol. 86, no. 9, p. 092502, 2005.

[44] S. Ikeda, J. Hayakawa, Y. Ashizawa, Y. Lee, K. Miura, H. Hasegawa, M. Tsunoda, F. Matsukura, and H. Ohno, "Tunnel magnetoresistance of 604% at 300 K by suppression of Ta diffusion in CoFeB/MgO/CoFeB pseudo-spin-valves annealed at high temperature," *Applied Physics Letters*, vol. 93, no. 8, p. 082508, 2008.

[45] B. Engel, J. Akerman, B. Butcher, R. Dave, M. DeHerrera, M. Durlam, G. Grynkewich, J. Janesky, S. Pietambaram, N. Rizzo, *et al.*, "A 4-Mb toggle MRAM based on a novel bit and switching method," *IEEE Transactions on Magnetics*, vol. 41, no. 1, pp. 132–136, 2005.

[46] J. Z. Sun, "Spin-current interaction with a monodomain magnetic body: A model study," *Physical Review B*, vol. 62, no. 1, p. 570, 2000.

[47] I. M. Miron, G. Gaudin, S. Auffret, B. Rodmacq, A. Schuhl, S. Pizzini, J. Vogel, and P. Gambardella, "Current-driven spin torque induced by the Rashba effect in a ferromagnetic metal layer," *Nature Materials*, vol. 9, no. 3, pp. 230–234, 2010.

[48] L. Liu, C.-F. Pai, Y. Li, H. Tseng, D. Ralph, and R. Buhrman, "Spin-torque switching with the giant spin Hall effect of tantalum," *Science*, vol. 336, no. 6081, pp. 555–558, 2012.

[49] L. Liu, O. Lee, T. Gudmundsen, D. Ralph, and R. Buhrman, "Current-induced switching of perpendicularly magnetized magnetic layers using spin torque from the spin Hall effect," *Physical Review Letters*, vol. 109, no. 9, p. 096602, 2012.

[50] T. Taniguchi, S. Mitani, and M. Hayashi, "Critical current destabilizing perpendicular magnetization by the spin Hall effect," *Physical Review B*, vol. 92, no. 2, p. 024428, 2015.

[51] S. Yan and Y. B. Bazaliy, "Phase diagram and optimal switching induced by spin Hall effect in a perpendicular magnetic layer," *Physical Review B*, vol. 91, no. 21, p. 214424, 2015.

[52] K.-S. Lee, S.-W. Lee, B.-C. Min, and K.-J. Lee, "Threshold current for switching of a perpendicular magnetic layer induced by spin Hall effect," *Applied Physics Letters*, vol. 102, no. 11, p. 112410, 2013.

[53] N. Mikuszeit, O. Boulle, I. M. Miron, K. Garello, P. Gambardella, G. Gaudin, and L. D. Buda-Prejbeanu, "Spin-orbit torque driven chiral magnetization reversal in ultrathin nanostructures," *Physical Review B*, vol. 92, no. 14, p. 144424, 2015.

[54] B. Chen, S. Ter Lim, and M. Tran, "Magnetization switching of a thin ferromagnetic layer by spin-orbit torques," *IEEE Magnetics Letters*, vol. 7, pp. 1–5, 2016.

[55] W. F. Brown, *Micromagnetics*. New York: Interscience Publishers, 1963.

[56] A. E. LaBonte, "Two-dimensional Bloch-type domain walls in ferromagnetic films," *Journal of Applied Physics*, vol. 40, no. 6, pp. 2450–2458, 1969.

[57] R. Victora, "Quantitative theory for hysteretic phenomena in CoNi magnetic thin films," *Physical Review Letters*, vol. 58, no. 17, p. 1788, 1987.

[58] J. E. Miltat and M. J. Donahue, "Numerical micromagnetics: Finite difference methods," *Handbook of Magnetism and Advanced Magnetic Materials*, 2007.

[59] C. Abert, "Micromagnetics and spintronics: models and numerical methods," *The European Physical Journal B*, vol. 92, no. 6, p. 120, 2019.

[60] I. D. Mayergoyz, G. Bertotti, and C. Serpico, *Nonlinear magnetization dynamics in nanosystems*. Elsevier, 2009.

[61] H. Yang, M. Chshiev, B. Dieny, J. Lee, A. Manchon, and K. Shin, "First-principles investigation of the very large perpendicular magnetic anisotropy at Fe|MgO and Co|MgO interfaces," *Physical Review B*, vol. 84, no. 5, p. 054401, 2011.

[62] I. Dzyaloshinsky, "A thermodynamic theory of "weak" ferromagnetism of antiferromagnetics," *Journal of Physics and Chemistry of Solids*, vol. 4, no. 4, pp. 241–255, 1958.

[63] T. Moriya, "Anisotropic superexchange interaction and weak ferromagnetism," *Physical Review*, vol. 120, no. 1, p. 91, 1960.

[64] A. Fert and P. M. Levy, "Role of anisotropic exchange interactions in determining the properties of spin-glasses," *Physical Review Letters*, vol. 44, no. 23, p. 1538, 1980.

[65] A. Bogdanov, U. Rößler, M. Wolf, and K.-H. Müller, "Magnetic structures and reorientation transitions in noncentrosymmetric uniaxial antiferromagnets," *Physical Review B*, vol. 66, no. 21, p. 214410, 2002.

[66] D. Cortés-Ortuño and P. Landeros, "Influence of the Dzyaloshinskii–Moriya interaction on the spin-wave spectra of thin films," *Journal of Physics: Condensed Matter*, vol. 25, no. 15, p. 156001, 2013.

[67] L. Landau and E. Lifshitz, "On the theory of the dispersion of magnetic permeability in ferromagnetic bodies," in *Perspectives in Theoretical Physics*, pp. 51–65, Elsevier, 1992.

[68] T. L. Gilbert, "A phenomenological theory of damping in ferromagnetic materials," *IEEE Transactions on Magnetics*, vol. 40, no. 6, pp. 3443–3449, 2004.

[69] R. Kikuchi, "On the minimum of magnetization reversal time," *Journal of Applied Physics*, vol. 27, no. 11, pp. 1352–1357, 1956.

[70] W. F. Brown Jr, "Thermal fluctuations of a single-domain particle," *Physical Review*, vol. 130, no. 5, p. 1677, 1963.

[71] A. J. Newell, W. Williams, and D. J. Dunlop, "A generalization of the demagnetizing tensor for nonuniform magnetization," *Journal of Geophysical Research: Solid Earth*, vol. 98, no. B6, pp. 9551–9555, 1993.

[72] M. Mansuripur and R. Giles, "Demagnetizing field computation for dynamic simulation of the magnetization reversal process," *IEEE Transactions on Magnetics*, vol. 24, no. 6, pp. 2326–2328, 1988.

[73] S. W. Yuan and H. N. Bertram, "Fast adaptive algorithms for micromagnetics," *IEEE Transactions on Magnetics*, vol. 28, no. 5, pp. 2031–2036, 1992.

[74] X. Feng and P. Visscher, "Coarse-graining Landau–Lifshitz damping," *Journal of Applied Physics*, vol. 89, no. 11, pp. 6988–6990, 2001.

[75] Y. Jiao, Z. Liu, and R. H. Victora, "Renormalized anisotropic exchange for representing heat assisted magnetic recording media," *Journal of Applied Physics*, vol. 117, no. 17, p. 17E317, 2015.

[76] N. Natekar, W.-H. Hsu, and R. Victora, "Calculated dependence of FePt damping on external field magnitude and direction," *AIP Advances*, vol. 7, no. 5, p. 056004, 2017.

[77] R. Ahmed and R. H. Victora, "A fully electric field driven scalable magnetoelectric switching element," *Applied Physics Letters*, vol. 112, no. 18, p. 182401, 2018.

[78] Y. Jiao, *Simulation of Heat Assisted Magnetic Recording System.* PhD thesis, University of Minnesota, Twin Cities, 2018.

[79] R. Victora, W. Peng, J. Xue, and J. Judy, "Superlattice magnetic recording media: experiment and simulation," *Journal of Magnetism and Magnetic Materials*, vol. 235, no. 1-3, pp. 305–311, 2001.

[80] Y. Dong and R. Victora, "Micromagnetic study of medium noise plateau," *IEEE Transactions on Magnetics*, vol. 45, no. 10, pp. 3714–3717, 2009.

[81] W.-H. Hsu and R. Victora, "Micromagnetic study of media noise plateau in heat-assisted magnetic recording," *IEEE Transactions on Magnetics*, vol. 55, no. 2, pp. 1–4, 2018.

[82] J.-G. Zhu and H. Li, "Understanding signal and noise in heat assisted magnetic recording," *IEEE Transactions on Magnetics*, vol. 49, no. 2, pp. 765–772, 2013.

[83] R. H. Victora, S. Wang, P.-W. Huang, and A. Ghoreyshi, "Noise mitigation in granular and bit-patterned media for HAMR," *IEEE Transactions on Magnetics*, vol. 51, no. 4, pp. 1–7, 2015.

[84] C. Vogler, C. Abert, F. Bruckner, D. Suess, and D. Praetorius, "Basic noise mechanisms of heat-assisted-magnetic recording," *Journal of Applied Physics*, vol. 120, no. 15, p. 153901, 2016.

[85] H. Bertram and M. Schabes, "A model for noise power nonlinearities in perpendicular magnetic recording," *IEEE Transactions on Magnetics*, vol. 45, no. 8, pp. 3100–3106, 2009.

[86] J. Zhang, T. C. Arnoldussen, and S. Duan, "Cluster cutting: A better understanding of media noise in perpendicular magnetic recording," *IEEE Transactions on Magnetics*, vol. 52, no. 11, pp. 1–5, 2016.

[87] T. Qu and R. H. Victora, "Effect of substitutional defects on Kambersky damping in $L1_0$ magnetic materials," *Applied Physics Letters*, vol. 106, no. 7, p. 072404, 2015.

[88] B. F. Valcu and M. Alex, "Nonlinear transition shift in heat assisted magnetic recording," *IEEE Transactions on Magnetics*, vol. 49, no. 7, pp. 3648–3651, 2013.

[89] X. Wang, K. Gao, H. Zhou, A. Itagi, M. Seigler, and E. Gage, "HAMR recording limitations and extendibility," *IEEE Transactions on Magnetics*, vol. 49, no. 2, pp. 686–692, 2013.

[90] J. Hohlfeld, P. Czoschke, P. Asselin, and M. Benakli, "Improving our understanding of measured jitter (in HAMR)," *IEEE Transactions on Magnetics*, vol. 55, no. 3, pp. 1–11, 2018.

[91] Y. Jiao, J. Hohlfield, and R. H. Victora, "Understanding transition and remanence noise in HAMR," *IEEE Transactions on Magnetics*, vol. 54, no. 11, pp. 1–5, 2018.

[92] Z. Liu and R. H. Victora, "Composite structure with superparamagnetic writing layer for heat-assisted magnetic recording," *IEEE Transactions on Magnetics*, vol. 52, no. 7, pp. 1–4, 2016.

[93] A. Savitzky and M. J. Golay, "Smoothing and differentiation of data by simplified least squares procedures.," *Analytical Chemistry*, vol. 36, no. 8, pp. 1627–1639, 1964.

[94] Y. Jiao and R. H. Victora, "Dependence of predicted areal density on common optimization strategies for heat-assisted magnetic recording," *IEEE Magnetics Letters*, vol. 8, pp. 1–4, 2017.

[95] W.-H. Hsu and R. H. Victora, "Rotated read head design for high-density heat-assisted shingled magnetic recording," *Applied Physics Letters*, vol. 118, no. 7, p. 072406, 2021.

[96] S. Kalarickal, A. Tsoukatos, S. Hernandez, C. Hardie, and E. Gage, "Adjacent track interference in heat-assisted magnetic recording: Impact and implications," *IEEE Transactions on Magnetics*, vol. 55, no. 7, pp. 1–4, 2019.

[97] N. A. Natekar and R. Victora, "Analysis of adjacent track erasure in the HAMR media," *IEEE Transactions on Magnetics*, 2020.

[98] Y. Qin, H. Li, and J.-G. Zhu, "Curvature-eliminating head field and track edge characteristics in heat-assisted magnetic recording," *IEEE Transactions on Magnetics*, vol. 53, no. 11, pp. 1–4, 2017.

[99] Y. Jiao, Y. Wang, and R. Victora, "A study of SNR and BER in heat-assisted magnetic recording," *IEEE Transactions on Magnetics*, vol. 51, no. 11, pp. 1–4, 2015.

[100] S. Granz, W. Zhu, E. C. S. Seng, U. H. Kan, C. Rea, G. Ju, J.-U. Thiele, T. Rausch, and E. C. Gage, "Heat-assisted interlaced magnetic recording," *IEEE Transactions on Magnetics*, vol. 54, no. 2, pp. 1–4, 2017.

[101] Y. Wang, M. Erden, and R. H. Victora, "Novel system design for readback at 10 terabits per square inch user areal density," *IEEE Magnetics Letters*, vol. 3, 2012.

[102] N. Natekar, W. Tipcharoen, and R. H. Victora, "Composite media with reduced write temperature for heat assisted magnetic recording," *Journal of Magnetism and Magnetic Materials*, vol. 486, p. 165253, 2019.

[103] N. Smith and P. Arnett, "White-noise magnetization fluctuations in magnetoresistive heads," *Applied Physics Letters*, vol. 78, no. 10, pp. 1448–1450, 2001.

[104] R. W. Wood, J. Miles, and T. Olson, "Recording technologies for terabit per square inch systems," *IEEE Transactions on Magnetics*, vol. 38, no. 4, pp. 1711–1718, 2002.

[105] C. Rea, P. Krivosik, V. Venugopal, M. F. Erden, S. Stokes, P. Subedi, M. Cordle, M. Benakli, H. Zhou, D. Karns, *et al.*, "Heat-assisted recording: Advances in recording integration," *IEEE Transactions on Magnetics*, vol. 53, no. 11, pp. 1–6, 2017.

[106] W.-H. Hsu and R. Victora, "Spin–orbit torque switching in low-damping magnetic insulators: A micrmomagnetic study," *IEEE Magnetics Letters*, vol. 11, pp. 1–5, 2020.

[107] H. Chang, P. Li, W. Zhang, T. Liu, A. Hoffmann, L. Deng, and M. Wu, "Nanometer-thick yttrium iron garnet films with extremely low damping," *IEEE Magnetics Letters*, vol. 5, pp. 1–4, 2014.

[108] A. Quindeau, C. O. Avci, W. Liu, C. Sun, M. Mann, A. S. Tang, M. C. Onbasli, D. Bono, P. M. Voyles, Y. Xu, *et al.*, "$Tm_3Fe_5O_{12}$/Pt heterostructures with perpendicular magnetic anisotropy for spintronic applications," *Advanced Electronic Materials*, vol. 3, no. 1, p. 1600376, 2017.

[109] E. R. Rosenberg, L. Beran, C. O. Avci, C. Zeledon, B. Song, C. Gonzalez-Fuentes, J. Mendil, P. Gambardella, M. Veis, C. Garcia, *et al.*, "Magnetism and spin transport in rare-earth-rich epitaxial terbium and europium iron garnet films," *Physical Review Materials*, vol. 2, no. 9, p. 094405, 2018.

[110] C. O. Avci, A. Quindeau, C.-F. Pai, M. Mann, L. Caretta, A. S. Tang, M. C. Onbasli, C. A. Ross, and G. S. Beach, "Current-induced switching in a magnetic insulator," *Nature Materials*, vol. 16, no. 3, pp. 309–314, 2017.

[111] M. Collet, X. De Milly, O. d. Kelly, V. V. Naletov, R. Bernard, P. Bortolotti, J. B. Youssef, V. Demidov, S. Demokritov, J. Prieto, *et al.*, "Generation of coherent spin-wave modes in yttrium iron garnet microdiscs by spin–orbit torque," *Nature Communications*, vol. 7, no. 1, pp. 1–8, 2016.

[112] P. Li, T. Liu, H. Chang, A. Kalitsov, W. Zhang, G. Csaba, W. Li, D. Richardson, A. DeMann, G. Rimal, *et al.*, "Spin–orbit torque-assisted switching in magnetic insulator thin films with perpendicular magnetic anisotropy," *Nature Communications*, vol. 7, no. 1, pp. 1–8, 2016.

[113] C. Guo, C. Wan, M. Zhao, H. Wu, C. Fang, Z. Yan, J. Feng, H. Liu, and X. Han, "Spin-orbit torque switching in perpendicular $Y_3Fe_5O_{12}$/Pt bilayer," *Applied Physics Letters*, vol. 114, no. 19, p. 192409, 2019.

[114] C. O. Avci, E. Rosenberg, M. Baumgartner, L. Beran, A. Quindeau, P. Gambardella, C. A. Ross, and G. S. Beach, "Fast switching and signature of efficient domain wall motion driven by spin-orbit torques in a perpendicular anisotropy magnetic insulator/Pt bilayer," *Applied Physics Letters*, vol. 111, no. 7, p. 072406, 2017.

[115] C. O. Avci, E. Rosenberg, L. Caretta, F. Büttner, M. Mann, C. Marcus, D. Bono, C. A. Ross, and G. S. Beach, "Interface-driven chiral magnetism and current-driven domain walls in insulating magnetic garnets," *Nature Nanotechnology*, vol. 14, no. 6, pp. 561–566, 2019.

[116] S. Vélez, J. Schaab, M. S. Wörnle, M. Müller, E. Gradauskaite, P. Welter, C. Gutgsell, C. Nistor, C. L. Degen, M. Trassin, *et al.*, "High-speed domain wall racetracks in a magnetic insulator," *Nature Communications*, vol. 10, no. 1, pp. 1–8, 2019.

[117] S. Ding, A. Ross, R. Lebrun, S. Becker, K. Lee, I. Boventer, S. Das, Y. Kurokawa, S. Gupta, J. Yang, *et al.*, "Interfacial Dzyaloshinskii-Moriya interaction and chiral magnetic textures in a ferrimagnetic insulator," *Physical Review B*, vol. 100, no. 10, p. 100406, 2019.

[118] Q. Shao, Y. Liu, G. Yu, S. K. Kim, X. Che, C. Tang, Q. L. He, Y. Tserkovnyak, J. Shi, and K. L. Wang, "Topological Hall effect at above room temperature in heterostructures composed of a magnetic insulator and a heavy metal," *Nature Electronics*, vol. 2, no. 5, pp. 182–186, 2019.

[119] J. Brandão, S. Azzawi, A. Hindmarch, and D. Atkinson, "Understanding the role of damping and Dzyaloshinskii-Moriya interaction on dynamic domain wall behaviour in platinum-ferromagnet nanowires," *Scientific Reports*, vol. 7, no. 1, pp. 1–10, 2017.

[120] C. Wu, C. Tseng, Y. Fanchiang, C. Cheng, K. Lin, S. Yeh, S. Yang, C. Wu, T. Liu, M. Wu, *et al.*, "High-quality thulium iron garnet films with tunable perpendicular magnetic anisotropy by off-axis sputtering–correlation between magnetic properties and film strain," *Scientific Reports*, vol. 8, no. 1, pp. 1–8, 2018.

[121] S. Crossley, A. Quindeau, A. Swartz, E. Rosenberg, L. Beran, C. Avci, Y. Hikita, C. Ross, and H. Hwang, "Ferromagnetic resonance of perpendicularly magnetized $Tm_3Fe_5O_{12}$/Pt heterostructures," *Applied Physics Letters*, vol. 115, no. 17, p. 172402, 2019.

[122] S. Xia, S. Zhang, Z. Luan, L. Zhou, J. Liang, G. Liu, B. Yang, H. Yang, R. Liu, and D. Wu, "Interfacial Dzyaloshinskii-Moriya interaction between ferromagnetic insulator and heavy metal," *Applied Physics Letters*, vol. 116, no. 5, p. 052404, 2020.

[123] E. Grimaldi, V. Krizakova, G. Sala, F. Yasin, S. Couet, G. S. Kar, K. Garello, and P. Gambardella, "Single-shot dynamics of spin–orbit torque and spin transfer torque switching in three-terminal magnetic tunnel junctions," *Nature Nanotechnology*, vol. 15, no. 2, pp. 111–117, 2020.

[124] G. Finocchio, M. Carpentieri, E. Martinez, and B. Azzerboni, "Switching of a single ferromagnetic layer driven by spin Hall effect," *Applied Physics Letters*, vol. 102, no. 21, p. 212410, 2013.

[125] T. Taniguchi, "Theoretical condition for switching the magnetization in a perpendicularly magnetized ferromagnet via the spin Hall effect," *Physical Review B*, vol. 100, no. 17, p. 174419, 2019.

[126] J. Park, G. Rowlands, O. Lee, D. Ralph, and R. Buhrman, "Macrospin modeling of sub-ns pulse switching of perpendicularly magnetized free layer via spin-orbit torques for cryogenic memory applications," *Applied Physics Letters*, vol. 105, no. 10, p. 102404, 2014.

[127] M. Baumgartner, K. Garello, J. Mendil, C. O. Avci, E. Grimaldi, C. Murer, J. Feng, M. Gabureac, C. Stamm, Y. Acremann, *et al.*, "Spatially and time-resolved magnetization dynamics driven by spin–orbit torques," *Nature Nanotechnology*, vol. 12, no. 10, p. 980, 2017.

[128] N. Perez, L. Torres, and E. Martinez-Vecino, "Micromagnetic modeling of Dzyaloshinskii–Moriya interaction in spin Hall effect switching," *IEEE Transactions on Magnetics*, vol. 50, no. 11, pp. 1–4, 2014.

[129] J. Li, G. Yu, C. Tang, Y. Liu, Z. Shi, Y. Liu, A. Navabi, M. Aldosary, Q. Shao, K. L. Wang, *et al.*, "Deficiency of the bulk spin Hall effect model for spin-orbit torques in magnetic-insulator/heavy-metal heterostructures," *Physical Review B*, vol. 95, no. 24, p. 241305, 2017.

[130] W. Legrand, R. Ramaswamy, R. Mishra, and H. Yang, "Coherent subnanosecond switching of perpendicular magnetization by the fieldlike spin-orbit torque without an external magnetic field," *Physical Review Applied*, vol. 3, no. 6, p. 064012, 2015.

[131] J. Yoon, S.-W. Lee, J. H. Kwon, J. M. Lee, J. Son, X. Qiu, K.-J. Lee, and H. Yang, "Anomalous spin-orbit torque switching due to field-like torque–assisted domain wall reflection," *Science Advances*, vol. 3, no. 4, p. e1603099, 2017.

[132] W.-H. Hsu, R. Bell, and R. H. Victora, "Ultra-low write energy composite free layer spin–orbit torque MRAM," *IEEE Transactions on Magnetics*, vol. 54, no. 11, pp. 1–5, 2018.

[133] M. Onbasli, A. Kehlberger, D. H. Kim, G. Jakob, M. Kläui, A. V. Chumak, B. Hillebrands, and C. A. Ross, "Pulsed laser deposition of epitaxial yttrium iron garnet films with low Gilbert damping and bulk-like magnetization," *APL Materials*, vol. 2, no. 10, p. 106102, 2014.

[134] C. Hauser, T. Richter, N. Homonnay, C. Eisenschmidt, M. Qaid, H. Deniz, D. Hesse, M. Sawicki, S. G. Ebbinghaus, and G. Schmidt, "Yttrium iron garnet thin films with very low damping obtained by recrystallization of amorphous material," *Scientific Reports*, vol. 6, p. 20827, 2016.

[135] D. Weller, A. Moser, L. Folks, M. E. Best, W. Lee, M. F. Toney, M. Schwickert, J.-U. Thiele, and M. F. Doerner, "High $K_u$ materials approach to 100 Gbits/in$^2$," *IEEE Transactions on Magnetics*, vol. 36, no. 1, pp. 10–15, 2000.

[136] M. Yoshikawa, E. Kitagawa, T. Nagase, T. Daibou, M. Nagamine, K. Nishiyama, T. Kishi, and H. Yoda, "Tunnel magnetoresistance over 100% in MgO-based magnetic tunnel junction films with perpendicular magnetic $L1_0$-FePt electrodes," *IEEE Transactions on Magnetics*, vol. 44, no. 11, pp. 2573–2576, 2008.

[137] S. Mitani, K. Tsukamoto, T. Seki, T. Shima, and K. Takanashi, "Fabrication and characterization of $L1_0$-ordered FePt/AlO/FeCo magnetic tunnel junctions," *IEEE Transactions on Magnetics*, vol. 41, no. 10, pp. 2606–2608, 2005.

[138] L. Liu, T. Moriyama, D. Ralph, and R. Buhrman, "Spin-torque ferromagnetic resonance induced by the spin Hall effect," *Physical Review Letters*, vol. 106, no. 3, p. 036601, 2011.

[139] N. Zhu, H. Chang, A. Franson, T. Liu, X. Zhang, E. Johnston-Halperin, M. Wu, and H. X. Tang, "Patterned growth of crystalline $Y_3Fe_5O_{12}$ nanostructures with engineered magnetic shape anisotropy," *Applied Physics Letters*, vol. 110, no. 25, p. 252401, 2017.

[140] J. Osborn, "Demagnetizing factors of the general ellipsoid," *Physical Review*, vol. 67, no. 11-12, p. 351, 1945.

[141] A. Khvalkovskiy, D. Apalkov, S. Watts, R. Chepulskii, R. Beach, A. Ong, X. Tang, A. Driskill-Smith, W. Butler, P. Visscher, *et al.*, "Basic principles of STT-MRAM cell operation in memory arrays," *Journal of Physics D: Applied Physics*, vol. 46, no. 7, p. 074001, 2013.

[142] C.-F. Pai, L. Liu, Y. Li, H. Tseng, D. Ralph, and R. Buhrman, "Spin transfer torque devices utilizing the giant spin Hall effect of tungsten," *Applied Physics Letters*, vol. 101, no. 12, p. 122404, 2012.

[143] S. K. Kim and M. Popovici, "Future of dynamic random-access memory as main memory," *MRS Bulletin*, vol. 43, no. 5, p. 334, 2018.

[144] J. Liu, B. Jaiyen, R. Veras, and O. Mutlu, "RAIDR: Retention-aware intelligent DRAM refresh," *ACM SIGARCH Computer Architecture News*, vol. 40, no. 3, pp. 1–12, 2012.

[145] M. Gabor, T. Petrisor Jr, R. Mos, A. Mesaros, M. Nasui, M. Belmeguenai, F. Zighem, and C. Tiusan, "Spin–orbit torques and magnetization switching in W/$Co_2$FeAl/MgO structures," *Journal of Physics D: Applied Physics*, vol. 49, no. 36, p. 365003, 2016.

[146] W. K. Peria, T. A. Peterson, A. P. McFadden, T. Qu, C. Liu, C. J. Palmstrøm, and P. A. Crowell, "Interplay of large two-magnon ferromagnetic resonance linewidths and low Gilbert damping in Heusler thin films," *Physical Review B*, vol. 101, no. 13, p. 134430, 2020.

[147] A. Y. Dobin and R. Victora, "Intrinsic nonlinear ferromagnetic relaxation in thin metallic films," *Physical Review Letters*, vol. 90, no. 16, p. 167203, 2003.

[148] U. Roy, T. Pramanik, L. F. Register, and S. K. Banerjee, "Write error rate of spin-transfer-torque random access memory including micromagnetic effects using rare event enhancement," *IEEE Transactions on Magnetics*, vol. 52, no. 10, pp. 1–6, 2016.